

PREDICTION OF DISC WING AERODYNAMIC CHARACTERISTICS USING
COMPUTATIONAL FLUID DYNAMICS

by

Daniel Barry Honeycutt

A thesis submitted to the faculty of
The University of North Carolina at Charlotte
in partial fulfillment of the requirements
for the degree of Master of Science in
Mechanical Engineering

Charlotte

2020

Approved by:

Dr. Mesbah Uddin

Dr. Russell Keanini

Dr. Jun Xu

©2020
Daniel Barry Honeycutt
ALL RIGHTS RESERVED

ABSTRACT

DANIEL BARRY HONEYCUTT. Prediction of Disc Wing Aerodynamic Characteristics using Computational Fluid Dynamics. (Under the direction of DR. MESBAH UDDIN)

The primary goal of the work presented in this thesis is to assess the effectiveness of Computational Fluid Dynamics (CFD) tools in predicting flow fields around golf discs. The quantities of interest involve aerodynamic force and moment coefficients, surface pressure distributions, and velocity and pressure distributions in the near field region. The veracity of the CFD predictions are investigated by comparing the CFD results against wind tunnel experiments. To date, direct comparisons between CFD and wind tunnel data for commercially available golf discs have not been published, and this will be the first work to do so. In doing so, this thesis also outlines the best practices for the CFD analysis of golf discs. The methods detailed in this thesis can be used to evaluate future disc designs. Three new disc design concepts are conceived and evaluated with the method. Steady-state Reynolds Average Navier-Stokes (RANS) simulations on highly resolved grids are performed using the $k-\omega$ Shear Stress Transport (SST) and Lag elliptic blending $k-\epsilon$ turbulence models. The latter one is a newer model and existing literature shows a very limited number of studies carried out using this turbulence model. The simulations presented in this work were carried out using a commercial finite volume CFD code, STAR-CCM+. It was observed that, compared to the SST model, the Lag elliptic blending $k-\epsilon$ turbulence model produces better correlation with experimental data. However, further improvement of experimental correlation requires that the turbulence model closure coefficients used in the Lag elliptic blending $k-\epsilon$ model be tuned to better correlate the

RANS simulations to the large database of experimental data for a particular disc. Additionally, in order to understand the limitations of the steady-state solution of an inherently unsteady phenomenon, transient Detached Eddy Simulations (DES) are also performed and the results are compared to the steady-state RANS and experimental data.

ACKNOWLEDGEMENTS

First, I would like to thank Dr. Mesbah Uddin. As he well knows, getting a graduate degree while working full time can be very tough. He has helped me through it with great career, academic, and family advise. I would also like to thank Dr. Russell Keanini. I very much appreciated his words of encouragement to the entire class during a Compressible Fluid Dynamics class lecture. I do not recall the exact quote, but I still remember how it made me feel - "if you are struggling to understand a difficult engineering or scientific concept, you are not alone." Thank you for serving on my committee Dr. Keanini. I would also like to thank Dr. Jun Xu for serving on my committee. Thank you, Mr. Kevin Rau of Digital Reality Scanning Services. Mr. Rau scanned the golf discs creating the starting geometry needed for CFD. Mr. Rau and I have scanned many NASCAR racecars together but scanning golf discs was a first for us. And finally, I would like to thank Ms. Tracy Beauregard, UNCC Department of Mechanical Engineering Academic Advisor. I cannot count the number of times that I emailed Ms. Beauregard and she solved my problem immediately or in very short order. I can only hope that I am as helpful to others as you have been to me.

DEDICATION

To my spouse Jeniffer: Thanks for letting me pursue my goals as always. We give each other more space than most, but it has worked for us for over twenty years so why change now. To my kids Aubrey and Gabe: One of my goals in pursuing a graduate degree midcareer was to show you the importance I place on education instead of just telling you. I hope I have done that without sacrificing too much family time during this endeavor. I also hope you have seen that I have had some fun along the way. I have always found that if I try and turn work and learning into fun, life goes much smoother and is so much more interesting. In fact, my quest to get a fun job in motorsports was my main motivation to obtain a bachelor's in engineering following high school. Now the fun sport of disc golf has helped me learn more about fluids dynamics and get closer to a master's degree. It seems that the "fun strategy" has worked again. I cannot wait to see what fun adventure is next!

TABLE OF CONTENTS

NOMENCLATURE	ix
LIST OF TABLES	xiii
LIST OF FIGURES	xiv
CHAPTER 1. INTRODUCTION	1
1.1 Motivation	1
1.2 Organization of thesis	2
1.3 Brief introduction to the sport of disc golf	3
CHAPTER 2. LITERATURE REVIEW	6
CHAPTER 3. TURBULENCE MODELING	12
3.1 Direct numerical simulation	14
3.2 Large eddy simulation	15
3.3 Reynolds Averaged Navier-Stokes	16
3.1 k - ω SST turbulence model	17
3.2 Lag elliptical blending k - ε turbulence model	19
3.3 k - ε empirical coefficients	21
3.4 Detached eddy simulation	23
CHAPTER 4. NUMERICAL SETUP	25
4.1 Disc shapes – existing discs	26
4.2 Disc shapes – new design concepts	28
4.3 Computational domain and boundary conditions	32
4.4 Prism layers	33

4.5 Core mesh.....	33
4.6 DES mesh refinement – Floater calibration disc.....	37
4.7 Golf discs’ mesh.....	38
4.8 Physics setup – RANS and DES	39
4.9 Additional angles of attack.....	41
CHAPTER 5. RANS RESULTS	42
5.1 Mesh refinement study	42
5.2 Floater calibration disc	43
5.3 Commercial golf discs.....	66
5.4 New disc designs.....	74
5.5 Additional angles of attack runs.....	76
5.6 Note on preliminary simulations.....	82
CHAPTER 6. DES RESULTS	83
6.1 Mesh refinement study	83
6.2 Time step convergence study	87
CHAPTER 7. CONCLUSIONS	92
REFERENCES	95

NOMENCLATURE

A	disc plan view area ($\pi d^2/4$)
AdvR	advance ratio [$\omega_{\text{rot}}(d/2)/V_{\infty}$]
AIAA	American Institute of Aeronautics and Astronautics
AoA	angle of attack ($^{\circ}$)
c	chord length (diameter for a disc)
CAD	computer-aided design
C_D	drag coefficient (drag force / QA)
c_f	skin friction
CFD	computational fluid dynamics
C_L	lift coefficient (lift force / QA)
CP	pressure coefficient (static pressure/Q)
C_{PM}	pitch moment coefficient (pitch moment / QAd)
d	disc diameter
DDES	delayed detached eddy simulation
DES	detached eddy simulation
E	E term in Lag elliptical blending k - ε model
EB	elliptic blending
Exp	experimental
F_1	blending function 1
F_2	blending function 2
FTT	flow through time (d/ V_{∞})

f_η, f_ω	parameters found by solving elliptic relaxation functions
k	turbulent kinetic energy
L	length scale
LES	large eddy simulation
LETOT	large eddy turn-over time
M_{ij}	term expressed as function of anisotropy tensor
p	pressure
P	production of turbulent kinetic energy
PDGA	Professional Disc Golf Association
PIV	particle image velocimetry
P_k	production of turbulent kinetic energy
Q	dynamic pressure $[(\rho V_\infty^2)/2]$
RANS	Reynolds Averaged Navier-Stokes
Re	Reynolds number
S	Strain rate tensor
SGS	sub grid scale
S_{ij}	Favre-averaged strain rate tensor
t	time
T, T_s	time scale
t/d	disc thickness to diameter ratio
u	velocity
U_i	average velocity
$\overline{u'_i u'_j}$	Reynolds stress tensor

V_∞	free stream velocity
x/c	specified spatial dimension divided by chord length or span
y	wall normal coordinate
y^+	nondimensional wall distance based on cell fluid velocity
α	non-dimensional coefficient that represents the lag effect on eddy viscosity found from solving the elliptic differential equation
δ	boundary layer thickness
δ_{ij}	Kronecker delta
ε	turbulent energy dissipation rate
η	Kolmogorov length scale
η	ratio between mean velocity strain and turbulence time-scales, Lag elliptical blending k - ε model
μ	dynamic viscosity
μ_τ	turbulent viscosity
ν	kinematic viscosity
ν_t	turbulent viscosity
ρ	fluid density
τ_{ij}	viscous stresses
φ	reduced stress function
ω	specific turbulent dissipation ($\omega \propto \varepsilon/k$)
ω_{rot}	rotation rate (rad/sec)
$a_1, \beta, \beta^*, \sigma_k, \sigma_\omega, \sigma_{\omega 2}, \gamma$	k - ω SST closure coefficients

$C_\mu, C_{\varepsilon 1}, C_{\varepsilon 2}, \sigma_\varepsilon, \sigma_k$

k - ε closure coefficients

$C_k, C_{P1}, C_{P2}, C_{P3}, C_t, C_{\varepsilon 1}, C_{\varepsilon 2}, C_\mu,$
 $C_\eta, C_\omega^*, \widetilde{C}_1, C_1^*, CL, \sigma_\varepsilon, \sigma_k, \sigma_\varphi$

Lag elliptical blending k - ε closure coefficients

LIST OF TABLES

TABLE 2.1. Golf disc aerodynamic publications.....	8
TABLE 4.1. Disc dimensions – existing discs	27
TABLE 4.2. Mesh details – Floater calibration disc	37
TABLE 5.1. RANS mesh refinement study results	43
TABLE 6.1. Aerodynamic force and moment coefficients from DES mesh refinement study for constant time step of $\Delta t=0.079$, $\text{AoA}=10^\circ$	85
TABLE 6.2. DES time step convergence, M27 medium mesh. $\text{AoA}=10^\circ$	88
TABLE 6.3. DES time step convergence, M27 medium mesh. $\text{AoA}=20^\circ$	91

LIST OF FIGURES

FIGURE 1.1. Disc golf target [6].....	5
FIGURE 1.2. Bradford Disc Golf Park, Huntersville, NC. Hole #9 view back to tee pad [7].....	5
FIGURE 2.1. Force and moment coefficient data for various advance ratios (AdvR or spin rates) at $Re=378,000$ [2]	10
FIGURE 2.2. Three-dimensional flow topology for the Floater disc by Potts. $AoA=10^\circ$ [2].....	11
FIGURE 3.1. Illustrative comparison of DNS, LES, and RANS [15].....	13
FIGURE 4.1. Disc Dimensions and Shape – existing discs	27
FIGURE 4.2. Disc 1	29
FIGURE 4.3. Disc 2.....	30
FIGURE 4.4. Disc 3.....	31
FIGURE 4.5. Computational domain	32
FIGURE 4.6. Mesh refinement zones at center span. Air flow direction is from left to right.....	34
FIGURE 4.7. Mesh top section view at mid-disc thickness	35
FIGURE 4.8. Medium (M27) mesh top and medium targeted (M31) mesh bottom. Center span.....	36
FIGURE 4.9. Turbulent dissipation rate for the Floater calibration disc at center span. Lag EB $k-\varepsilon$, $AoA=10^\circ$	38
FIGURE 4.10. Wraith golf disc with medium mesh. Center span.....	39
FIGURE 5.1. Aerodynamic force and moment coefficients for the Floater (calibration) disc for experimental, $k-\omega$ SST, Lag EB $k-\varepsilon$, Lag EB $k-\varepsilon$ tuned. C_D top, C_L center and C_{PM} bottom	49
FIGURE 5.2. Experimental pitch moment coefficient data and pressure calculated pitch moment coefficients for the Floater (calibration) disc [2].....	50
FIGURE 5.3. Recalculated CFD pitch moment using alternate pitch moment axis.....	50

FIGURE 5.4. Centerline span pressure profiles for the Floater (calibration) disc. Experiment [2] and CFD. $k-\omega$ SST top, Lag EB $k-\varepsilon$ center, Lag EB $k-\varepsilon$ tuned bottom, $AoA=0^\circ$	51
FIGURE 5.5. $1/4^{\text{th}}$ Span pressure profiles for the Floater (calibration) disc. Experiment [2] and CFD. $k-\omega$ SST top, Lag EB $k-\varepsilon$ center, Lag EB $k-\varepsilon$ tuned bottom, $AoA=0^\circ$	52
FIGURE 5.6. $1/8^{\text{th}}$ Span pressure profiles for the Floater (calibration) disc. Experiment [2] and CFD. $k-\omega$ SST top, Lag EB $k-\varepsilon$ center, Lag EB $k-\varepsilon$ tuned bottom, $AoA=0^\circ$	53
FIGURE 5.7. $1/2$ Chord pressure profiles for the Floater (calibration) disc. Experiment [2] and CFD. $k-\omega$ SST top, Lag EB $k-\varepsilon$ center, Lag EB $k-\varepsilon$ tuned bottom, $AoA=0^\circ$	54
FIGURE 5.8. Centerline span pressure profiles for the Floater (calibration) disc. Experiment [2] and CFD. $k-\omega$ SST top, Lag EB $k-\varepsilon$ center, Lag EB $k-\varepsilon$ tuned bottom, $AoA=10^\circ$	55
FIGURE 5.9. $1/4^{\text{th}}$ Span pressure profiles for the Floater (calibration) disc. Experiment [2] and CFD. $k-\omega$ SST top, Lag EB $k-\varepsilon$ center, Lag EB $k-\varepsilon$ tuned bottom, $AoA=10^\circ$	56
FIGURE 5.10. $1/8^{\text{th}}$ Span pressure profiles for the Floater (calibration) disc. Experiment [2] and CFD. $k-\omega$ SST top, Lag EB $k-\varepsilon$ center, Lag EB $k-\varepsilon$ tuned bottom, $AoA=10^\circ$	57
FIGURE 5.11. $1/2$ Chord pressure profiles for the Floater (calibration) disc. Experiment [2] and CFD. $k-\omega$ SST top, Lag EB $k-\varepsilon$ center, Lag EB $k-\varepsilon$ tuned bottom, $AoA=10^\circ$	58
FIGURE 5.12. Centerline span pressure profiles for the Floater (calibration) disc. Experiment [2] and CFD. $k-\omega$ SST top, Lag EB $k-\varepsilon$ center, Lag EB $k-\varepsilon$ tuned bottom, $AoA=20^\circ$	59
FIGURE 5.13. $1/4^{\text{th}}$ Span pressure profiles for the Floater (calibration) disc. Experiment [2] and CFD. $k-\omega$ SST top, Lag EB $k-\varepsilon$ center, Lag EB $k-\varepsilon$ tuned bottom, $AoA=20^\circ$	60
FIGURE 5.14. $1/8^{\text{th}}$ Span pressure profiles for the Floater (calibration) disc. Experiment [2] and CFD. $k-\omega$ SST top, Lag EB $k-\varepsilon$ center, Lag EB $k-\varepsilon$ tuned bottom, $AoA=20^\circ$	61
FIGURE 5.15 $1/2$ Chord pressure profiles for the Floater (calibration) disc. Experiment [2] and CFD. $k-\omega$ SST top, Lag EB $k-\varepsilon$ center, Lag EB $k-\varepsilon$ tuned bottom, $AoA=20^\circ$	62
FIGURE 5.16. CFD centerline span velocity magnitude plots for the Floater (calibration) disc. $k-\omega$ SST top, Lag EB $k-\varepsilon$ center, Lag EB $k-\varepsilon$ tuned bottom, $AoA=10^\circ$	63
FIGURE 5.17. CFD centerline span turbulent kinetic energy plots for the Floater (calibration) disc. $k-\omega$ SST top, Lag EB $k-\varepsilon$ center, Lag EB $k-\varepsilon$ tuned bottom, $AoA=10^\circ$	64

FIGURE 5.18. Comparison of trailing vortices. $k-\omega$ SST top, experiment center, Lag EB $k-\varepsilon$ tuned bottom, one diameter aft of disc trailing edge. AoA=10°. Reynolds number for experiment was 56,700 [2].....	65
FIGURE 5.19. Aerodynamic force and moment coefficients for the Quarter K golf disc, Lag EB $k-\varepsilon$ tuned turbulence model and experiment [12]. C_D top, C_L center and C_{PM} bottom	68
FIGURE 5.20. Aerodynamic force and moment coefficients for the Flick golf disc, Lag EB $k-\varepsilon$ tuned turbulence model and experiment [12]. C_D top, C_L center and C_{PM} bottom	69
FIGURE 5.21. Aerodynamic force and moment coefficients for the Wraith golf disc, Lag EB $k-\varepsilon$ tuned turbulence model and experiment [12]. C_D top, C_L center and C_{PM} bottom	70
FIGURE 5.22. C_D v. AoA for all existing discs: experiment top [12], CFD bottom.....	71
FIGURE 5.23. C_L v. AoA for all existing discs: experiment top [12], CFD bottom	72
FIGURE 5.24. C_{PM} v. AoA for all existing discs: experiment top [12], CFD bottom.....	73
FIGURE 5.25. Aerodynamic force and moment coefficients (CFD) for three new disc designs and the Wraith disc	75
FIGURE 5.26. Velocity magnitude. Wraith top, Disc 2 bottom. AoA=10°.	76
FIGURE 5.27. Aerodynamic force and moment coefficient results with additional angles of attack for Floater calibration disc	78
FIGURE 5.28. Aerodynamic force and moment coefficient results with additional angles of attack for Quarter K disc	79
FIGURE 5.29. Aerodynamic force and moment coefficient results with additional angles of attack for Flick disc	80
FIGURE 5.30. Aerodynamic force and moment coefficient results with additional angles of attack for Wraith disc	81
FIGURE 6.1. Residuals for M27, LETOTS=197, FTT=0.079	85
FIGURE 6.2. C_D (top), C_L (center) and C_{PM} (bottom) for M27, LETOTS=197, FTT=0.079	86
FIGURE 6.3. Centerline span pressure profiles for the Floater (calibration) disc. Experiment [2] and CFD Lag EB $k-\varepsilon$ tuned (RANS) model, AoA=20°	89

FIGURE 6.4. Centerline span pressure profiles for the Floater (calibration) disc. Experiment [2], Lag EB k - ϵ tuned model, and DES, AoA=20°, DES FFT=0.00889

FIGURE 6.5. Centerline span pressure profiles for the Floater (calibration) disc. Experiment [2], Lag EB k - ϵ tuned model, and DES, AoA=20°, DES FFT=0.00490

FIGURE 6.6. Centerline span pressure profiles for the Floater (calibration) disc. Experiment [2], Lag EB k - ϵ tuned model, and DES, AoA=20°, DES FFT=0.00290

FIGURE 6.7. Centerline span pressure profiles for the Floater (calibration) disc. Experiment [2], Lag EB k - ϵ tuned model, and DES, AoA=20°, DES FFT=0.00191

CHAPTER 1. INTRODUCTION

Aerodynamics plays a major role in projectile sports. The flight path of a soccer ball, football, baseball, discus, golf ball or any other projectile are largely determined by their aerodynamic force and moment coefficients which are mostly defined by their shape. Unlike other projectile sports, in disc golf, the projectile shape is not standardized. Although there are basic dimensional and mass rules specified by the Professional Disc Golf Association (PDGA), there is still a large amount of design freedom. New discs are introduced by manufacturers regularly with the aim of improving distance and accuracy or to suit a particular throwing style or course layout by achieving a particular flight path. Most players use at least three discs (a driver disc, a mid-range disc, and putter disc) for one round of play. Experienced players use as many as ten to fifteen unique discs during a round of play. The PDGA lists over 1200 approved discs on their website [1].

1.1 Motivation

Even though aerodynamics and therefore disc shape are very important in the sport of disc golf, very few aerodynamic studies have been completed on golf discs. Wind tunnel testing is expensive, so a limited number of tests have been performed. Although some experimental data exists for golf discs, to date, no data are publicly available comparing commercial golf disc experimental aerodynamic data to computational fluid dynamics (CFD) data. A unique opportunity exists for the application of CFD to this sport since disc golf is a relatively young compared to other projectile sports that matured prior to the advent of widely available CFD software. CFD could be a very valuable tool for the design and evaluation of golf discs, but there have been relatively few CFD analyses completed of competition discs. As such, the goals of this paper are as follows:

1. Perform steady-state RANS CFD simulations on a disc shape using a commercial code and compare the results to available experimental data.
2. Tune the RANS CFD processes and models as needed to more closely match experimental data.
3. Evaluate commercially available golf discs for which wind tunnel data exists.
4. Design new discs and evaluate the designs using the tuned RANS model.
5. Perform detached eddy simulations (DES) for comparison to the RANS and experimental data.

1.2 Organization of thesis

Chapter 1 lays out the motivations of this study and gives a brief introduction to the sport of disc golf. Chapter 2 is a literature review of golf disc aerodynamic publications and other applicable literature such as CFD of low aspect ratio wings. This chapter includes a very useful image taken from the research of Potts showing the major flow structures around a flying disc [2]. Chapter 3 is a brief summary of turbulence modeling in general and a summary of the turbulence models used in this study. Chapter 4 details the numerical setup. This chapter includes the geometric details of the discs and mesh. Some newly designed discs are introduced in this chapter. The physics setup is also contained here. Mesh refinements are also described. Chapter 5 contains the RANS results and discussion. RANS mesh refinement study results are contained here. Chapter 6 contains DES results and discussion. DES mesh and time step convergence study results are included here. Chapter 7 concludes the work and contains suggestions for future research.

1.3 Brief introduction to the sport of disc golf

The Professional Disc Golf Association (PDGA) is the most prominent rule making body for disc golf in the world. “The PDGA is a membership-based organization in 47 countries, with over 100,000 members. The PDGA is the governing body for the sport and sanctions competitive events for men and women of every skill level from novice to professional. By some estimates there are as many as 5 million disc golf players and 7,000 courses in the United States [3]. “Although most players play on a casual, amateur level, the professional disc golf scene is also growing rapidly, with the top professionals playing full-time and earning their livings through tournament winnings and sponsorship from equipment manufacturers [4]”.

Disc golf is played much like the traditional game of golf except instead of striking a ball towards a hole, a plastic disc is thrown by the player towards an above ground target, FIGURE 1.1. The goal is to pitch the disc into the target using the fewest number of throws of the disc possible, starting from a tee pad (typically a concrete pad or other hard surface) and finishing when the disc is tossed into the target or basket. “Most disc golf courses consist of 18 or 24 holes, but some nine-hole courses can be found too. Holes’ lengths vary, but generally fall between 150 and 500 feet each. As a player progresses down the fairway, he or she must make each consecutive shot from the spot where the previous throw has landed. The trees, shrubs, and terrain changes located in and around the fairways provide challenging obstacles for the disc golfer [5].” It is worth noting that Charlotte, NC is a disc golf hub. In fact, Charlotte hosted the 2012 Disc Golf World Championships and many renowned courses are in the metro region. FIGURE 1.2 in an image from the target looking back to the tee pad at Bradford Disc Golf Park in Huntersville, NC. Notice the

narrow fairway which is typical of many disc golf courses demanding both long as well as accurate throws from players.



FIGURE 1.1. Disc golf target [6]



FIGURE 1.2. Bradford Disc Golf Park, Huntersville, NC. Hole #9 view back to tee pad [7]

CHAPTER 2. LITERATURE REVIEW

Compared to projectiles from other sports such as golf balls and soccer balls, very few aerodynamic studies have been published on golf discs. This is especially surprising given the large amount of design freedom available for golf discs compared to other sports projectiles which are largely standardized. This chapter will review publications specific to golf disc, studies on other disc shapes, and other potentially applicable studies such as those on low aspect ratio wings.

TABLE 2.1 is a list of peer reviewed papers directly related to golf disc aerodynamics published in journals. Future researchers may wish to append to this table and include it in their work as more golf disc research is published or if papers were overlooked. The first peer reviewed technical paper on the study of a golf disc was published through the AIAA in 2000 [8]. Higuchi et al. studied the flow structures of a flying disc using PIV (particle image velocimetry). The authors cited the monotonically increasing lift coefficient at extremely high angles of attack for disc-wings which may have application to micro-air vehicles. The authors note that a spinning disc created a transition which suppressed trailing edge separation. Reynolds numbers and spin rates ($AdvR$) for this study were 100,000 and 0.8 respectively which are comparable to normal golf disc launch speeds. The spin rate or $AdvR$ is the ratio of disc tip speed to free stream velocity, $AdvR = \omega_{rot}(d/2)/V_{\infty}$. Note that wind tunnel data which will be cited later in this paper from other sources shows a negligible change in aerodynamic force and moment coefficients due to spin at typical Reynolds numbers ($\sim 400,000$) and spin rates (~ 1.0) for golf discs. In 2010, Lissaman and Hubbard published a paper describing optimum flight path of a golf disc for maximum distance. This paper published virtually equal release velocities for

amateur and professional players of about 23 m/sec which corresponds to a Reynolds number of about 300,000 for a typical golf disc [9]. In 2014, Lukes et al. were the first to publish CFD analyses of a commercially available golf disc. Prior to performing analyses on the golf disc, three turbulence models were tested on a flat disc with a thickness to diameter ratio (t/d) of 0.1, which is typical of golf discs, to determine their suitability for use on the more complex geometry of the golf disc. Reynolds Average Navier-Stokes (RANS) analyses using commercial software were performed using the $k-\epsilon$, realizable $k-\epsilon$ and $k-\omega$ turbulence models on the flat disc. The standard $k-\epsilon$ and realizable $k-\epsilon$ were judged to yield reasonable results compared to the experimental data for the flat disc. The $k-\omega$ model was judged to be inadequate due to differences in aerodynamic coefficients. Next, the standard $k-\epsilon$ and realizable $k-\epsilon$ were used for CFD analyses on the commercial golf disc. Experimental data were not available for comparison to the golf disc [10]. The final entry in TABLE 2.1 is a 2018 publication from Kamaruddin et al. which contains wind tunnel force and moment data for parametric discs, and three golf discs. Using the wind tunnel force and moment coefficients as inputs, six degree-of-freedom simulations of the discs were performed to visualize their flight trajectories and attitudes [11].

TABLE 2.1. Golf disc aerodynamic publications

Date	Title	Authors	Journal	Disc Shapes	Ref.
2000	Rotating flying disks and formation of trailing vortices	Higuchi, Goto, Hiramoto, Meisel	AIAA	Name not specified, but image appears to be a golf disc driver.	[8]
2010	Maximum range of flying discs	Lissaman, Hubbard	International Sports Engineering Association	Name not specified, but golf discs are stated to have been used.	[9]
2014	A CFD analysis of flow around a disc	Lukes, Hart, Potts, Haake	International Sports Engineering Association	flat disc, Floater	[10]
2018	Aerodynamic performance of flying discs	Kamaruddin, Potts, Crowther	Aircraft Engineering and Aerospace Technology	Parametric, Aviar, Roc, Wraith	[11]

Now other relevant disc studies will be discussed. Kamaruddin’s 2011 PhD thesis published wind tunnel data for six golf discs and many different parametric disc shapes. Using the wind tunnel force and moment coefficients as input, disc flight trajectories were predicted with numerical simulations. Aerodynamic force data are available from -5 degrees to 15 degrees angle of attack and flow visualization data are available for 0 and 5 degrees for three of the disc golf drivers. These three discs are simulated in CFD in the present study [12]. Potts and Masters published results in 2015 comparing RANS CFD using the $k-\omega$ SST turbulence model and experimental data for a flat plate disc, a cavity disc and, a generic field athletic discuss [13]. Good correlation for the flat plate experimental and CFD data were obtained. For the cavity disc, good correlation for the drag coefficient (C_D) and lift coefficient (C_L) were obtained but the pitch moment curve v. angle of attack was flatter for CFD compared to the experiment. Potts presented extensive aerodynamic force data, pressure profile data, and flow visualization in the 2005 PhD thesis work for a disc with a large cavity referred to as a disc-wing or its commercial name of

Floater. Since Potts published such an extensive amount of data on the Floater disc, this shape was used in the current study to calibrate the CFD model. Potts showed that disc spin affects aerodynamic forces negligibly at typical golf disc launch speeds. Potts states that an advance ratio (AdvR or tip speed to free stream ratio) of 1.0 would be the maximum spin expected from a typical human hand launch [2]. FIGURE 2.1, force and moment coefficients at various advance ratios, was taken from Potts [2]. It was noted during the defense of the current work that one explanation for the negligible effect of spin on aerodynamic forces is that the flow through time ($FFT = d / V_{\infty}$) is relatively short compared to the time required for one disc revolution for the subject diameter and Reynolds numbers. In fact, at $V_{\infty} = 20$ m/sec and AdvR=1.04, for 1 FFT, the disc will only spin about 1/3 of a revolution. Potts also published a very useful image depicting three-dimensional flow structures of a flying disc based on flow visualization, FIGURE 2.2. Notice the leading edge separation bubble and counter-rotating trailing vortices.

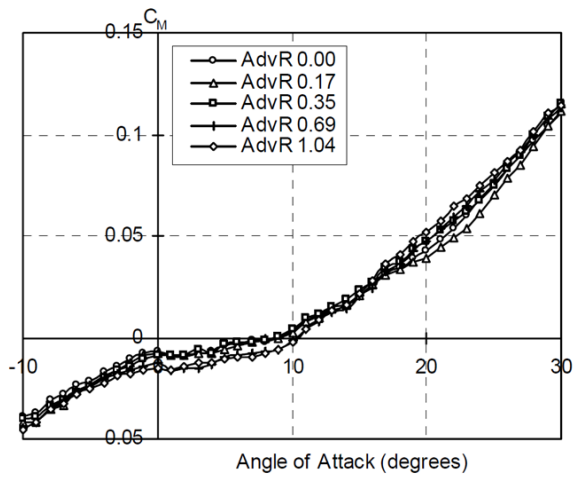
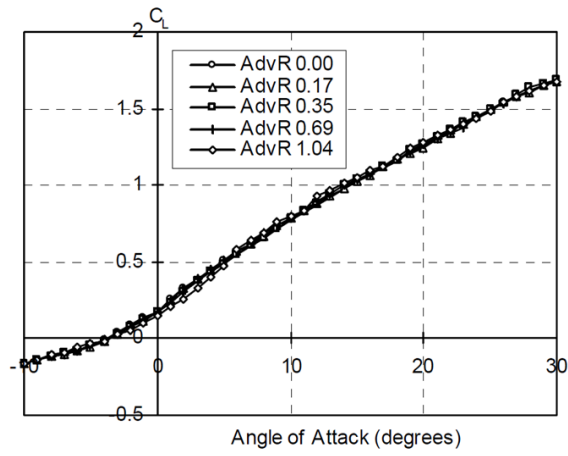
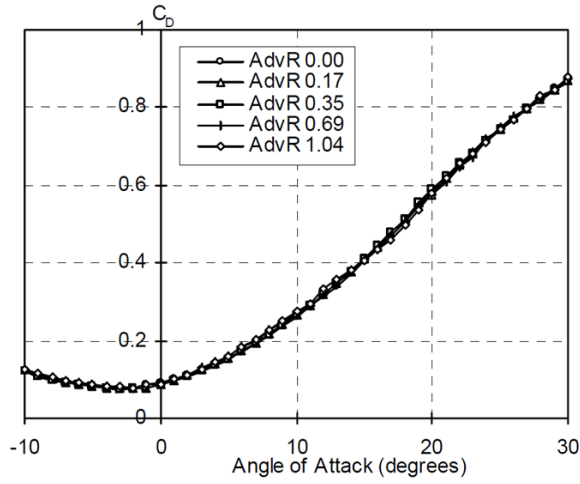


FIGURE 2.1. Force and moment coefficient data for various advance ratios (AdvR or spin rates) at $Re=378,000$ [2]

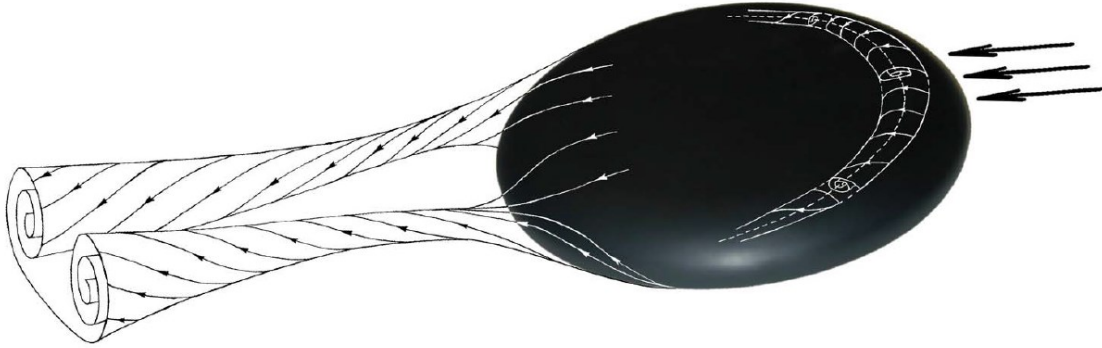


FIGURE 2.2. Three-dimensional flow topology for the Floater disc by Potts. $AoA=10^\circ$
[2]

Low aspect ratio wings have received more attention recently due to the emergence of micro-air vehicles. Discs and other low aspect ratio wings are inefficient and have shallow lift slopes, but they do have the advantage of producing lift at very high angles of attack. Stall angles as high as 29 degrees have been reported for discs by Higuchi et al [8]. The aspect ratio of a disc is 1.0 given that the chord length and span are equal. As such, the literature on CFD of low aspect ratio wings was also examined for this study. Cosyn and Vierendeels performed CFD simulations on low aspect ratio wings at a Reynolds number of 100,000 primarily for application to micro-air vehicles. Before proceeding, Cosyn and Vierendeels evaluated turbulence models in 2D by comparing CFD results to experimental results for the S5010 cambered airfoil. After testing many turbulence models including variants of the $k-\epsilon$ and $k-\omega$ models, the Spalart-Allmaras model was deemed most suitable based on comparison to experimental data for drag and lift coefficients [14].

CHAPTER 3. TURBULENCE MODELING

As originally stated, one goal of this paper is to assess the viability of using CFD as the primary aerodynamic evaluation tool for golf discs. In the foreseeable future, for design engineers to evaluate discs using CFD, Reynolds Averaged Navier-Stokes (RANS) will likely be the modeling approach. As computing power increases, Detached Eddy Simulation (DES) becomes more accessible, but DES models are still rather complex to operate effectively even in commercial packages. This chapter briefly reviews CFD methods starting with direct numerical simulation (DNS). Next large eddy simulation (LES) is discussed. RANS models are then discussed and finally the hybrid approach of detached eddy simulation (DES) which combines RANS and LES is summarized.

FIGURE 3.1, an excerpt from an image by Hanjalić, presents an illustrative comparison of DNS, LES and RANS simulations of a fully developed turbulent steady flow in a pipe [15]. The top of the figure gives a schematic comparison of the grid size required and time averaged velocity profile yielded from each method. Although DNS yields the most accurate results by simulating all scales of turbulence, it requires the most dense grid. Next is LES which reduces the grid density significantly and yields less accuracy. RANS represented on the right side is the least expensive computationally and the least accurate. The RANS solutions are only capable of producing a constant velocity at a point and does not simulate fluctuations in the flow at each point in space and time [15].

COMPARISON OF SIMULATION METHODS
FULLY DEVELOPED FLOW IN A PIPE

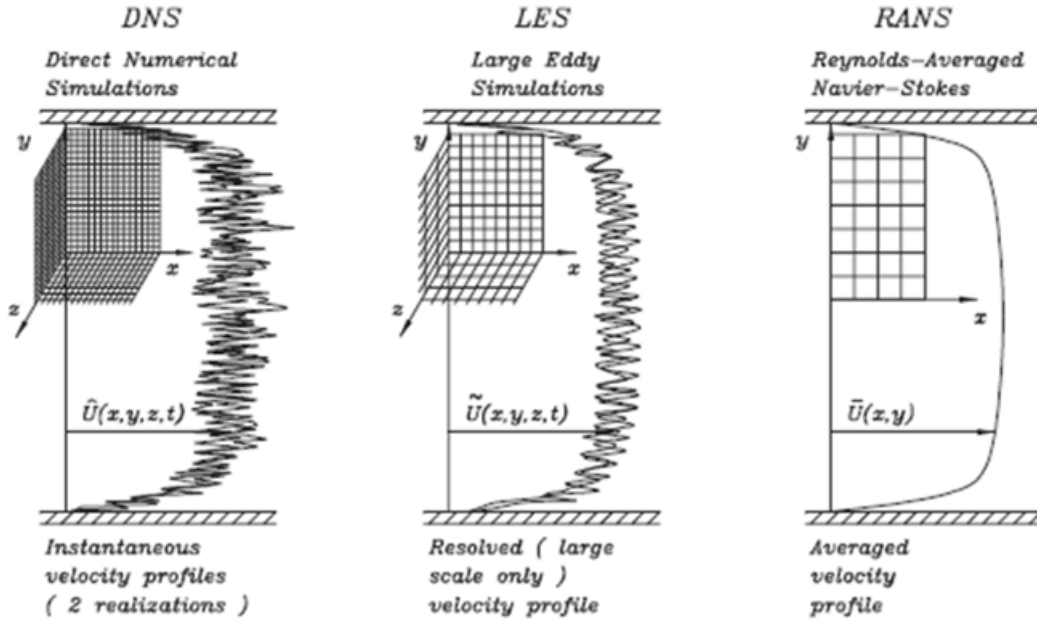


FIGURE 3.1. Illustrative comparison of DNS, LES, and RANS [15]

According to Schlichting and Gersten [16], there is little doubt that the Navier-Stokes equations derived in the mid-1800's completely describe fluid flow. There are only a few known closed formed solutions for a few specific cases, but the results agree very well with experiment [16]. Since discs operate at speeds much less than supersonic, the incompressible version of the Navier-Stokes equations written using Einstein's compact notation are included below. For Einstein's notation repeated indices are summed over their entire range. For instance, in the case of the velocity term u_i , $u_i u_i = u_i u_i + u_j u_j + u_k u_k$. Equation (1) is the conservation of mass and equation (2) is the conservation of momentum.

Equation (3) represents the viscous stresses, τ_{ij} [17]. Fluid density is represented by ρ , pressure is p , and μ is the dynamic viscosity.

$$\frac{\partial u_i}{\partial x_i} = 0 \quad (1)$$

$$\frac{\partial u_i}{\partial t} + u_j \frac{\partial u_i}{\partial x_j} = -\frac{1}{\rho} \frac{\partial p}{\partial x_i} + \frac{\partial \tau_{ij}}{\partial x_j} \quad (2)$$

$$\tau_{ij} = \mu \left(\frac{\partial u_i}{\partial x_j} + \frac{\partial u_j}{\partial x_i} \right) \quad (3)$$

3.1 Direct numerical simulation

Direct numerical simulation (DNS) is like carrying out an experiment in a computer rather than a physical laboratory such as a wind tunnel. In fact, many people refer to DNS as numerical experiments [18]. But this comprehensiveness comes at a cost. Cell dimensions must become very small to resolve down to the smallest dissipative motions which are on the order of the Kolmogorov scale, η . The Kolmogorov length scale can be estimated as $\eta = (\nu^3/\varepsilon)^{1/4}$ [19]. Turbulent dissipation rates as high as 7.5 million (m^2/s^3) were obtained from RANS simulations for discs in the current study. Using this value for ε and a kinematic viscosity of air, ν at $1.6 \times 10^{-5} \text{ m}^2/\text{s}$ yields a Kolmogorov scale of 0.005 mm. For reference, the smallest cells in the core mesh for the finest grid model in the current study were 0.9 mm, almost 200 time larger than those needed to resolve the Kolmogorov scales. Using 0.005 mm cells would result in a mesh with over 1 trillion cells. Even the most powerful supercomputer could not manage a mesh of this size. Disc models in the current were about 4 million cells for most runs. For a DNS run time reference, consider the 2015 DNS performed by Lee and Moser with a Reynolds number of 125,000,

3 times less than the current study on discs. Rodi reports that on the Mira supercomputer with performance measured in petaflops this simulation took several months to complete [20]. Considering model size and run time requirements, it is not likely that DNS will be used for practical aerodynamics problems in the near future. See Pope for a more comprehensive treatment of DNS [17].

3.2 Large eddy simulation

Nearly all the computational cost of DNS is expended on the smallest, dissipative motions [17]. In large eddy simulation (LES), larger eddies are resolved with the unsteady Navier-Stoke equations while the smaller eddies are assumed to be isotropic and to behave similarly to one another and are developed using a sub grid scale (SGS) model thus avoiding much of the computational expense of DNS. LES accuracy is largely dependent on the SGS model used. Many SGS models are based on eddy viscosity modeling with the Smagorinsky model being one of the most common [21]. Leading research such as that of Fröhlich et al. recommend resolving eddies as small as 12 times the Kolmogorov scale [22]. Using this factor of 12 recommendation, LES models are still prohibitively expensive in most cases. Note, the term large eddy turn-over time (LETOT) is often used in LES and is defined as the time period for large eddies to transfer energy to the smaller eddies and can be calculated using equation (4) where t is the time of interest for the simulation, L is the length scale, and V_∞ is the free stream velocity [23]. See Pope for a more comprehensive treatment of LES [17].

$$LETOT = \frac{t}{L/V_\infty} \quad (4)$$

3.3 Reynolds Averaged Navier-Stokes

In contrast to DNS where all turbulence scales are resolved and LES where the larger turbulence scales are resolved and the smaller scales are modeled, all turbulence scales are modeled for the Reynolds Averaged Navier-Stokes method. RANS simulations are less computationally expensive than DNS and LES simulations, but this comes at a cost to accuracy since many of the modeling assumptions are non-physical. All RANS models include empirical numerical constants referred to as closure coefficients. The closure coefficients are typically derived using dimensional analysis, experimental data, and heuristics. For this reason, a particular RANS model with constant coefficients may not be valid for all cases. Nonetheless, RANS models have become very popular and are the workhorses of industrial CFD due to their efficiency and robustness compared to DNS and LES.

There are two main types of RANS models: eddy viscosity and Reynolds stress. Eddy viscosity models use an apparent viscosity increase of the mean flow to simulate turbulent motion. Reynolds stress models directly calculate the Reynolds stress tensor components by solving their governing transport equations. Reynolds stress models (RSM) are computationally expensive compared to eddy viscosity models. RSMs must solve seven equations and typically require more iterations than two equation models to converge [24]. As such, two equation models such as the k - ω and the k - ϵ and their variants are more popular in industry.

The RANS equations are derived by taking the statistical average of the turbulent velocities in the Navier-Stokes equations yielding equation (5) and (6) below where $U_i = \overline{u_i}$.

$$\frac{\partial U_i}{\partial x_i} = 0 \quad (5)$$

$$\frac{\partial U_i}{\partial t} + U_j \frac{\partial U_i}{\partial x_j} = -\frac{1}{\rho} \frac{\partial p}{\partial x_i} + \frac{1}{\rho} \frac{\partial \tau_{ij}}{\partial x_j} - \frac{\partial \overline{u'_i u'_j}}{\partial x_j} \quad (6)$$

The Reynolds stress tensor, $\overline{u'_i u'_j}$, controls the irregular mean flow. As previously mentioned, Reynolds stress models directly calculate the Reynolds stress tensor which means seven equations must be solved. Eddy viscosity models introduce the unphysical eddy viscosity, ν_t , which reduce the number of equations from seven to two. This is known as the Boussinesq approximation which yields equation (7) where k is the turbulent kinetic energy and δ_{ij} is the Kronecker delta [15]. The two eddy viscosity models used in this study are previewed in the following sections.

$$\overline{u'_i u'_j} = \frac{2}{3} k \delta_{ij} - \nu_t \left(\frac{\partial U_i}{\partial t} + U_j \frac{\partial U_i}{\partial x_j} \right) \quad (7)$$

3.1 k - ω SST turbulence model

The k - ω SST turbulence model was used as installed in STAR-CCM+ which was adapted from Menter for all results presented in this paper [25]. As is well known, this model makes use of a k - ω model in the near wall region but is transformed completely to k - ϵ model from the boundary layer edge onward with blending in between facilitated by

blending functions. The k - ω SST model also incorporates a modification to the k - ω portion of the model that accounts for transport of the principal turbulent shear stress to avoid a strong freestream sensitivity that was present in the earlier k - ω model of Wilcox [26] [25]. The transport equations for the k - ω SST model are listed below, equation (8) through equation (15). The turbulent kinetic energy is represented by k and ω is the specific turbulent dissipation rate where ω is proportional to ε/k . P is the production of turbulent kinetic energy term. F_1 and F_2 are the blending functions. S is the strain rate tensor which includes the Favre-averaged strain rate tensor S_{ij} . The surface normal coordinate is represented by y . $a_1, \beta, \beta^*, \sigma_k, \sigma_\omega, \sigma_{\omega 2}, \gamma$ are all empirical constants sometimes referred to as closure coefficients and are determined by experiment, dimensional analysis and heuristics.

$$\frac{\partial k}{\partial t} + U_j \frac{\partial k}{\partial x_j} = P - \beta^* k \omega + \frac{\partial}{\partial x_i} \left[\left(\nu + \sigma_k \nu_t \right) \frac{\partial k}{\partial x_i} \right] \quad (8)$$

$$\begin{aligned} \frac{\partial \omega}{\partial t} + U_j \frac{\partial \omega}{\partial x_j} = & \gamma \frac{1}{\mu_t} P - \beta \omega^2 + \frac{\partial}{\partial x_i} \left[\left(\nu + \sigma_\omega \nu_t \right) \frac{\partial \omega}{\partial x_i} \right] + 2(1 \\ & - F_1) \sigma_{\omega 2} \frac{1}{\omega} \frac{\partial k}{\partial x_i} \frac{\partial \omega}{\partial x_i} \end{aligned} \quad (9)$$

$$\nu_t = \frac{a_1 k}{\max(a_1 \omega, S F_2)} \quad (10)$$

$$S = \sqrt{2 S_{ij} S_{ij}} \quad (11)$$

$$P_k = \tau_{ij} \frac{\partial U_i}{\partial x_j} \quad (12)$$

$$F_1 = \tanh \left[\left\{ \min \left\{ \max \left(\frac{\sqrt{k}}{\beta^* \omega y}, \frac{500\nu}{y^2 \omega} \right), \frac{4\rho\sigma_{\omega 2} k}{CD_{k\omega} y^2} \right\} \right\}^4 \right] \quad (13)$$

$$F_2 = \tanh \left[\left\{ \max \left(\frac{2\sqrt{k}}{\beta^* \omega y}, \frac{500\nu}{y^2 \omega} \right) \right\}^2 \right] \quad (14)$$

$$CD_{k\omega} = \min \left(2\rho\sigma_{\omega 2} \frac{1}{\omega} \frac{\partial k}{\partial x_i} \frac{\partial \omega}{\partial x_i}, 10^{-20} \right) \quad (15)$$

See reference [25] for a complete description of the k - ω SST model including the closure coefficient values.

3.2 Lag elliptical blending k - ε turbulence model

This section briefly describes the formulation of the Lag elliptical blending (EB) k - ε turbulence model which was used in this study. According to the developers Lardeau and Billard this new model is able to predict the misalignment of the principal components of the strain and stress tensors. This is a three equation model and incorporates some of the aspects of RSM models to account for the misalignment of stress and strain. This model is based on the Elliptical Blending Reynolds Stress model and according to the authors requires no further calibration since its constants are derived directly from that model [27]. The transport equations for the Lag elliptical blending k - ε turbulence model are listed below as equation (16) through equation (25) where k and ε are the turbulent kinetic energy and turbulent energy dissipation respectively. T , T_s , and L represent time and length scale respectively. S and S_{ij} are the strain rate tensor and Favre-averaged strain rate tensor respectively. The following are all empirical constants of the model: $C_k, C_{P1}, C_{P2}, C_{P3}, C_t, C_{\varepsilon 1}, C_{\varepsilon 2}, C_\mu, C_\eta, C_\omega^*, \widetilde{C}_1, C_1^*, CL, \sigma_\varepsilon, \sigma_k, \sigma_\varphi$.

$$\frac{Dk}{Dt} = P - \varepsilon + \frac{\partial}{\partial x_j} \left[\left(\frac{\nu}{2} + \frac{\nu_t}{2} \right) \frac{\partial k}{\partial x_j} \right] \quad (16)$$

Where P is the production of turbulent energy and ν and ν_t are the kinematic fluid viscosity and the eddy turbulent viscosity respectively.

$$\frac{D\varepsilon}{Dt} = C_{\varepsilon 1} \frac{P\varepsilon}{k} - E - C_{\varepsilon 2}^* \frac{\varepsilon^2}{k} + \frac{\partial}{\partial x_j} \left[\left(\frac{\nu}{2} + \frac{\nu_t}{\sigma_\varepsilon} \right) \frac{\partial \varepsilon}{\partial x_j} \right] \quad (17)$$

Where E is referred to as the E term. It was originally proposed by Jones and Launder to account for viscous wall effects [28].

$$\frac{D\varphi}{Dt} = (1 - \alpha^3)f_\omega + \alpha^3 f_\eta - C_{p1} \frac{P}{k} \varphi + \frac{\partial}{\partial x_j} \left[\left(\frac{\nu}{2} + \frac{\nu_t}{\sigma_\varphi} \right) \frac{\partial \varphi}{\partial x_j} \right] \quad (18)$$

Where the reduced stress function is represented by φ and α is a non-dimensional coefficient that represents the Lag effect on eddy viscosity and is found from solving the elliptic differential equation (19). The elliptic relaxation equations are solved to find f_ω and f_η .

$$L^2 \nabla^2 \alpha = \alpha - 1 \quad (19)$$

$$E = -2C_k \nu \nu_t (1 - \alpha)^3 \left(\frac{\partial \parallel 2S_{ij}n_j \parallel n_k}{\partial x_k} \right)^2 \quad (20)$$

$$f_\eta = C_\omega^* \varphi \frac{\varepsilon}{k} \quad (21)$$

$$f_{\omega} = \left(\overline{C}_1 + C_1^* \frac{P}{\varepsilon} \right) \frac{\varphi}{\tau} + C_{P2} \varphi S + C_{P3} \frac{1}{\tau} + \tau_S M_{ij} S_{ij} \quad (22)$$

M_{ij} is expressed as a function of the anisotropy tensor in equation (22).

$$T_S = \frac{T}{\max(\eta^2, 1)} \quad (23)$$

Where η is the ratio between mean velocity strain and turbulence time-scales.

$$T = \sqrt{\left(\frac{k}{\varepsilon}\right)^2 + C_t \frac{v}{\varepsilon}} \quad (24)$$

$$L = CL \sqrt{\left(\frac{k}{\varepsilon}\right)^3 + C_{\eta}^2 \sqrt{\frac{v^3}{\varepsilon}}} \quad (25)$$

3.3 k - ε empirical coefficients

Recently, researchers have improved the prediction capability of RANS models through tuning the closure coefficients. Fu et al. [29] and Zhang et al. [30] provide examples of tuning the closure coefficients for the k - ω SST model. The k - ω SST model was used initially in the current study and select coefficients were tuned with little success in matching the experimental data. Those results are not included here. Closure coefficients for the Lag EB k - ε model were tuned and studied more closely in the present study. To the knowledge of the author, there are no published studies for adjusting closure coefficients for the Lag EB k - ε model. Tuning studies have been published for the standard k - ε model.

Jones and Launder present values of the empirical constants (or closure coefficients) of C_μ , $C_{\varepsilon 1}$, $C_{\varepsilon 2}$, σ_ε and σ_k in their original definition of the k - ε model [28]. The original equations of the k - ε model are given below in equation (26) through equation (28). Equation (26) is referred to as the turbulence energy equation and equation (27) is the energy dissipation equation. “The terms which contain σ_ε and σ_k represent the diffusion rates of k and ε respectively [28].” As before k is the turbulent kinetic energy; ε is turbulent energy dissipation rate. μ and μ_τ are the dynamic viscosity and the turbulent viscosity respectively.

$$\rho \frac{Dk}{Dt} = \frac{\partial}{\partial y} \left[\left(\mu + \frac{\mu_t}{\sigma_k} \right) \frac{\partial k}{\partial y} \right] + \mu_\tau \left(\frac{\partial u}{\partial y} \right)^2 - \rho \varepsilon - 2\mu \left(\frac{\partial k^{1/2}}{\partial y} \right)^2 \quad (26)$$

$$\rho \frac{D\varepsilon}{Dt} = \frac{\partial}{\partial y} \left[\left(\mu + \frac{\mu_t}{\sigma_\varepsilon} \right) \frac{\partial \varepsilon}{\partial y} \right] + c_{\varepsilon 1} \frac{\varepsilon}{k} \mu_\tau \left(\frac{\partial u}{\partial y} \right)^2 - c_{\varepsilon 2} f_2 \frac{\rho \varepsilon^2}{k} + 20\mu\mu_\tau \left(\frac{\partial^2 u}{\partial y^2} \right)^2 \quad (27)$$

$$\mu_\tau = c_\mu \rho k^2 / \varepsilon \quad (28)$$

The under-prediction of turbulent kinetic energy by RANS models which results in an insufficient amount of turbulent mixing and an over-prediction of separated flow structure size has been noted by Ashton et al. for realistic shaped automotive models [31]. Since a disc is also a bluff body characterized by separation, reattachment, and trailing edge counterrotating vortices (much like a car body), it is expected that RANS CFD simulations of discs would over-predict the size of the separation region as well. Poroseva and Bezdard tuned the standard k - ε model with the $C_{\varepsilon 1}$, σ_ε , and σ_k coefficients to match experimental results for a wake, mixing layer, plane jet, round jet, and four boundary layers

[32]. Comparisons of shear stress profiles, velocity profiles, and turbulent kinetic energy profiles were the evaluation criteria for coefficient selections. Specific values of $C_{\varepsilon 1}$ were arrived at for each case. Rather than specific values of σ_{ε} and σ_k , the ratio of these two values was found to be important. Since a disc is a bluff body characterized largely by separated flow, the wake values from Poroseva and Beazard were trialed with the Floater calibration disc after the initial runs with the non-tuned Lag EB k - ε model. For the standard k - ε model in STAR-CCM+, the values of $C_{\varepsilon 1}$ and $\sigma_{\varepsilon}/\sigma_k$ are 1.44 and 1.2 respectively. Poroseva and Beazard found that values of $C_{\varepsilon 1}=1.2$ and $\sigma_{\varepsilon}/\sigma_k=1.8$ match the data best for the wake. Although Poroseva and Beazard recommend specific values for each of the canonical cases tested for $C_{\varepsilon 1}$ and $\sigma_{\varepsilon}/\sigma_k$, distinct reasoning is not elucidated in the study except for demonstrating a closer match to the experimental data. The recommended wake values from Poroseva and Beazard were used for the current study. The tuned model will now be referred to as the Lag EB k - ε tuned model and the standard model will be referred to as simply the Lag EB k - ε model in this paper.

3.4 Detached eddy simulation

Detached eddy simulation (DES) which is a hybrid approach using both LES and RANS, falls in between these two approaches in terms of expense and complexity. LES is used where there are large separated flows far from the surface and RANS is used to model turbulence in attached flows. The switch between RANS and LES is governed by the turbulent length scale and grid spacing. Although DES has shown to be very promising in some simulations, it is still an emerging technique. The creation of suitable grids is something of an art [33].

Given the emerging state of DES and the fact that its less accessible to golf disc design engineers, RANS simulations were completed for the majority of this study. The DES runs were seen as a first foray into a hybrid RANS-LES approach with the Lag EB k - ϵ turbulence model.

The Lag EB k - ϵ model was used for all DES runs. The Lag EB k - ϵ model is implemented as a delayed detached eddy simulation (DDES) in STAR-CCM+ [33]. Interestingly, the standard STAR-CCM+ DES setting for σ_ϵ/σ_k is 1.5, whereas the standard RANS σ_ϵ/σ_k ratio is 1.2 in STAR-CCM+

CHAPTER 4. NUMERICAL SETUP

Seven disc shapes were used for this study. First a disc shaped more like a traditional Frisbee was modeled and then six golf disc drivers. The Frisbee shaped disc called the Floater is manufactured by Disc Dynamic. Three of the six golf disc drivers are commercially available. They were as follows: Quarter K by Discwing, Flick by Discraft, and Wraith by Innova. After the existing commercial discs were simulated, three new disc shapes were conceived and modeled by the author. This chapter includes the numerical setup for all disc simulations including the disc shapes, mesh, domain, boundary conditions, and physics parameters such as velocity and angles of attack.

The commercial CFD code STAR-CCM+ 13.04 was used for all meshing and simulations. All simulations were run on the UNCC Research Computing Group clusters. The clusters of Copperhead which has 96 nodes and 2060 computing cores and Sidewinder which has 29 nodes and 488 computing nodes were both used [34]. Seven disc shapes were evaluated. Potts published extensive wind tunnel data for the Floater disc which included force and moment coefficients, pressure profiles, and flow visualization for many angles of attack. Given this, the Floater disc was used for the mesh refinement study, turbulence model selection, and turbulence model calibration. The Floater disc is more akin to a beach Frisbee and has a larger cavity and more blunt leading and trailing edge surfaces and therefore more regions of flow separation than typical golf discs which tend to be more streamlined in shape. If CFD turbulence models can be tuned to match the experimental data from the blunt Floater disc, the models would presumably perform remarkably well for the more streamlined golf discs. The Floater calibration disc was also run in DES mode at three angles of attack. Next three commercially available golf discs

for which Kamaruddin published experimental data were simulated [12]. These discs were primarily simulated to evaluate the effectiveness of the CFD methods and tuning for actual commercially available golf discs. Finally, three new disc designs were conceived by the author and evaluated using the same CFD method and tuned turbulence model.

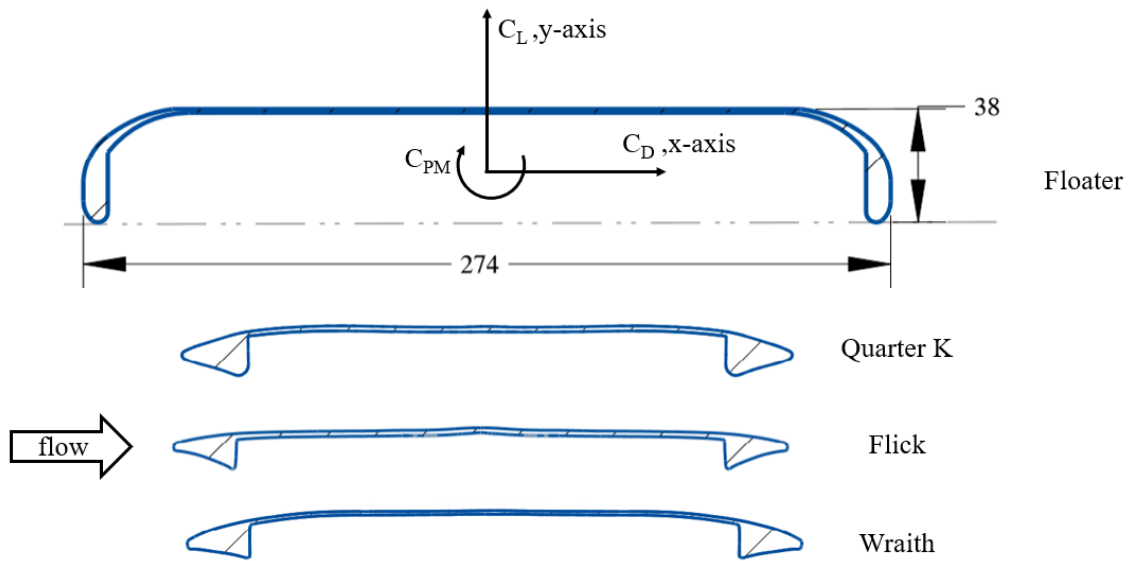
4.1 Disc shapes – existing discs

TABLE 4.1 and FIGURE 4.1 display dimensions and information for the existing commercially available discs used in this study. The disc images in FIGURE 4.1 are scaled proportionally correct to each other and show the location of the aerodynamic force and moment coefficient coordinate system which is mid diameter and mid thickness for all discs. Note, all coefficients are reported at the wind axis; that is, the coordinate system is always parallel to the nominal flow direction from the inlet. Flow is from left to right in TABLE 4.1. The Floater disc surface model was created in Creo Parametric CAD software using the dimensions and figures from Potts [2]. The three golf discs were purchased and scanned by Mr. Kevin Rau of Digital Reality using a GOM ATOS blue light scanning unit. After the surface files were received from Digital Reality, they were imported into Creo Parametric, reverse engineered, and exported as neutral files for use in STAR-CCM+.

TABLE 4.1. Disc dimensions – existing discs

Disc Name	Manufacturer	Disc Type	Diameter (mm)	Thickness (mm)
Floater	Disc Dynamics	Frisbee (“calibration” disc for this study)	274	38
Quarter K	Discwing	commercial golf discs, drivers	213	20
Flick	Discraft		211	13
Wraith	Innova		211	14

FIGURE 4.1. Disc Dimensions and Shape – existing discs



4.2 Disc shapes – new design concepts

Three new discs concepts were created and evaluated in CFD for this study. All disc surfaces were created in Creo Parametric, exported as neutral files and then meshed in STAR-CCM+. PDGA disc rules and production feasibility were not closely considered for the new designs. Breakthrough concepts are often discovered when freeform thinking is used. Even if the new shapes are not physically feasible, the learnings from these shapes may lead to viable improved designs. FIGURE 4.2, FIGURE 4.3, and FIGURE 4.4 show the new disc designs 1, 2, and 3 respectively. All discs started with the Wraith golf disc shape. Disc 1 is the Wraith disc shape with a 3 mm tall circular protrusion added to the top surface and blended at the perimeter back into the top surface of the disc. As a child, the author recalls owning a Frisbee with a raised center section that glided for a long distance. To test this concept, a feature was added to the top of the Wraith disc as shown. Disc 2 retained the upper surface of Disc 1 (circular protrusion) but with a radically redesigned bottom surface lip. After observing flow direction at 0 degrees and 10 degrees angle of attack using the CFD results from this study, it was hypothesized that the lower lip could be designed to increase lift and negligibly affect the pitch moment compared to the Wraith disc. It appears that if the lower lip of the Wraith were flatter and not concave, higher energy flow would be directed downward thereby creating more lift at 0 degrees angle of attack. Reshaping of this lip could lead to more flow impinging on the back inner lip at higher angles of attack. To potentially address this, the vertical surface was made smaller by the removal of material on the inside of the rim. The thought was to reduce the area of vertical surface available for impinging flow to act on. For the Disc 3 design, the author found a picture of the Aerobie disc and designed a lip that resembled the Aerobie

lip. The Aerobie holds the Guinness World Record for the longest throw of an object at 406 meters [35]. Except for Disc 2, very little scientific reasoning was used for conception of the new designs. The paper focused more on the CFD method. Future research will focus on disc design.

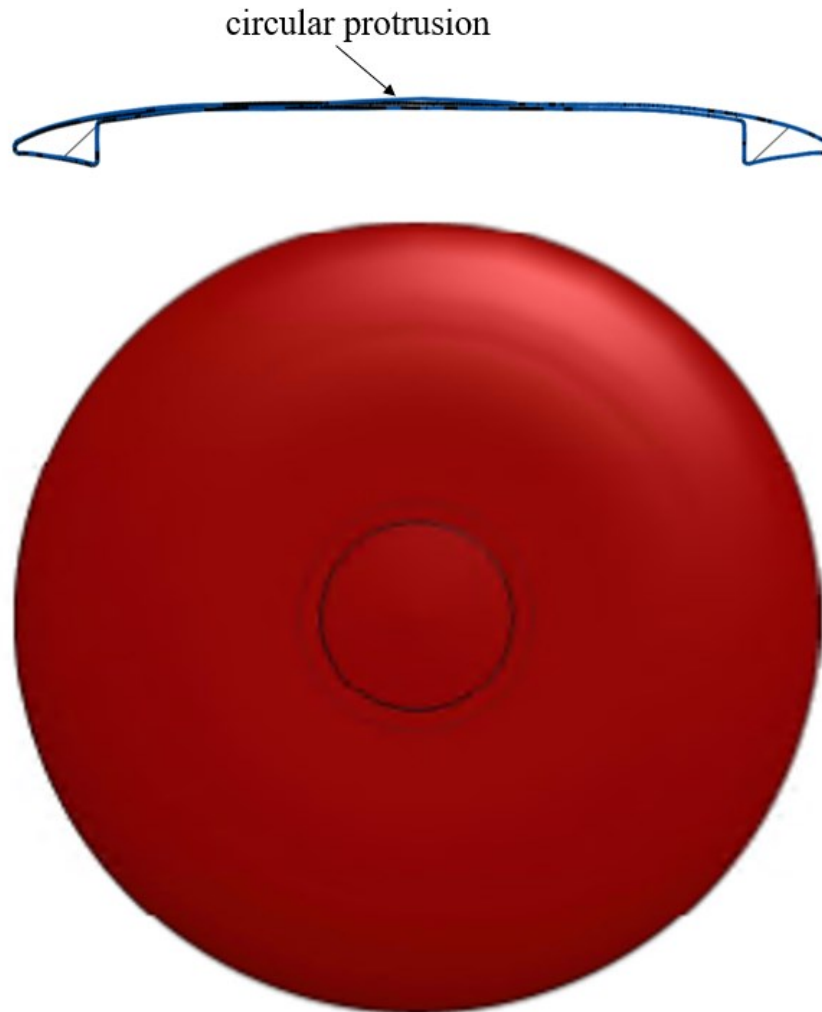


FIGURE 4.2. Disc 1



FIGURE 4.3. Disc 2

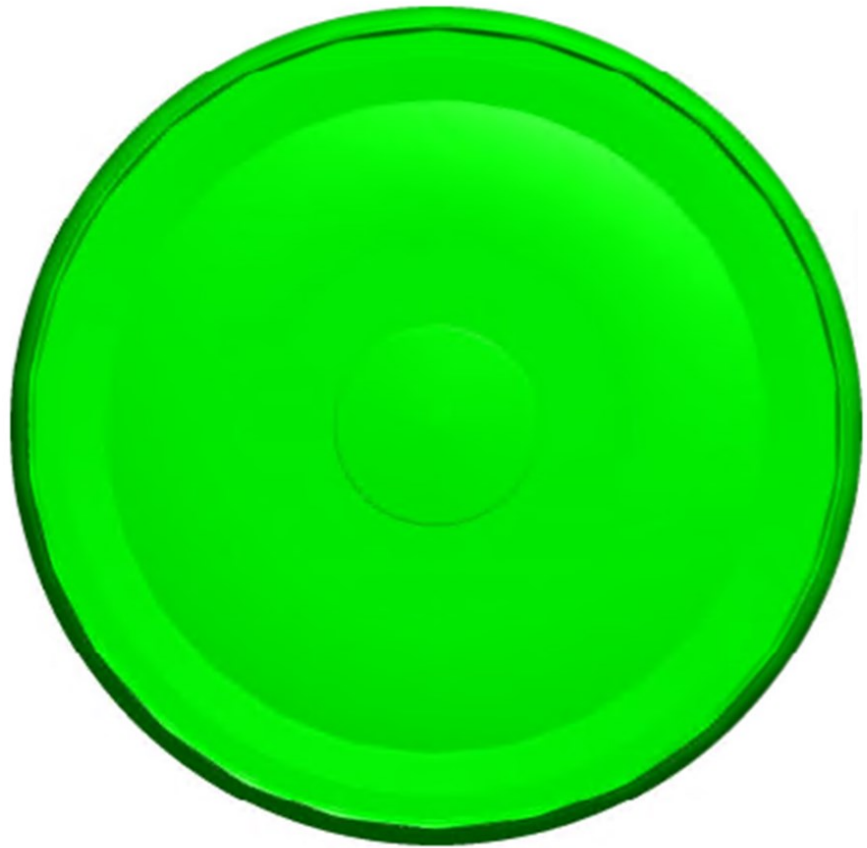


FIGURE 4.4. Disc 3

4.3 Computational domain and boundary conditions

The proportions of the computational domain relative to the calibration disc are shown in FIGURE 4.5. The blockage ratio for the calibration disc was 0.2% and it was verified that velocity in the vicinity of the disc was not affected by the walls during results post-processing. Half disc models were used for all cases since the discs are symmetric. A velocity inlet boundary condition was used at the entrance. The far wall was a symmetry plane. The near wall boundary condition was wall. For 0 degree angle of attack runs, the floor and ceiling were classified as walls. For nonzero angle of attack runs, the floor was classified as velocity inlet and the ceiling was a pressure outlet and the inlet and floor velocity directions matched the intended angle attack of the disc, but the disc remained parallel to the tunnel floor and ceiling for all cases. The aft exit (right side of FIGURE 4.5) used the pressure outlet boundary condition. Pressure outlet conditions were set to zero gauge pressure for all runs.

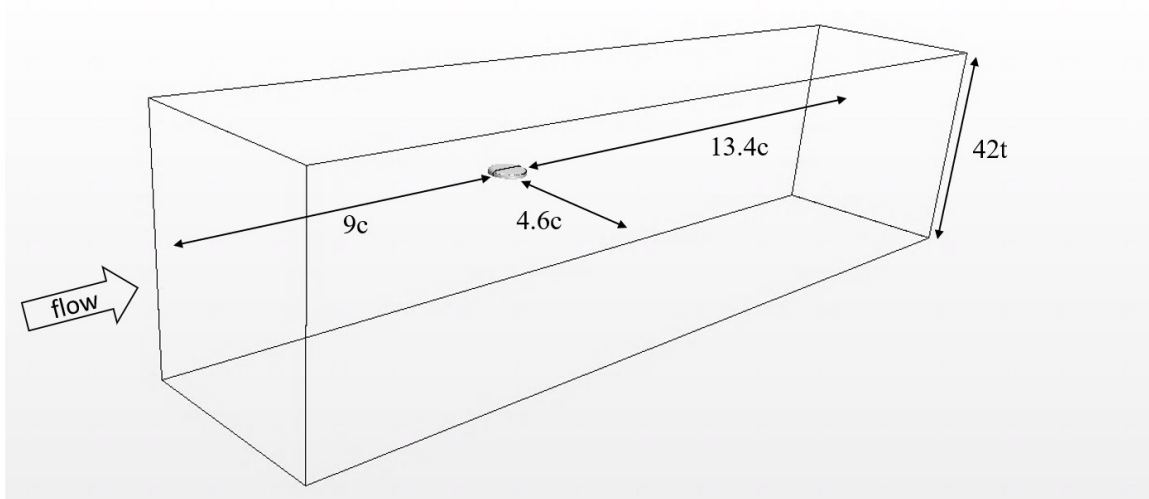


FIGURE 4.5. Computational domain

4.4 Prism layers

“Prism layers allow the solver to resolve near wall flow accurately, which is critical in determining not only the forces and heat transfer on walls, but also flow features such as separation [36]”. The all y^+ wall treatment for wall functions was chosen for all simulations. A y^+ of less than one and a total prism layer thickness that would encompass most of the large gradients present in the boundary layer was achieved using the following procedure. First, the boundary layer thickness for a flat plate was estimated using the turbulent boundary-layer growth equation from Prandtl [37], $\delta=0.37c/Re^{1/3}$ where c is the chord length or diameter in the case of a disc. Based on this calculation, a total prism layer thickness of approximately 5 mm was used. The first node thickness was calculated using $y=y^+/Re(c_f/2)^{1/2}$ from reference [38]. Also, from reference [38], skin friction was estimated as $c_f=0.455/\ln(0.06Re)^2$. Choosing $y^+ = 0.05$, a first node thickness of 0.001 mm was calculated and utilized for all simulations. During results post-processing, results y^+ values were verified to be less than 1.0.

4.5 Core mesh

STAR-CCM+ trim cell mesh was used for the core mesh. The core mesh was subdivided into four major zones shown in FIGURE 4.6. The cell size nominally doubles in size from zone to zone. FIGURE 4.7 displays a top section view of the mesh at mid-disc thickness. Refinement zone C extended 4.3 diameters aft of the disc trailing edge. During a mesh refinement study on the Floater calibration disc, two additional zones were added to the top surface and rim of the disc for the medium mesh (M27) to create the medium targeted mesh (M31) shown in FIGURE 4.8 (bottom image). Models ranged in size from 2.3 million cells to 25.3 million cells. TABLE 4.2 contains details of each mesh.

The mesh refinement study was performed in both RANS (4 meshes) and DES (3 meshes) with the Floater calibration disc. The coarse, medium, medium targeted and fine mesh were all tested in RANS mode. Only the coarse, medium, and medium targeted were run in DES mode. The next section contains the details of the DES mesh refinement design.

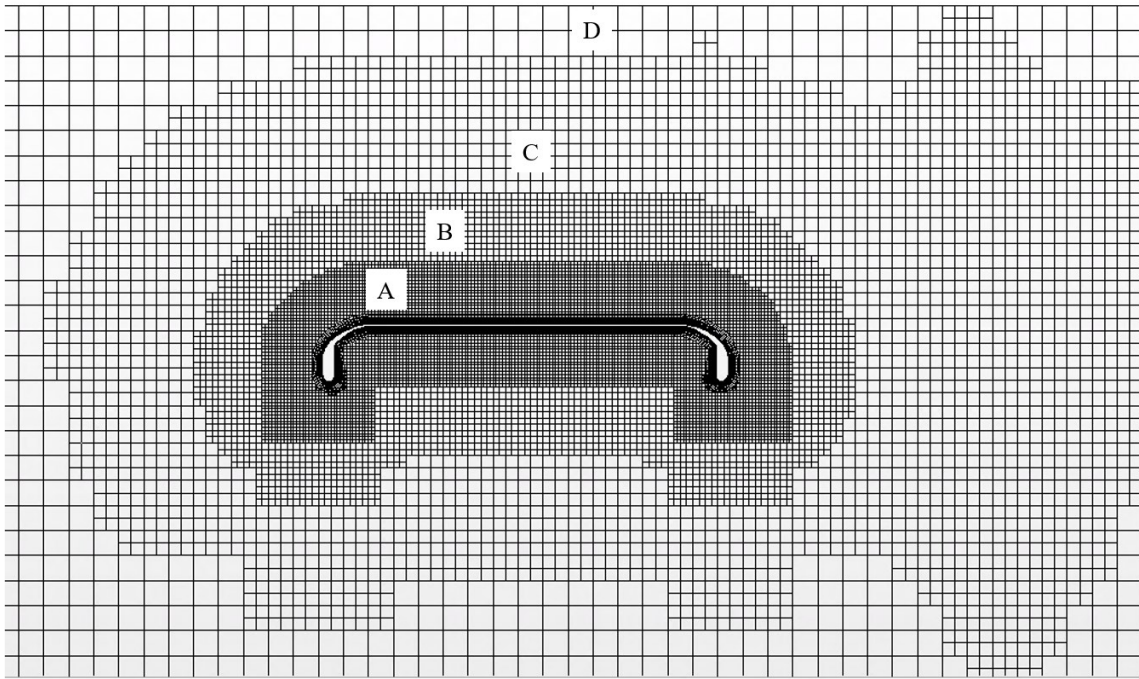


FIGURE 4.6. Mesh refinement zones at center span. Air flow direction is from left to right.

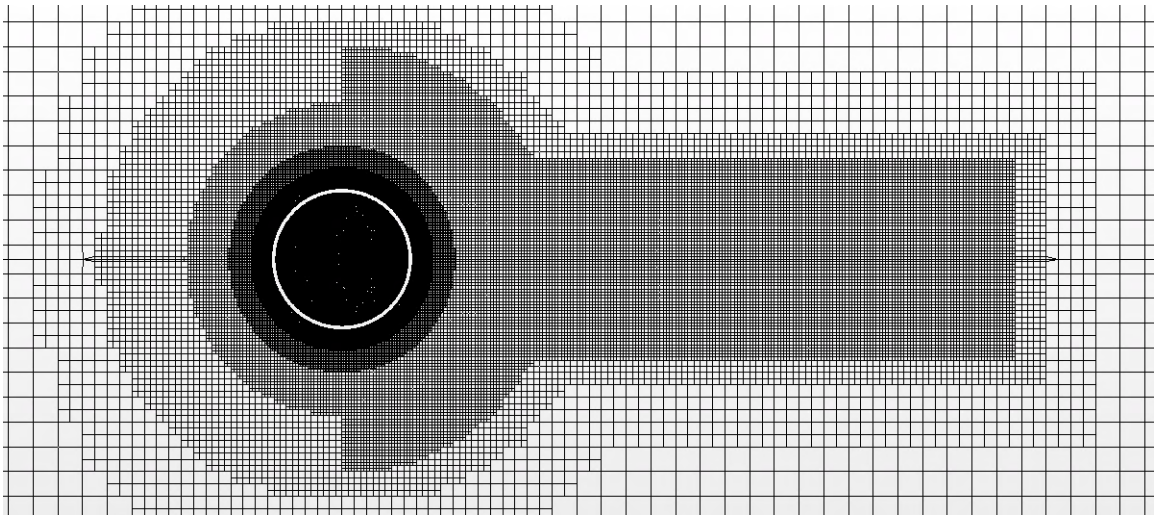


FIGURE 4.7. Mesh top section view at mid-disc thickness

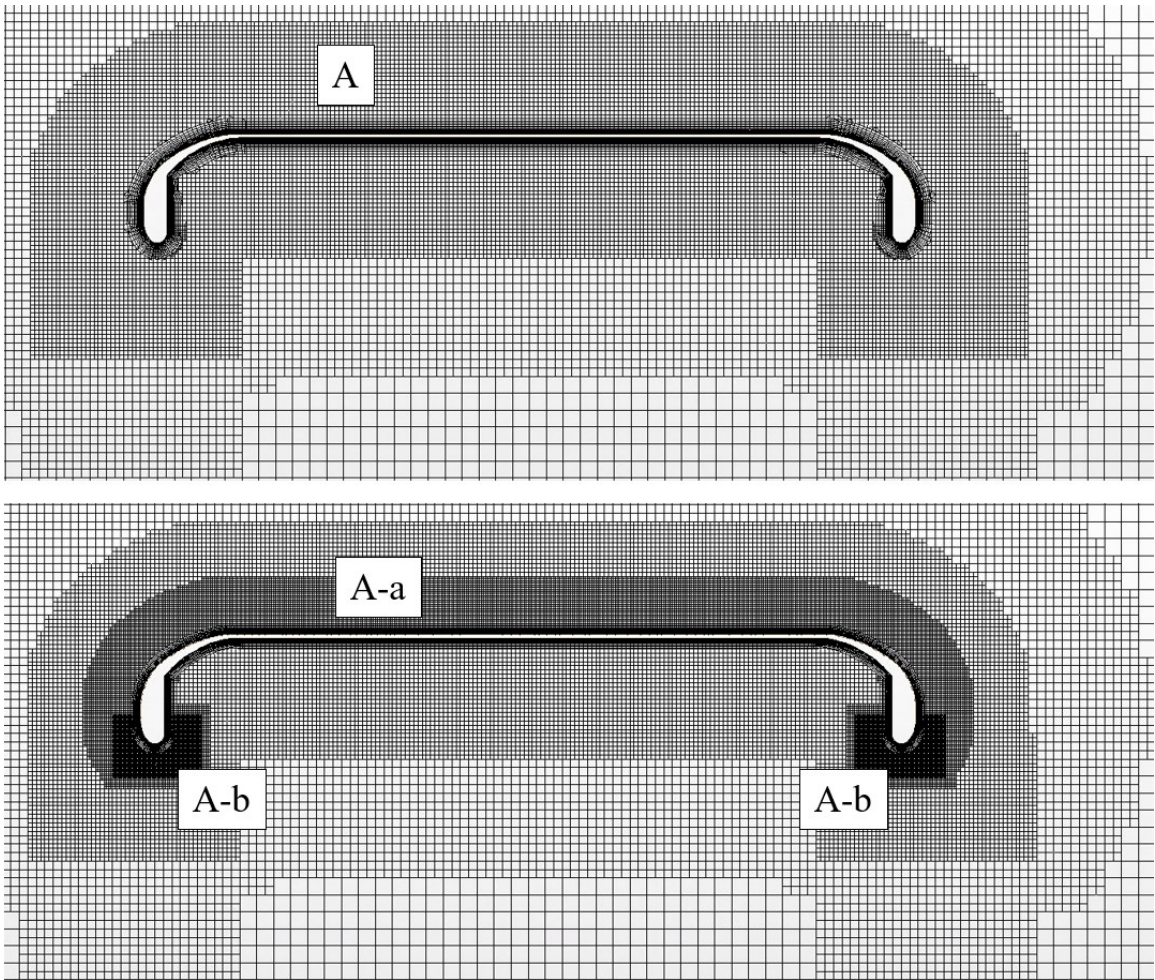


FIGURE 4.8. Medium (M27) mesh top and medium targeted (M31) mesh bottom.
Center span.

TABLE 4.2. Mesh details – Floater calibration disc

Mesh Name	Number of prism layers	First prism layer cell thickness (mm)	Prism layer thickness (mm)	A (mm)	B (mm)	C (mm)	D (mm)	Cell Count (10 ⁶)
Coarse (M29)	37	0.00109	5.6	2.1	4.2	8.4	16.8	2.3
Medium (M27)	41	0.00109	5.6	1.5	3	6	12	4.4
Medium targeted (M31)	40	0.00109	3.4	A:1.5 A-a: 0.75 A-b:0.4	3	6	12	17.0
Fine (M28)	41	0.00109	6.8	0.9	1.8	3.6	7.2	25.3

4.6 DES mesh refinement – Floater calibration disc

For DES mode, a mesh convergence study was performed by holding the time step constant at 0.079 FTT (flow through times) and varying the mesh. The results of the study are included in the results chapter; the details of the mesh design are included here. The M27 or medium mesh used for most of the RANS simulations was the starting mesh for this exercise. Since there is likely separated flow around the bottom of the disc rim and on the top surface of the disc, the M31 mesh (bottom of FIGURE 4.8) was generated to compare against the first DES run of the M27 mesh. Mesh refinement should allow the DES to take advantage of the LES capabilities of the DES model formulation and improve the prediction of flow structures in these challenging areas. Mesh size in these target areas was estimated following a procedure used by Ashton and Revell [39]. First the Kolmogorov length-scale is estimated using $\eta=(\nu^3/\varepsilon)^{1/4}$, where ν is the dynamic viscosity of the fluid. The turbulent dissipation rate ε is obtained from the RANS simulation of the

Floater disc for the Lag EB $k-\epsilon$ at 10 degrees angle of attack, FIGURE 4.9. To maintain a practical model size, a maximum value of $5500 \text{ m}^2/\text{s}^3$ was chosen. Fröhlich et al. recommend a target value of 12 times the Kolmogorov scale for large eddy simulation [22]. Based on these calculations, where practical, a target cell size of 0.4 mm was used for the M31 mesh, FIGURE 4.8, zone A-b. Recall that cells in zone A of M27 were nominally 1.5 mm. The M29 coarse mesh was also ran in DES mode.

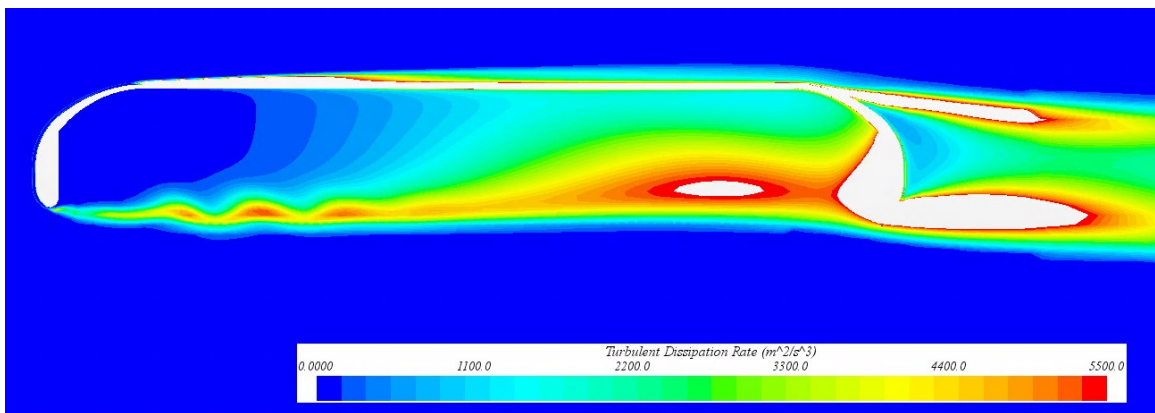


FIGURE 4.9. Turbulent dissipation rate for the Floater calibration disc at center span. Lag EB $k-\epsilon$, $\text{AoA}=10^\circ$.

4.7 Golf discs' mesh

All mesh settings in STAR-CCM+ remained the same for the golf discs as they were for the Floater calibration disc. The golf discs are all smaller than the Floater disc, so outer portions of the mesh remained much the same. FIGURE 4.10 shows the Wraith golf disc with the medium mesh (M27). All golf disc meshes contained about 7 million cells. The more intricate geometry of the golf discs compared to the Floater calibration disc resulted in more cells near the disc surface.

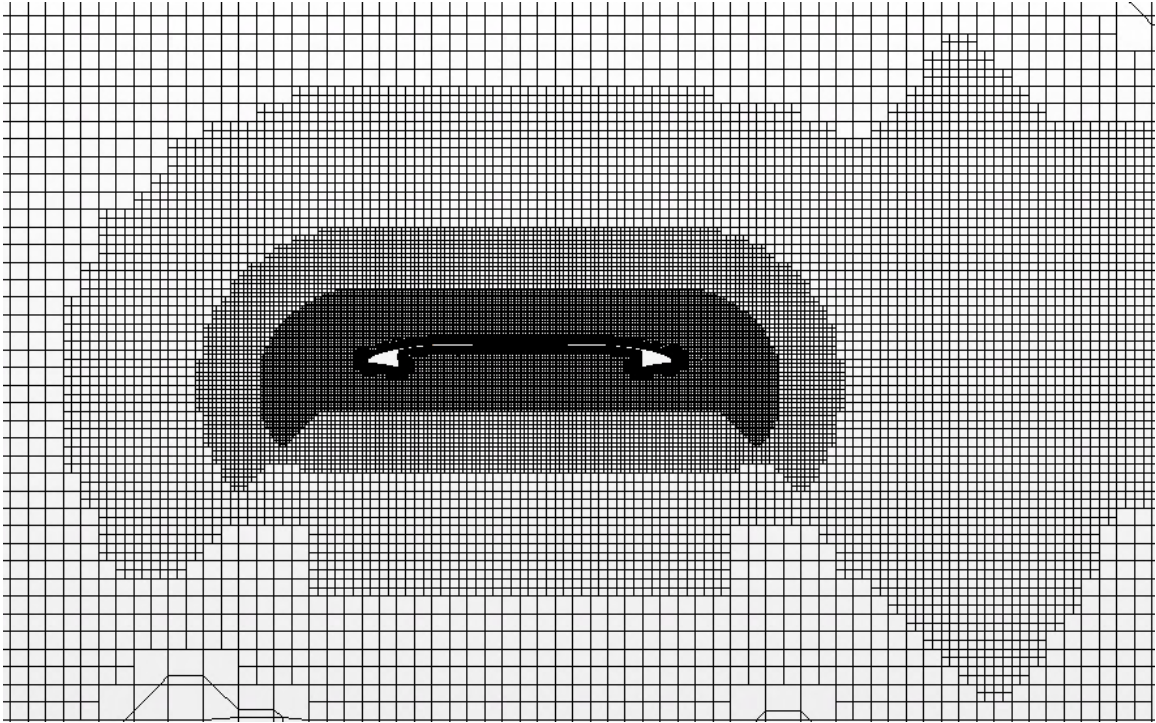


FIGURE 4.10. Wraith golf disc with medium mesh. Center span.

4.8 Physics setup – RANS and DES

To match the wind tunnel data, disc spin was not included in the CFD runs. Previous studies have shown that disc spin has a negligible aerodynamic effect [2]. The wind tunnel strut was not modeled since its effects were shown to be minimal [12]. To match the experimental data of Potts [2] and Kamaruddin [12], the Reynold's number was set to 380,700 (based on the disc diameter) for all cases. This corresponded to a free stream velocity of 21.6 m/sec for the Floater calibration disc and 28.0 m/sec for the 213 mm diameter golf disc and 28.2 m/sec for the 211 mm diameter golf discs. Note, Lissaman and Hubbard report that both professional and amateur disc golf players release discs at about 23 m/sec so the speeds used in the simulation and experiments are reasonable [9]. The

fluid density and kinematic viscosity are held at $\rho = 1.184 \text{ kg/m}^3$ and $\nu = 1.855 \times 10^{-5} \text{ Pa}\cdot\text{s}$ respectively. Turbulent intensity was set to 0.005 to match the reported level from the wind tunnel [2] [12]. The Floater calibration disc was run at 0, 10, and 20 degrees angle of attack to match corresponding angles for the experimental data of Potts [2]. To match corresponding points for the experimental data of Kamaruddin, all golf discs were run at 0, 10, and 15 degrees angle of attack [12]. The steady-state RANS simulations ran for 3000 iterations. All simulations converged as the residuals were reduced by several orders of magnitude and C_D , C_L , and C_{PM} were typically stable to the third decimal place. Regardless, all RANS results were averaged for the last 25 iterations. DES inner iterations varied between 5 and 7 depending on convergence but all runs of like time-step maintained an equal quantity of inner iteration. DES runs were deemed initially converged (prior to mesh and time-step convergence testing) when residuals for inner iterations were reduced by several orders of magnitude. All DES runs were started with a converged RANS solution of the same mesh and turbulence model. The LETOTs varied between 79 and 197. LETOTs were changed during the time-step study to save resources. This is detailed in the results chapter.

For RANS simulations, three different turbulence models were used: $k-\omega$ SST, Lag EB $k-\varepsilon$, Lag EB $k-\varepsilon$ tuned. The $k-\omega$ SST closure coefficients were not changed from the STAR-CCM+ default values. The Lag EB $k-\varepsilon$ standard closure coefficients also retained their default values of 1.44 and 1.2 for $C_{\varepsilon 1}$ and $\sigma_{\varepsilon}/\sigma_k$, respectively. For the Lag EB $k-\varepsilon$ tuned model $C_{\varepsilon 1}$ and $\sigma_{\varepsilon}/\sigma_k$ were set to 1.2 and 1.8 respectively as recommended by Poroseva and Bezdard for a wake for the standard $k-\varepsilon$ model [32]. For DES, the Lag EB

k - ε model was used with its default STAR-CCM+ settings. Interestingly $\sigma_\varepsilon/\sigma_k = 1.5$ by default instead of the standard 1.2 used for RANS.

4.9 Additional angles of attack

Near the conclusion of the study, at the suggestion of one of the reviewers, additional angle of attack runs were made with the Lag EB k - ε tuned turbulence model in RANS mode for the Floater calibration disc and the three commercial golf discs. For the Floater calibration disc, the angles of -10, -5, and 5 degrees were added. For the commercial golf discs, -5, and 5 degrees were added.

CHAPTER 5. RANS RESULTS

Results for all RANS simulations are included in this chapter. This includes the results for the Floater calibration disc, the Quarter K, Flick, and Wraith commercial golf discs as well as the three new golf disc designs concepts. Numerous force and moment coefficient plots and pressure profile plots (CP v. span or chord both non-dimensionalized by diameter) are presented comparing discs and turbulence models. The results of the RANS mesh refinement study are also included here. Comparative analysis between turbulence models and discs are also made.

5.1 Mesh refinement study

Aerodynamic coefficients were not sensitive to mesh density for the ranges tested, TABLE 5.1. The medium mesh was chosen for the majority of this study since it achieved adequate resolution and virtually matched the force and moment coefficients of the fine mesh at one-sixth the model size. The coarse mesh would have been sufficient for RANS, but since the medium mesh only contained 4.4 million cells, a very manageable size for the available hardware, it was chosen. Additionally, it was anticipated that the medium mesh would also prove sufficient during the DES mesh study and that the coarse would not. Also, if the medium mesh could be used for the majority of the RANS and DES simulations, it could be eliminated as a variable.

TABLE 5.1. RANS mesh refinement study results

AoA (degrees)	Mesh name	Mesh no.	C_D	C_L	C_{PM}
0	coarse	M29	0.058	0.017	0.001
	medium	M27	0.059	0.018	0.001
10	coarse	M29	0.138	0.438	0.031
	medium	M27	0.138	0.439	0.031
	fine	M28	0.142	0.445	0.029
	medium targeted	M31	0.135	0.432	0.033
20	coarse	M29	0.424	0.952	0.025
	medium	M27	0.423	0.951	0.026

5.2 Floater calibration disc

FIGURE 5.1 displays force and moment coefficients verses angle of attack for the Floater calibration disc for experiment, $k-\omega$ SST, Lag EB $k-\epsilon$, and the Lag EB $k-\epsilon$ tuned models. As previously stated, since extensive data was published by Potts [2] for the Floater disc, it was used as a calibration tool for this study. Prediction of C_D and C_L compared to the experimental data are successively improved when stepping from the $k-\omega$ SST to the Lag EB $k-\epsilon$ and finally to the Lag EB $k-\epsilon$ tuned model for all angles of attack. As expected, the CFD results more closely matched the experimental results at lower angles of attack where separation and reattachment are less predominant. The pitch moment (C_{PM}) curves did not match experimental data well for any of the turbulence models. The CFD pitch moment curves more closely resemble the experimental pitch moment curves calculated from integrated pressure data. See FIGURE 5.2 below from reference [2]. To explore this further, the CFD pitch moments were recalculated and plotted with the pitch moment axis located at the bottom of the disc rather than the center, FIGURE 5.3. Although it cannot be determined conclusively if this adjustment is valid, the data do more closely match the experimental data with relocation of the pitch moment axis.

FIGURE 5.4 through FIGURE 5.15 display top and bottom surface pressure profiles at the centerline span, 1/4 span, 1/8th span, and 1/2 chord for both top and bottom surfaces of the disc at 0, 10, and 20 degrees angle of attack for experiment and all three turbulence models. CFD curves are solid lines and experimental curves from Potts [2] are the broken lines. The $k-\omega$ SST turbulence model is the top plot of each figure, Lag EB $k-\epsilon$ is in the center, and Lag EB $k-\epsilon$ tuned is in the bottom. Black colored curves are for the top surface of the disc and red colored curves are the bottom surface. Dr. Potts provided an electronic image of Figure 5.33 from [2] via email from which the experimental curves were obtained. The original experimental curves were interpolated from a fine grid of pressure ports spaced at 0.5 mm [2]. For this paper, the experimental curves were captured from the provided image using a MATLAB point capture program. User inputs included the minimum and maximum axes values and clicks on the axis's extremes and desired data points with the computer mouse. Although not quantified, it is reasonable to expect that some error was created in acquiring the pressure profiles in this manner.

Although data for 0 and 20 degrees angle of attack were also plotted and analyzed, the 10 degree angle of attack was the main focus for calibrating the turbulence model. According to the simulation results of Kamaruddin, maximum range of a driver golf disc is obtained with a release angle of about 10 degrees [12]. The 10 degree angle of attack curves are analyzed in the following paragraph.

For 10 degrees, all turbulence models captured the stagnation point with a CP of 1.0 at the leading edge. Although all turbulence models captured the top front suction peak ($x/c \sim 0.05$), none captured the shape correctly. Between $x/c \sim 0.05$ and 0.2, the experimental data shows a suction peak, separation, and then a reattachment evidenced by the double

hump circled in FIGURE 5.8. All models captured the first low pressure peak and have a narrow spike aft of this peak, but none captured the rear plateau correctly compared to experimental data. All models performed reasonably well for the top center portion of the disc where the flow has reattached and a boundary layer is formed. At the aft of the top surface, the $k-\omega$ SST predicted the rear suction peak faintly; the Lag EB $k-\varepsilon$ was more accurate in this region. More accurate prediction of this prominent feature led to the choice of the Lag EB $k-\varepsilon$ for this study. Consequently, once the rear suction peak was more closely captured, the pitch moment coefficient more closely matched experimental data. The Lag EB $k-\varepsilon$ tuned model over-predicted the magnitude of the rear peak. All models calculated a narrow rear peak. Overall the Lag EB $k-\varepsilon$ tuned model improved the accuracy of the bulk of the upper surface pressure profile compared to the other models. For the bottom pressure profile curves, all three models appear very similar compared to experimental data for the front half of the disc. For the rear portion of the disc, the Lag EB $k-\varepsilon$ tuned model captures the behavior more accurately than the other models. The improved predictive capability of the Lag EB $k-\varepsilon$ tuned model is likely due to the more accurate prediction of turbulent kinetic energy in the wake which is discussed in subsequent paragraphs related to FIGURE 5.17. For the $1/4^{\text{th}}$ span pressure profiles in FIGURE 5.9, all models underpredicted the magnitude of the upper surface front suction peak. The tuned model is more accurate in magnitude and shape than the $k-\omega$ SST and standard Lag EB $k-\varepsilon$ models for the upper surface rear suction peak. Like the $1/2$ span profiles, all models look similar for the front lower surface of the disc, but the Lag EB $k-\varepsilon$ tuned model performs better at the rear of the disc. Consequently, the improved pressure profile prediction at the rear of the disc for the tuned model seemed to degrade the accuracy at the center. All models performed poorly

and similarly for the 1/8th span upper pressure profiles, FIGURE 5.10. Front upper surface prediction was better for all models compared to the rear. The Lag EB k - ϵ tuned model showed the least predictive capability for the lower surface. The 1/2 chord profiles, FIGURE 5.11, appear to show poor correlation for all models compared to experimental data, but this impression is driven in large part by the reduced axis size compared to the previous figures of chord profiles due to the smaller pressure variations from side to side compared to front to back. For the Lag EB k - ϵ tuned model, the top surface centerline pressure difference is about 25% from experiment. For the majority of the top surface, the Lag EB k - ϵ tuned model improved predictions by decreasing pressure compared to the other models. The opposite trend resulted on the bottom surface; increased pressure and degraded prediction.

Further analysis of behavior of interest for various plots is included here: The k - ω SST model failed to predict the centerline span pressure profiles for 0 degrees angle of attack. The upper center span rear pressure profile suction peak appeared faintly for 10 degrees; a bit stronger for 20 degrees but still did not match the experimental data. The Lag EB k - ϵ predicted a weak upper rear peak for 0 and 10 degrees angles of attack compared to experimental data but matched fairly well at 20 degrees. The Lag EB k - ϵ tuned model matched the experimental rear suction peak well in magnitude for 0 and was slightly high for 10 degrees, but overpredicted the magnitude substantially at 20 degrees angle of attack. Note that even when predicted, the rear suction peak was not as broad as the experimental data for any of the turbulence models. All turbulence models predicted the front suction peak well at 0 and 10 degrees but overpredicted the size of the peak at 20 degrees angle of attack. Strengthening of the rear surface suction peak for both versions

of the Lag EB $k-\varepsilon$ model was manifested in the pitch moment coefficient which decreased at all angles of attack as would be expected (FIGURE 5.1). Surprisingly, there were only minor differences among all turbulence models for the pressure profiles at 1/4th and 1/8th span for all angles of attack. In general, there was good agreement in shape among all turbulence models and the experimental data, but they all differed in magnitude from the experimental data by a similar amount for the 1/4th and 1/8th span data for each respective angle of attack. The 0 degree angle of attack data appears to deviate in magnitude more than the other angles for both top and bottom surfaces for all models. The 10 degree angle of attack data had the best overall average look for both the top and bottom. The 20 degree angle of attack data matched very well for the bottom surface pressure profiles, but although matching in general shape the top surface pressure magnitudes differed by as much as 50% in places. The 1/2 chord pressure profiles displayed similar trends as the 1/4th and 1/8th span profiles when compared to the experimental data but the magnitude deviated significantly in places compared to experimental data. Zero degree angle of attack overall showed the most deviation. Ten degree angle of attack was best on average. The 20 degree angle of attack data matched very well for the bottom and showed the most deviation on the top surface.

FIGURE 5.16 is a plot of velocity magnitude for all three turbulence models. The $k-\omega$ SST produced the largest wake followed by the Lag EB $k-\varepsilon$ and then the Lag EB $k-\varepsilon$ tuned model. There were no quantitative experimental data for direct comparison to the CFD wakes, but the Lag EB $k-\varepsilon$ tuned model did more closely match the centerline rear surface profile suction peak as well as the force and moment coefficients compared to the other models. It is therefore inferred that the Lag EB $k-\varepsilon$ tuned model more accurately

predicted the magnitude of turbulent kinetic energy in the separation region at the rear of the disc. FIGURE 5.17 does in fact show an elevated level of turbulent kinetic energy for the Lag EB k - ε tuned model compared to both the Lag EB k - ε standard model and the k - ω SST model. FIGURE 5.18 shows the vortices from the experimental data and CFD for both the k - ω SST model and the Lag EB k - ε tuned model. The vortices for the Lag EB k - ε tuned model were larger than those for the k - ω SST model. This further supports the assumption that the Lag EB k - ε tuned model more closely matched the correct level of turbulent kinetic energy in the separation regions. Also notice the decreased velocity at the core of the wake for the Lag EB k - ε tuned model compared to the k - ω SST model presumably manifested due to the smaller production of turbulent kinetic energy by the Lag model at the vortices cores as noted by the developers of the model for other configurations [27].

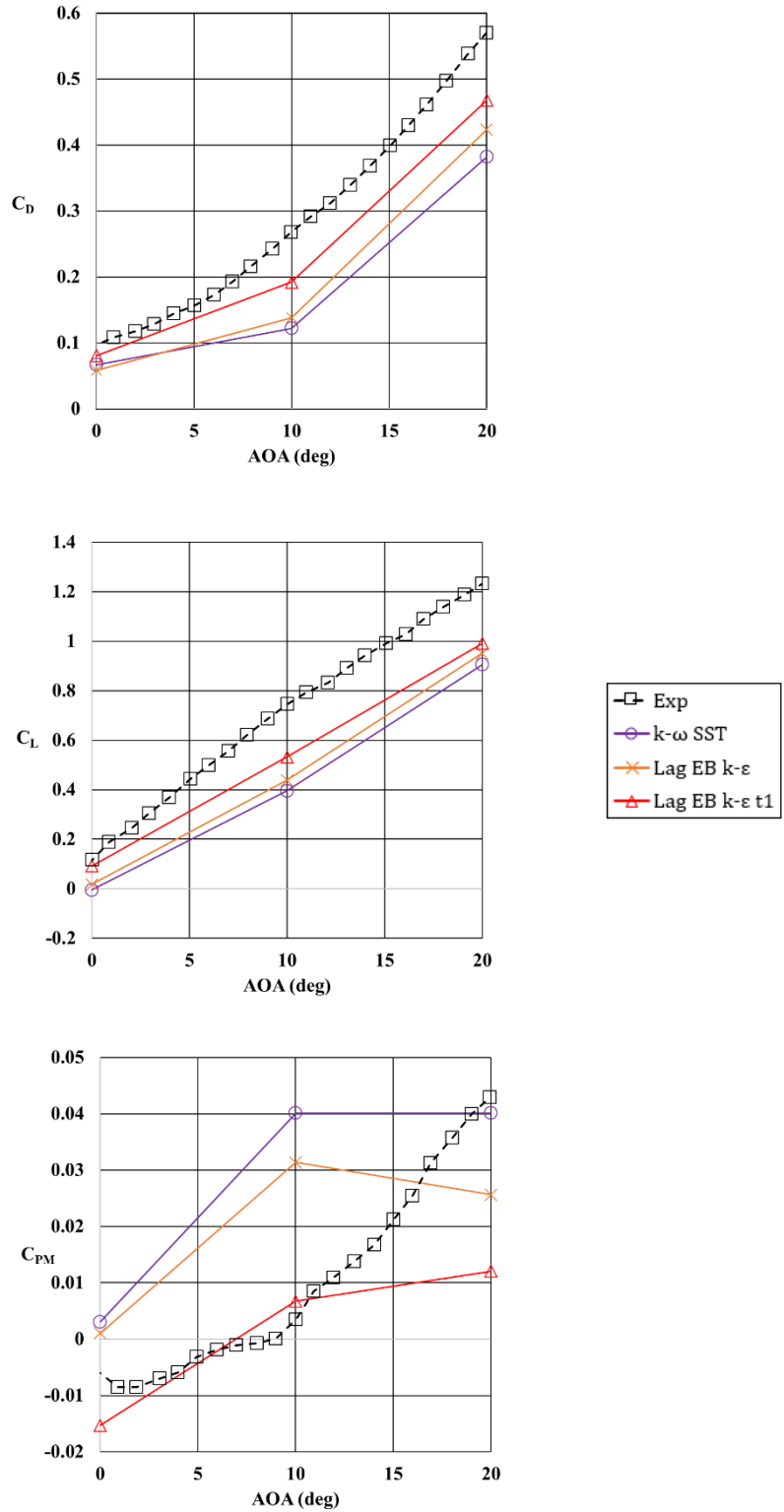


FIGURE 5.1. Aerodynamic force and moment coefficients for the Floater (calibration) disc for experimental, $k-\omega$ SST, Lag EB $k-\epsilon$, Lag EB $k-\epsilon$ tuned. C_D top, C_L center and C_{PM} bottom

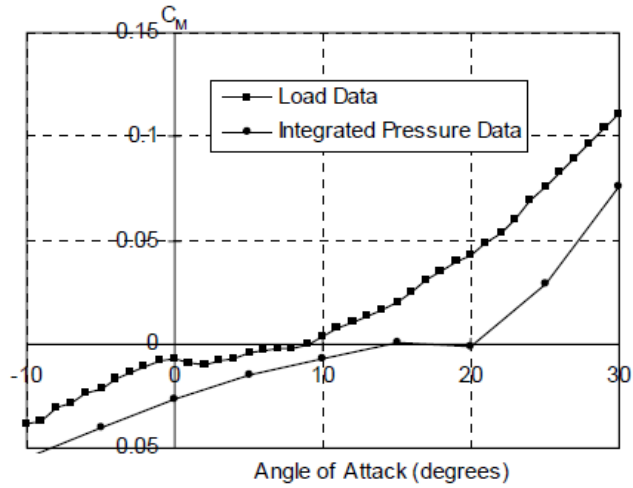


FIGURE 5.2. Experimental pitch moment coefficient data and pressure calculated pitch moment coefficients for the Floater (calibration) disc [2]

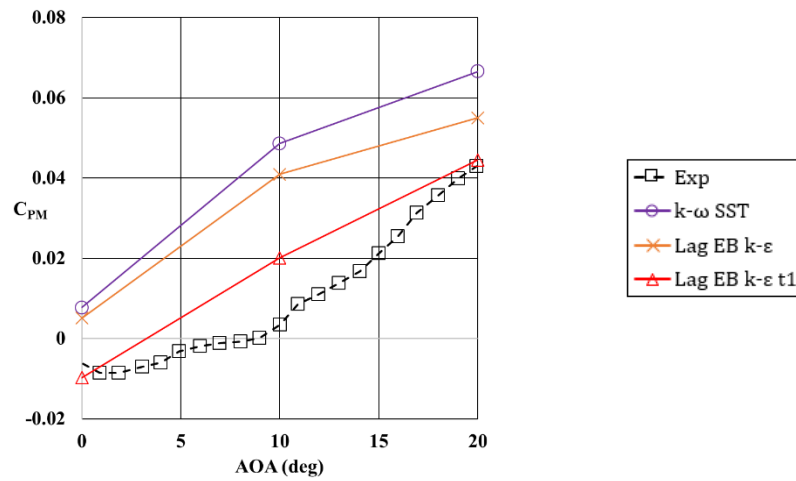


FIGURE 5.3. Recalculated CFD pitch moment using alternate pitch moment axis

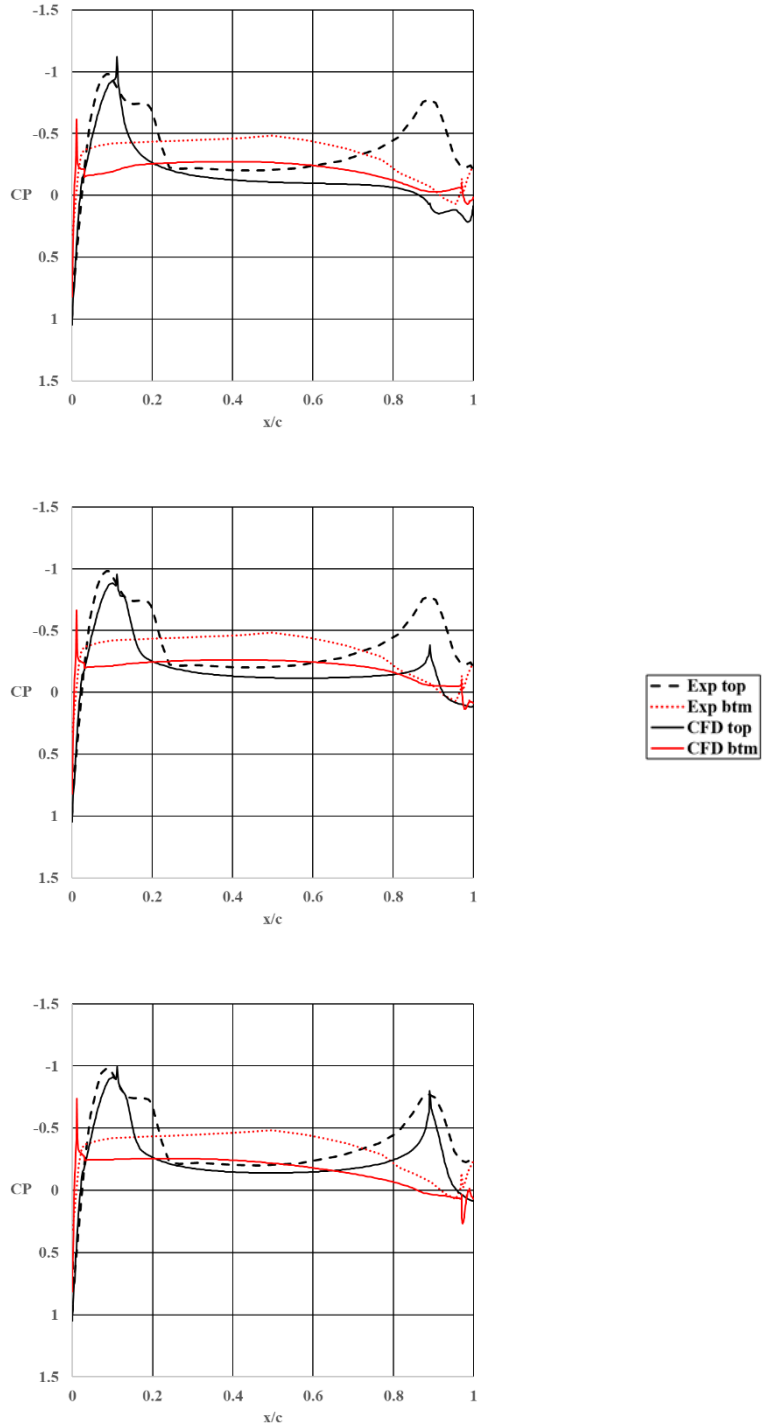


FIGURE 5.4. Centerline span pressure profiles for the Floater (calibration) disc. Experiment [2] and CFD. $k-\omega$ SST top, Lag EB $k-\epsilon$ center, Lag EB $k-\epsilon$ tuned bottom, $AoA=0^\circ$

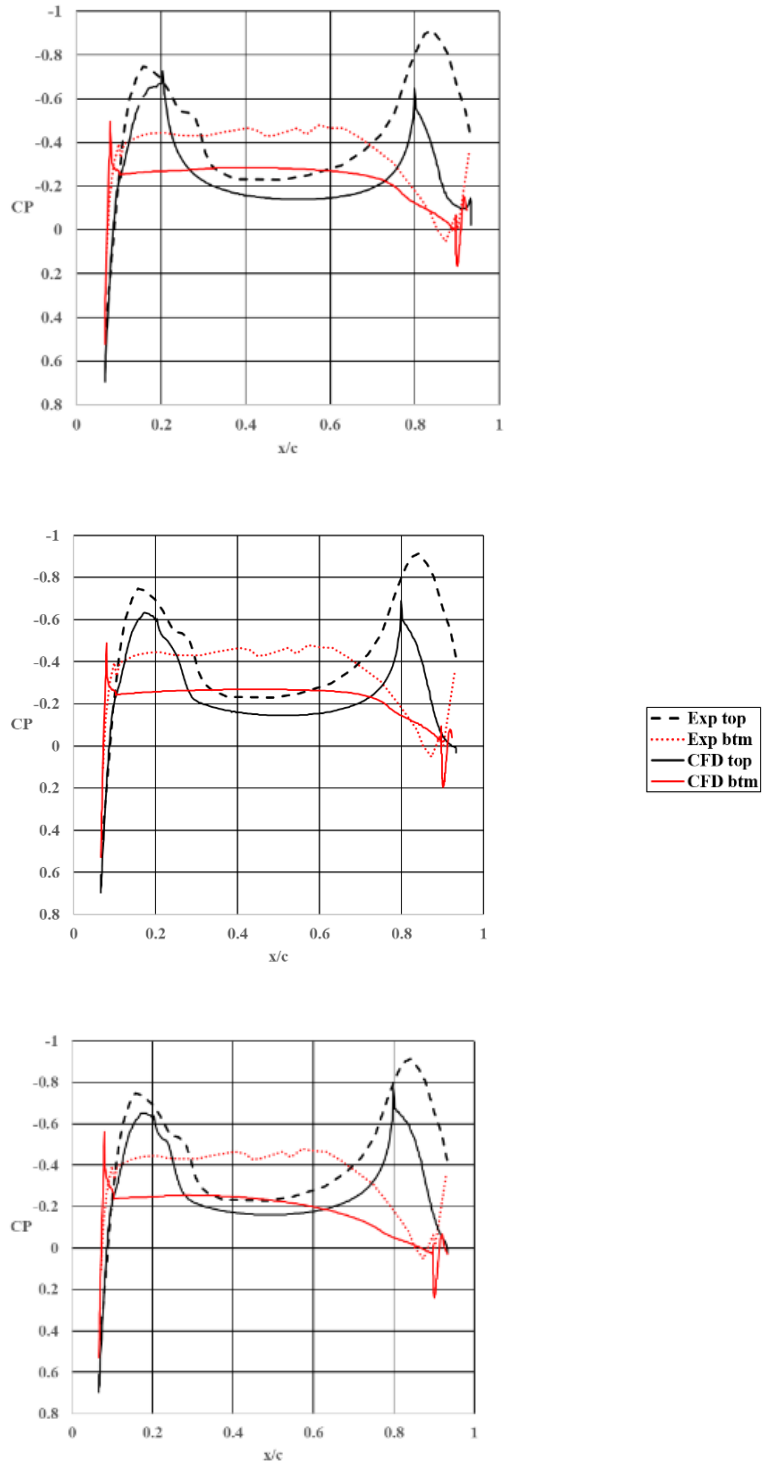


FIGURE 5.5. 1/4th Span pressure profiles for the Floater (calibration) disc. Experiment [2] and CFD. $k-\omega$ SST top, Lag EB $k-\varepsilon$ center, Lag EB $k-\varepsilon$ tuned bottom, $AoA=0^\circ$

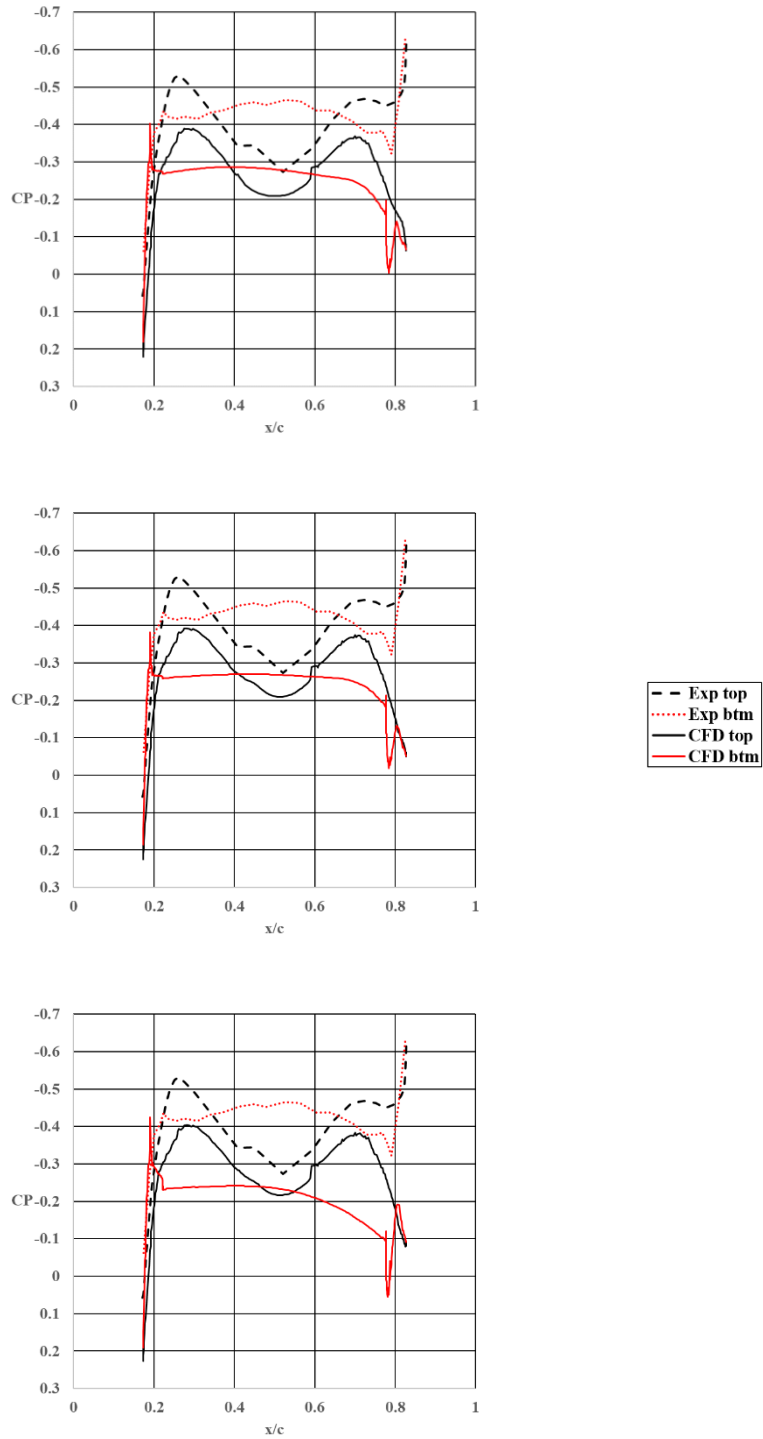


FIGURE 5.6. 1/8th Span pressure profiles for the Floater (calibration) disc. Experiment [2] and CFD. $k-\omega$ SST top, Lag EB $k-\varepsilon$ center, Lag EB $k-\varepsilon$ tuned bottom, $AoA=0^\circ$

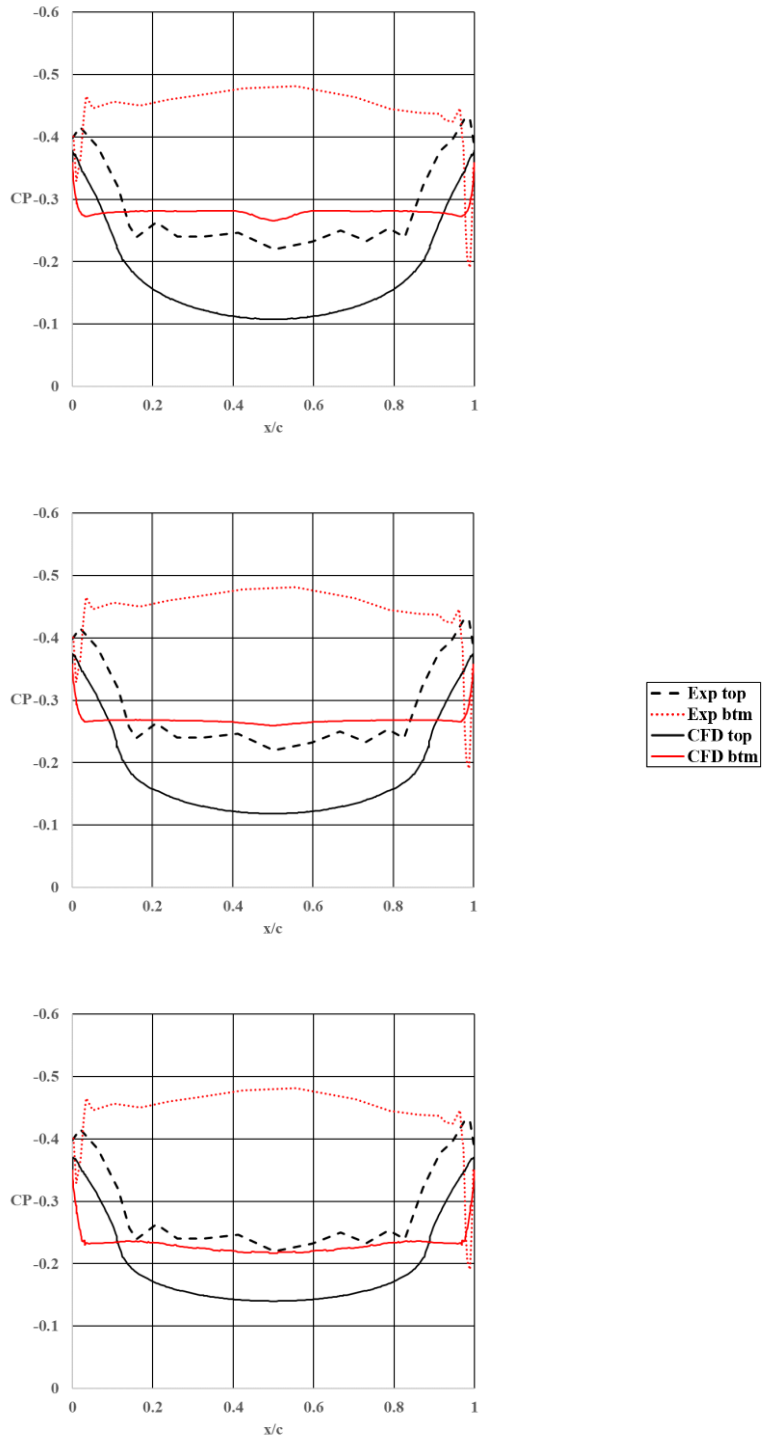


FIGURE 5.7. 1/2 Chord pressure profiles for the Floater (calibration) disc. Experiment [2] and CFD. $k-\omega$ SST top, Lag EB $k-\varepsilon$ center, Lag EB $k-\varepsilon$ tuned bottom, $\text{AoA}=0^\circ$

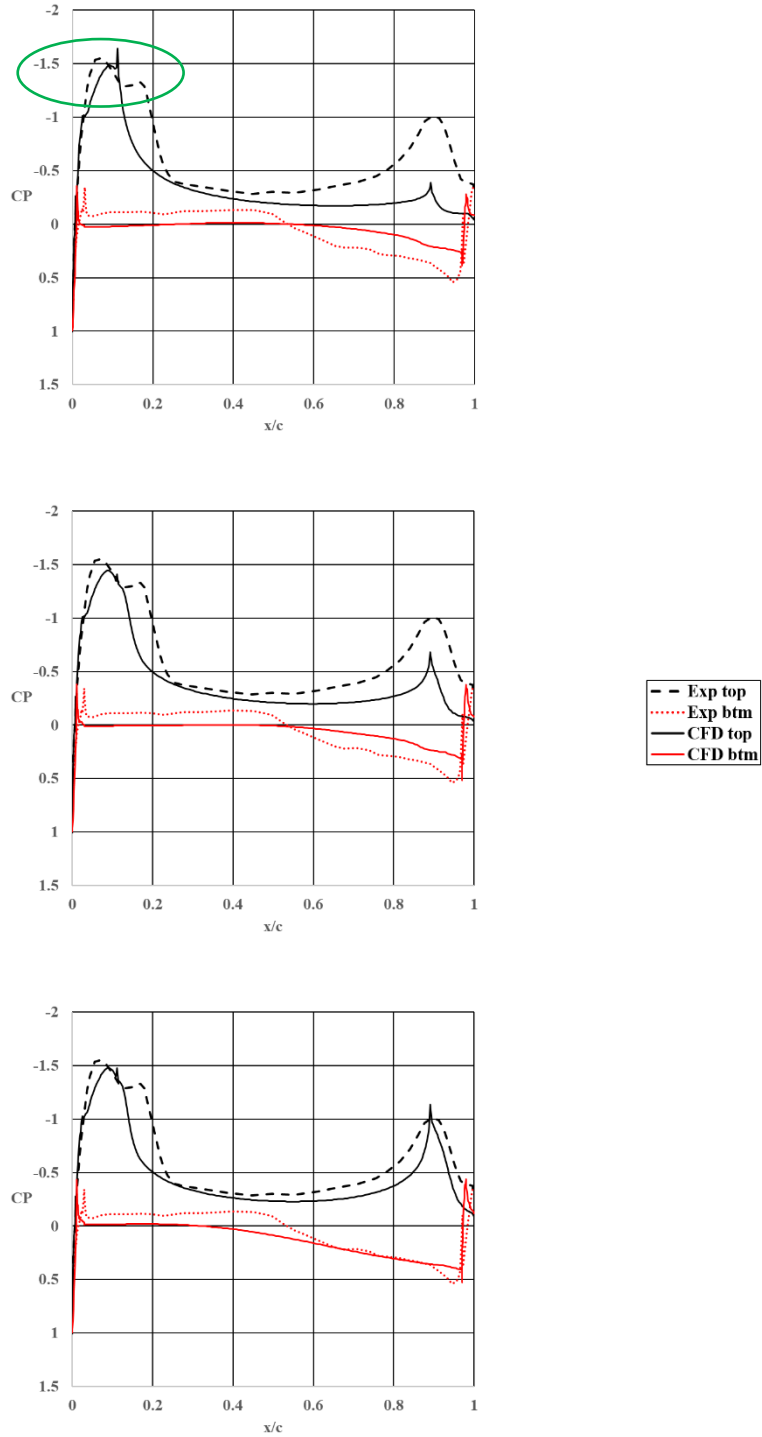


FIGURE 5.8. Centerline span pressure profiles for the Floater (calibration) disc. Experiment [2] and CFD. $k-\omega$ SST top, Lag EB $k-\varepsilon$ center, Lag EB $k-\varepsilon$ tuned bottom, $AoA=10^\circ$

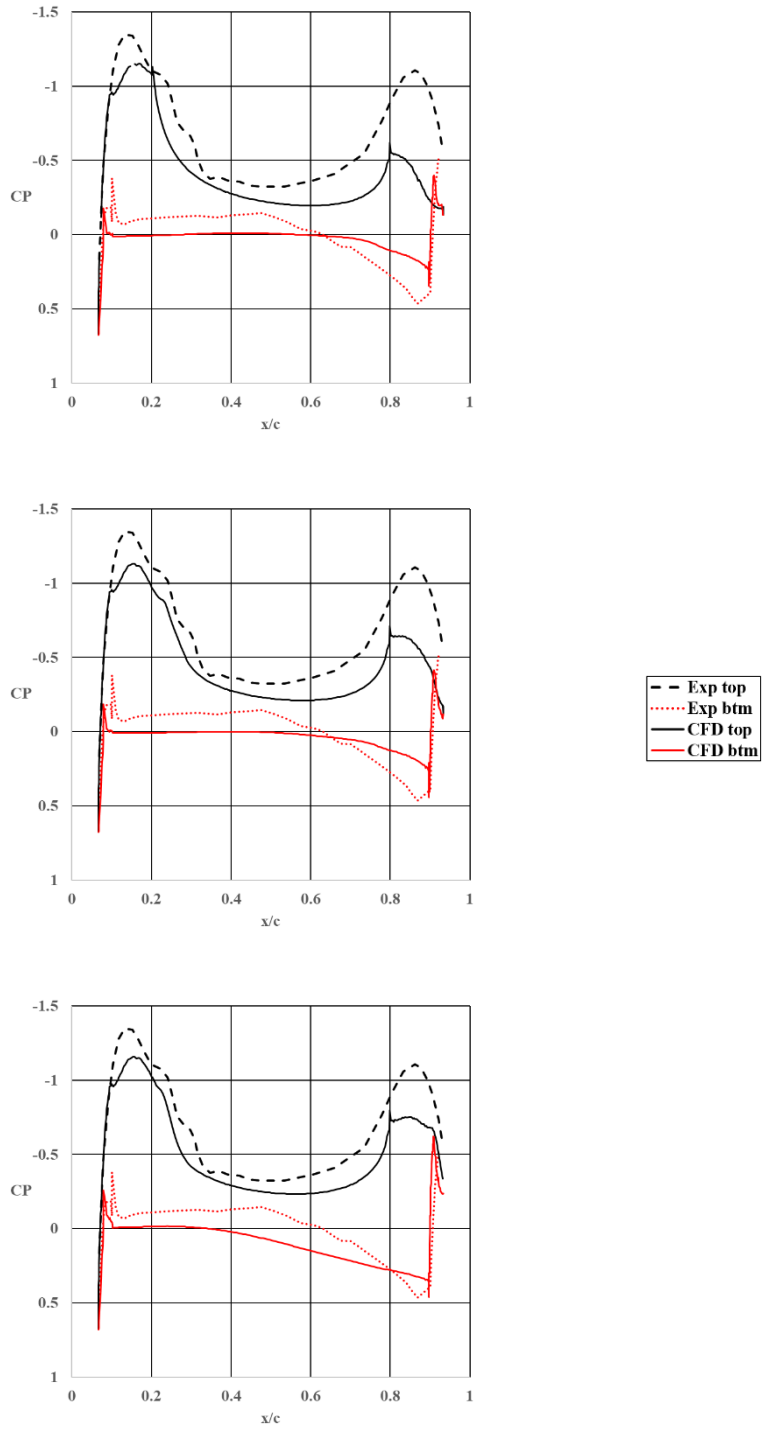


FIGURE 5.9. 1/4th Span pressure profiles for the Floater (calibration) disc. Experiment [2] and CFD. $k-\omega$ SST top, Lag EB $k-\epsilon$ center, Lag EB $k-\epsilon$ tuned bottom, $\text{AoA}=10^\circ$

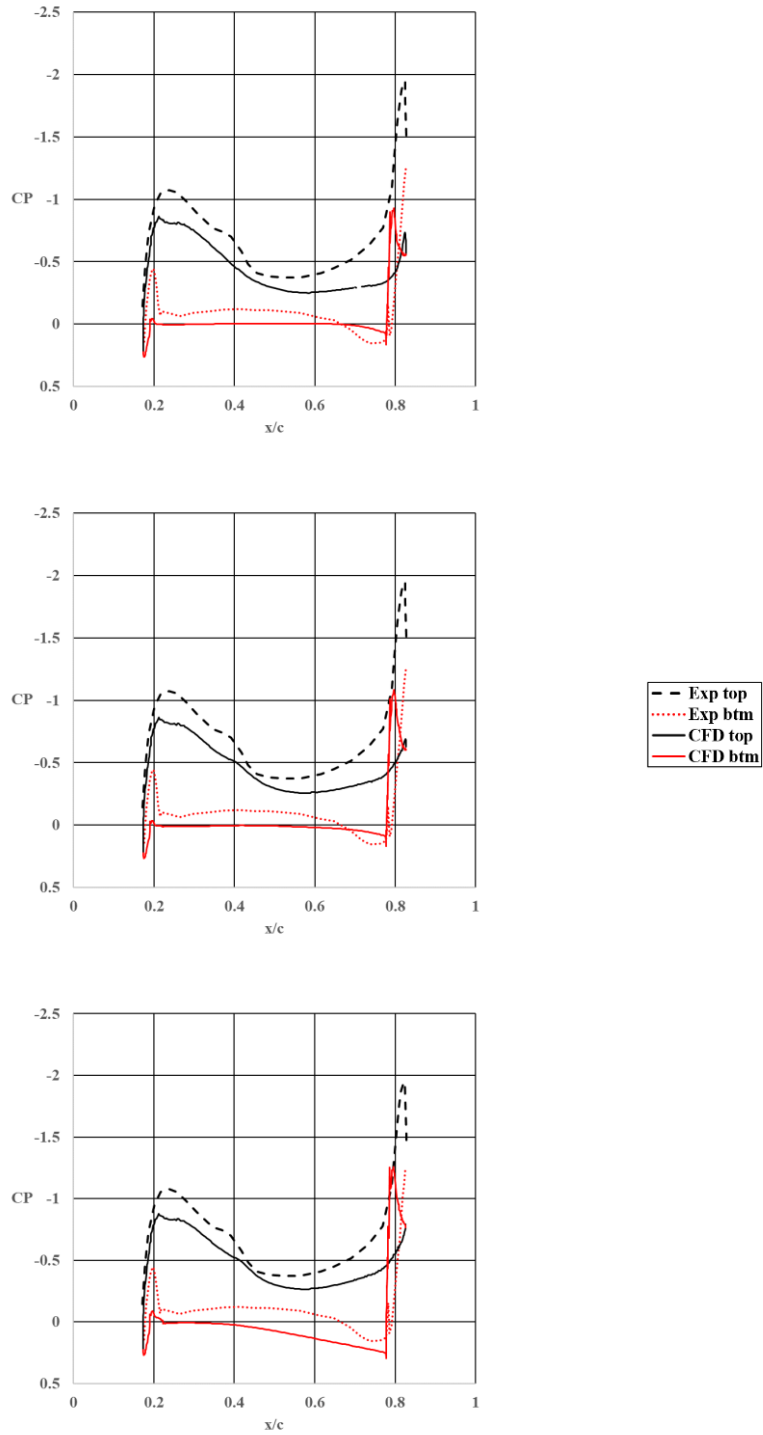


FIGURE 5.10. 1/8th Span pressure profiles for the Floater (calibration) disc. Experiment [2] and CFD. $k-\omega$ SST top, Lag EB $k-\varepsilon$ center, Lag EB $k-\varepsilon$ tuned bottom, $AoA=10^\circ$

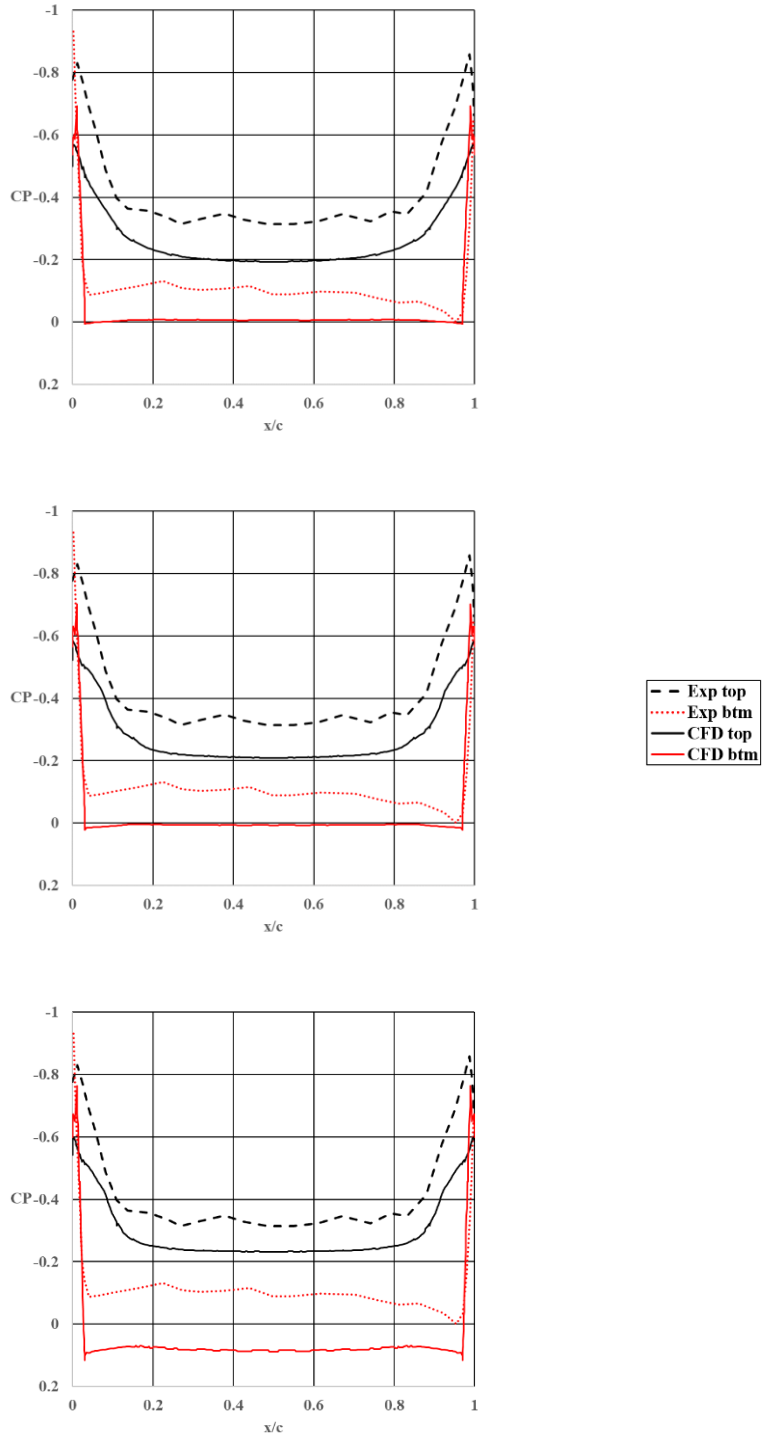


FIGURE 5.11. $\frac{1}{2}$ Chord pressure profiles for the Floater (calibration) disc. Experiment [2] and CFD. $k-\omega$ SST top, Lag EB $k-\varepsilon$ center, Lag EB $k-\varepsilon$ tuned bottom, $AoA=10^\circ$

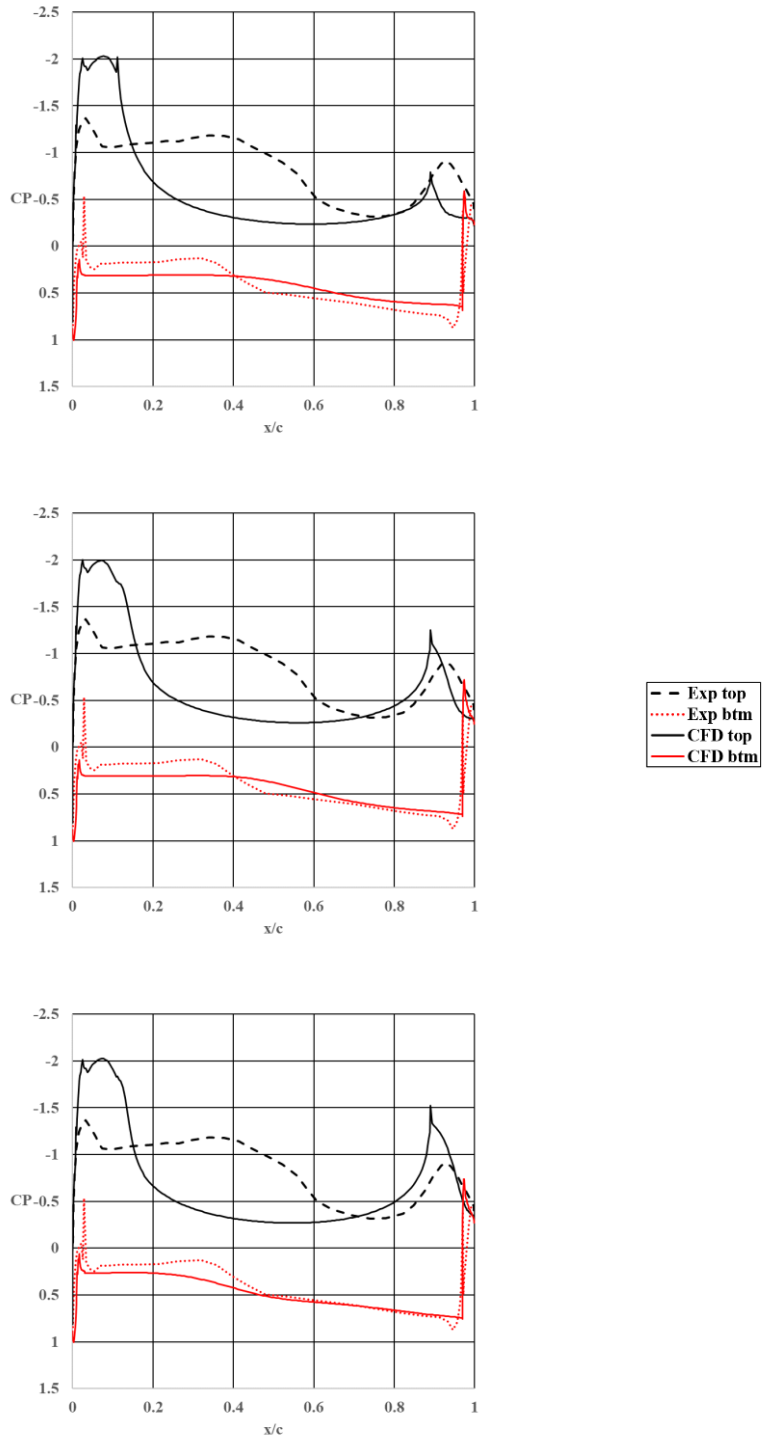


FIGURE 5.12. Centerline span pressure profiles for the Floater (calibration) disc. Experiment [2] and CFD. $k-\omega$ SST top, Lag EB $k-\varepsilon$ center, Lag EB $k-\varepsilon$ tuned bottom, $AoA=20^\circ$

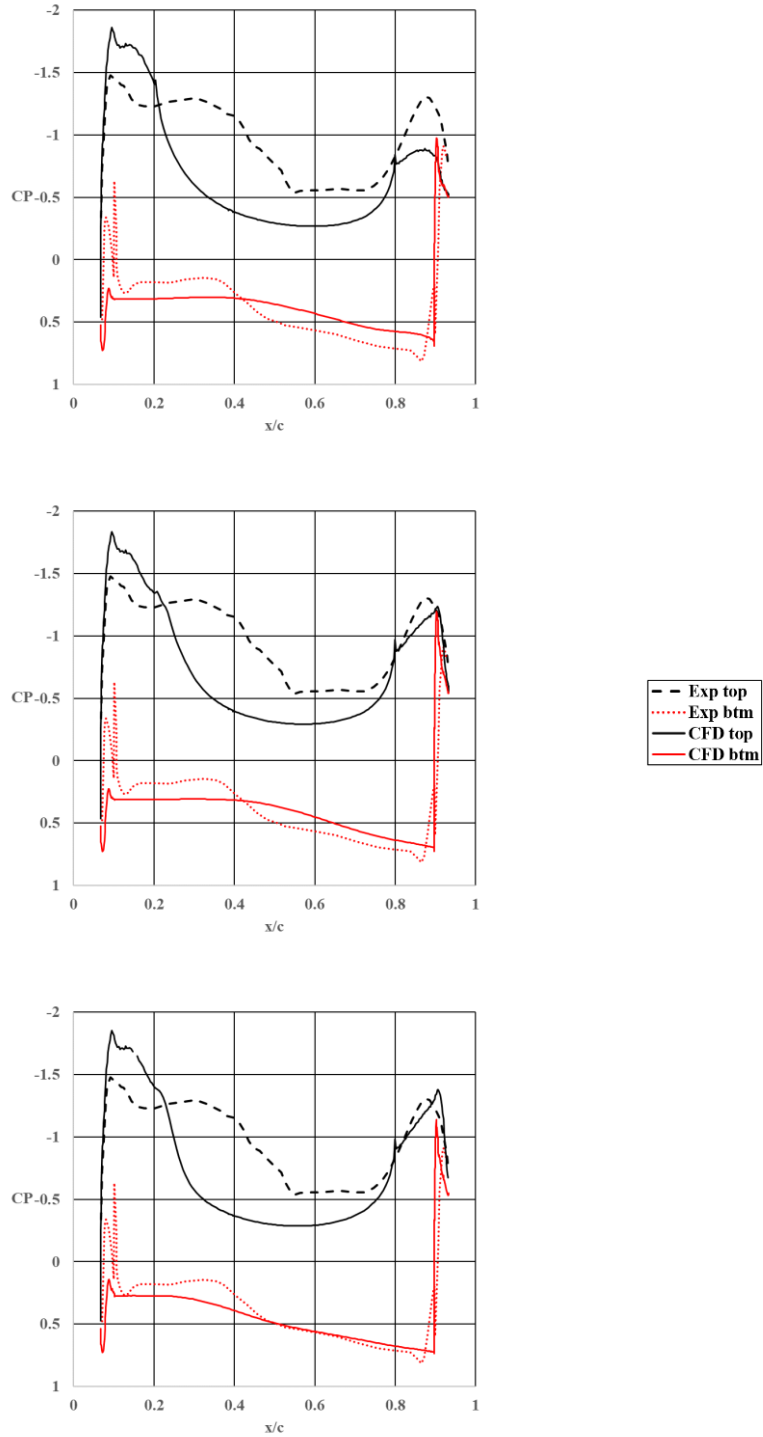


FIGURE 5.13. 1/4th Span pressure profiles for the Floater (calibration) disc. Experiment [2] and CFD. $k-\omega$ SST top, Lag EB $k-\varepsilon$ center, Lag EB $k-\varepsilon$ tuned bottom, $AoA=20^\circ$

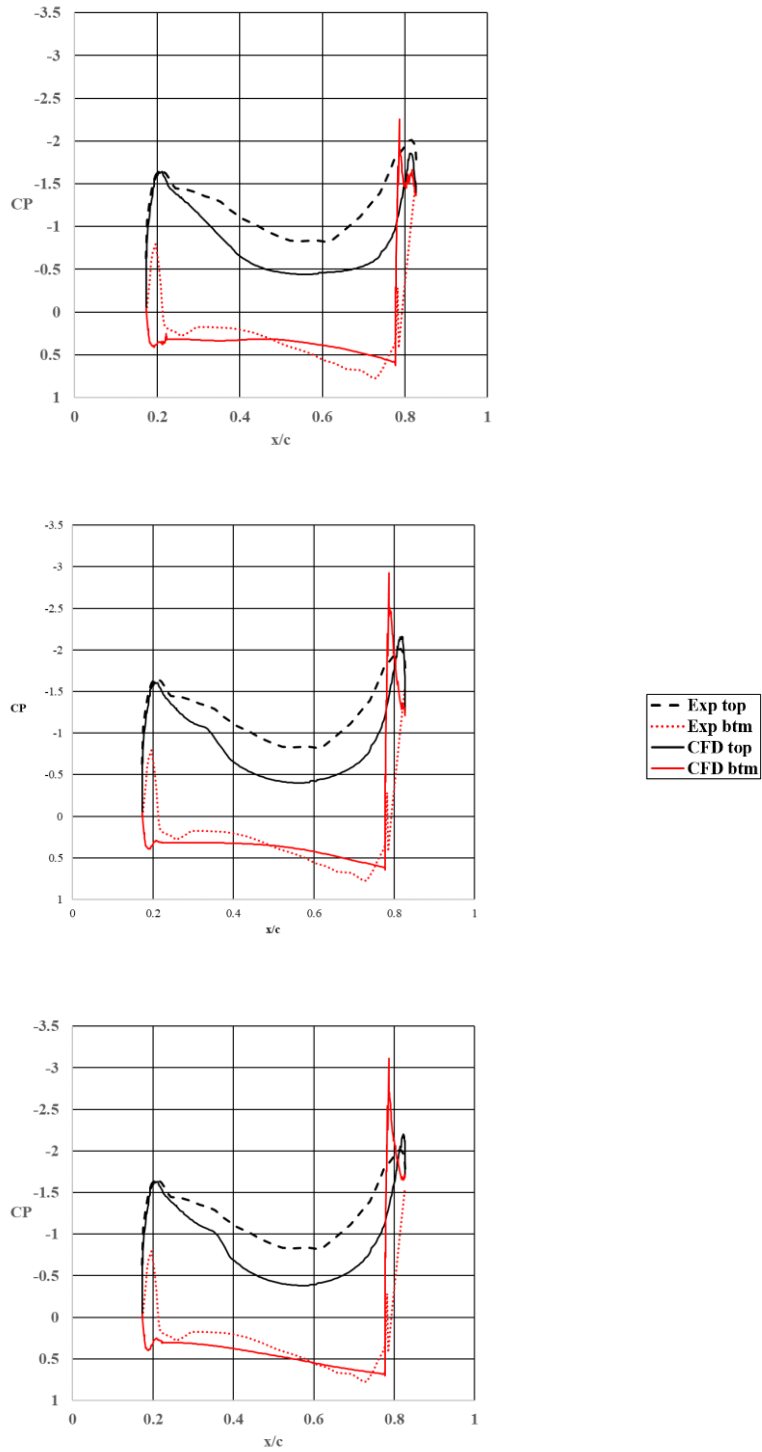


FIGURE 5.14. 1/8th Span pressure profiles for the Floater (calibration) disc. Experiment [2] and CFD. $k-\omega$ SST top, Lag EB $k-\varepsilon$ center, Lag EB $k-\varepsilon$ tuned bottom, $AoA=20^\circ$

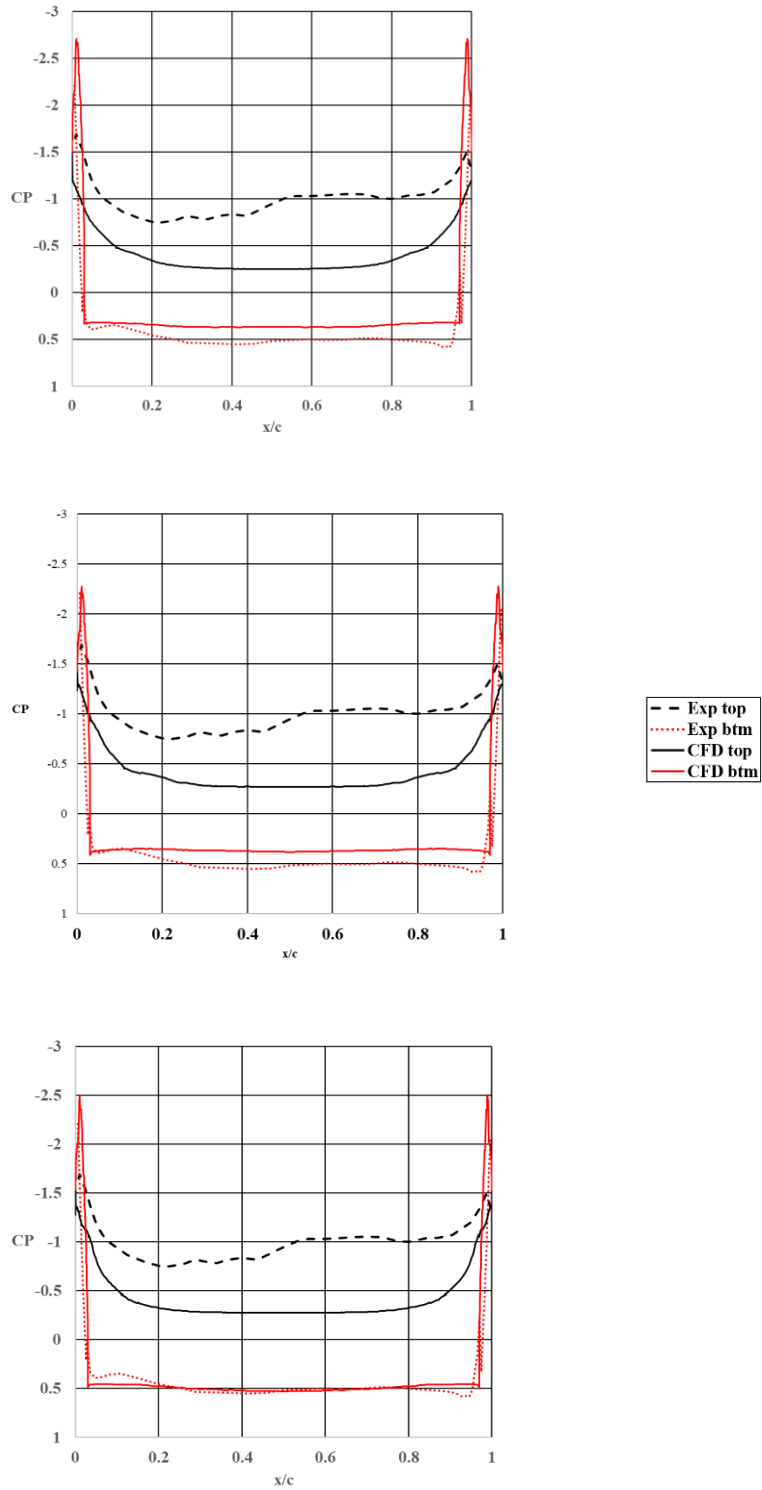


FIGURE 5.15 $\frac{1}{2}$ Chord pressure profiles for the Floater (calibration) disc. Experiment [2] and CFD. $k-\omega$ SST top, Lag EB $k-\varepsilon$ center, Lag EB $k-\varepsilon$ tuned bottom, $AoA=20^\circ$

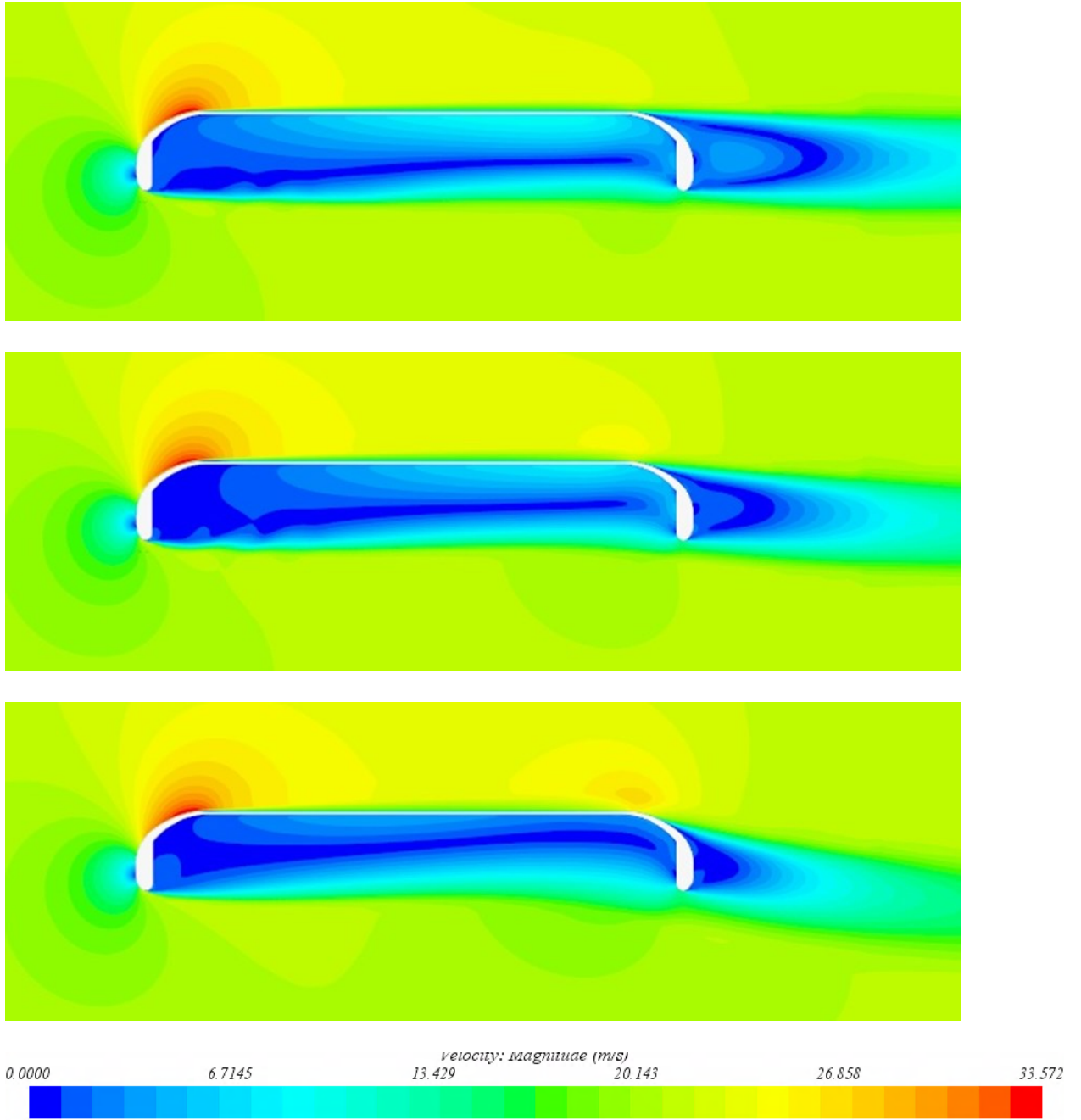


FIGURE 5.16. CFD centerline span velocity magnitude plots for the Floater (calibration) disc. $k-\omega$ SST top, Lag EB $k-\epsilon$ center, Lag EB $k-\epsilon$ tuned bottom, $AoA=10^\circ$

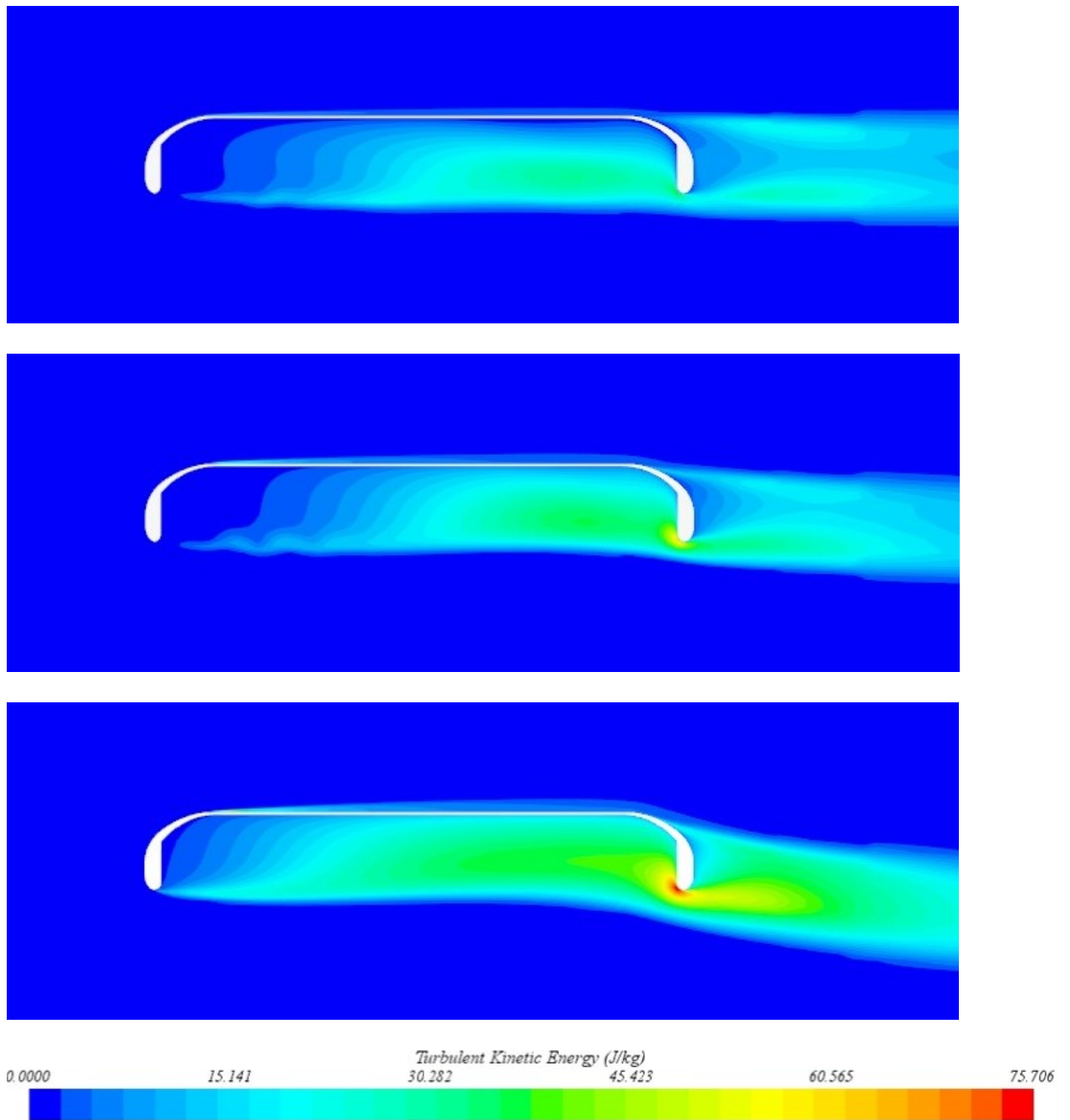


FIGURE 5.17. CFD centerline span turbulent kinetic energy plots for the Floater (calibration) disc. $k-\omega$ SST top, Lag EB $k-\epsilon$ center, Lag EB $k-\epsilon$ tuned bottom, $AoA=10^\circ$

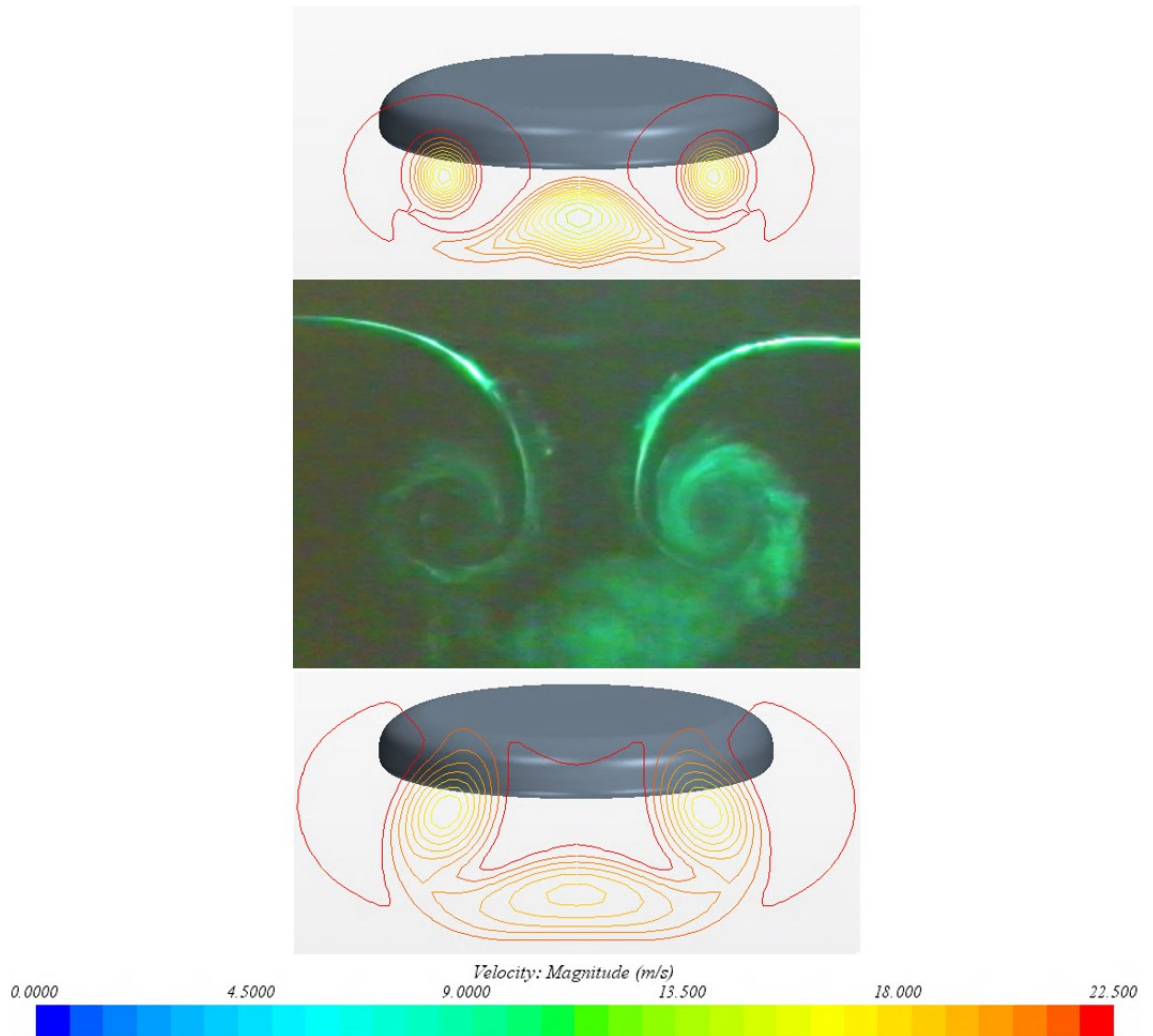


FIGURE 5.18. Comparison of trailing vortices. $k-\omega$ SST top, experiment center, Lag EB $k-\epsilon$ tuned bottom, one diameter aft of disc trailing edge. $AoA=10^\circ$. Reynolds number for experiment was 56,700 [2].

5.3 Commercial golf discs

The only quantitative data available for the commercial golf discs were C_D , C_L , and C_{PM} . The maximum angle of attack tested was 15 degrees [12]. The CFD force and moment coefficient curve shapes match the experimental curve shapes very well as shown in FIGURE 5.19 through FIGURE 5.21 although there are magnitude differences that will be explored further. C_D and C_L are likely within repeatability of the reverse engineering and experimental methods used. C_{PM} shows the most deviation from experiment but this is to be expected since small force changes at the extents of the disc can swing the pitch moment by large amounts. It is also worth noting that large differences in aerodynamic coefficients have been observed when testing the same model in different wind tunnels. All of the author's experiences relate to automotive models. But surely all differences cannot be simply attributed to this type of variation. Unless the disc experimental setup was not sufficiently replicated in CFD (geometry including pressure hose routing) it is likely that the turbulence models still need improvements to accurately predict all aerodynamic characteristics as evidenced by the difference in magnitude and shape for the pressure profiles for the Floater calibration disc. But recall, the blunt Floater calibration disc was viewed as an extremely challenging case for the turbulence models.

A natural question to ask is how does each of the individual discs' aerodynamic force and moment coefficients rank compared to each other for experiment and CFD? For instance, if discs are ranked from lowest to highest C_D for both experiment and CFD, do the rankings agree? FIGURE 5.22 through FIGURE 5.24 provide a visual means to address this question. Experimental data for each disc is plotted in the top portion of each figure and CFD data is plotted in the bottom. For the C_D plot, experiment and CFD are

very close at 0 and 15 degrees for all discs but differ more at 10 degrees. In fact, CFD predicts the ranking of C_D incorrectly at 10 degrees since the Quarter K and Wraith points have switched places from experiment to CFD. CFD matches experiment for the ranking of C_L for all discs at all three points of comparison. The Wraith has the most lift at all three points and the Flick has the least lift at all three points. For the C_{PM} plots the Flick had the most pitch moment for both experiment and CFD, but the Quarter K and the Wraith switched places in the rankings for all three points. Overall, the drag and lift rankings are likely as accurate as can be expected given the error potentially created by the reverse engineering methods used to create the CFD surfaces. Additional error was created when the force and moment coefficient plots were scanned from image files. C_{PM} results could likely be improved further with additional turbulence model calibration although it is not surprising that CFD is least accurate for pitch moment compared to drag and lift. Small variations in force at the extremes of the disc can generate large changes in pitch moment due to the length of the moment arm in the formulation of pitch moment.

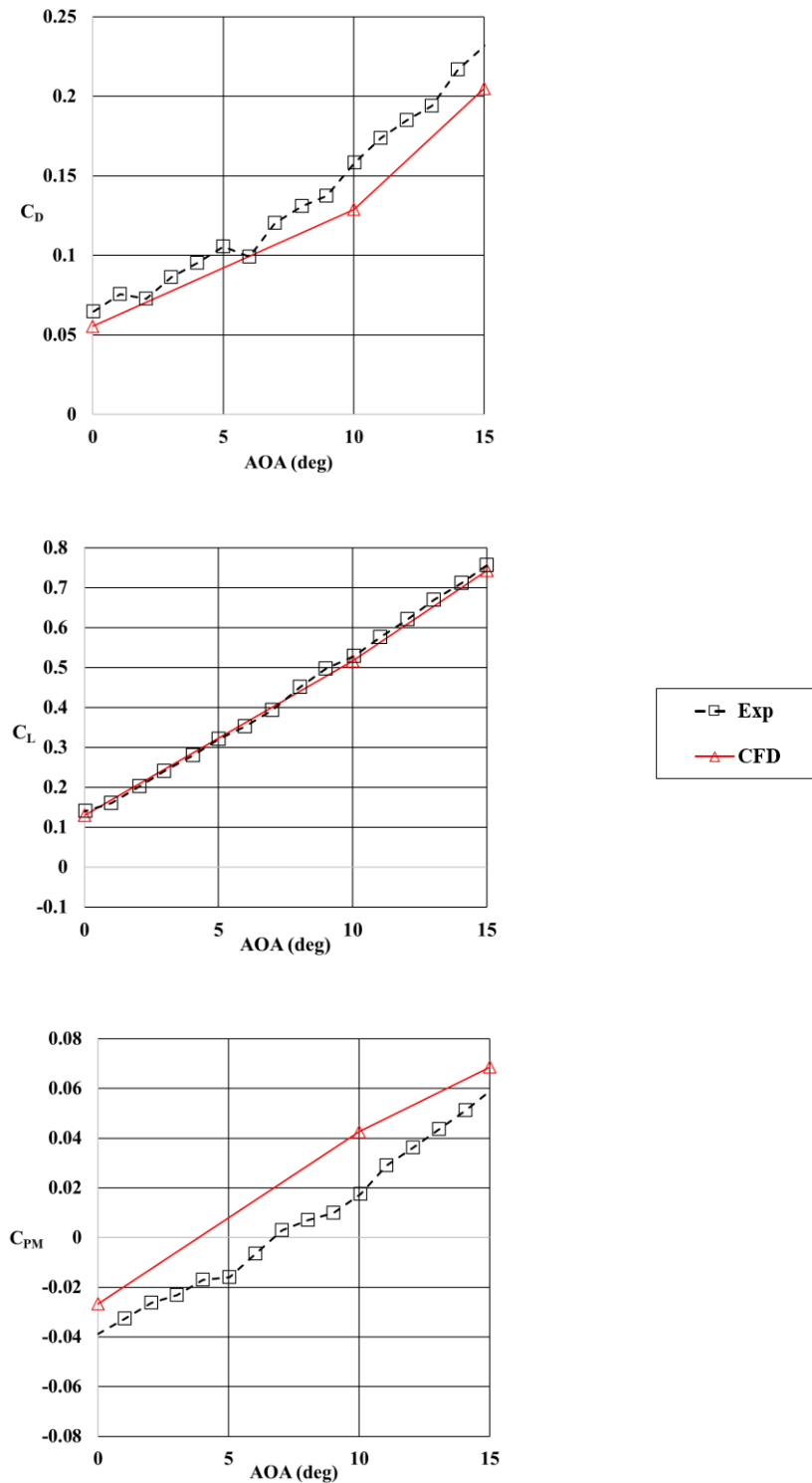


FIGURE 5.19. Aerodynamic force and moment coefficients for the Quarter K golf disc, Lag EB $k-\varepsilon$ tuned turbulence model and experiment [12]. C_D top, C_L center and C_{PM} bottom

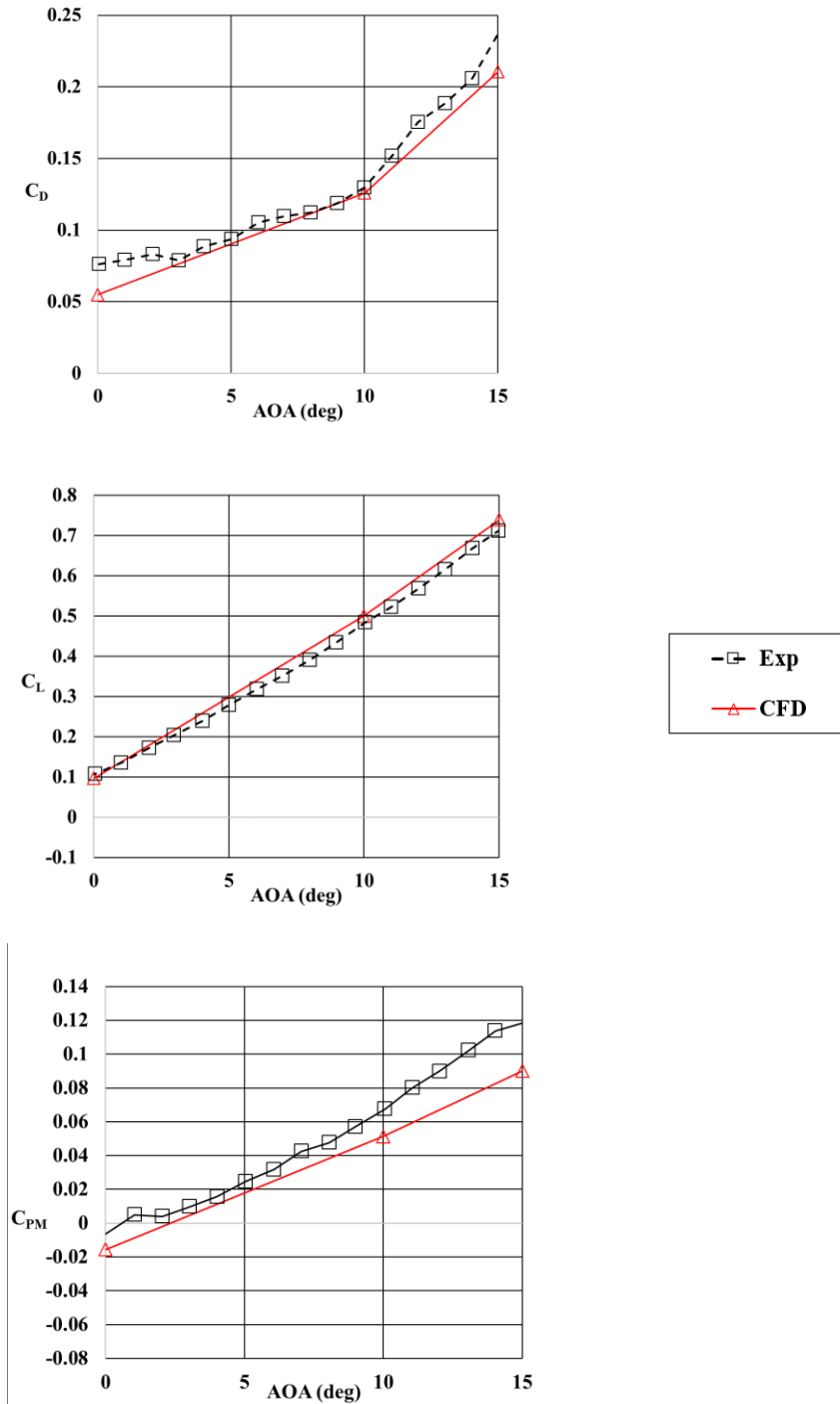


FIGURE 5.20. Aerodynamic force and moment coefficients for the Flick golf disc, Lag EB $k-\epsilon$ tuned turbulence model and experiment [12]. C_D top, C_L center and C_{PM} bottom

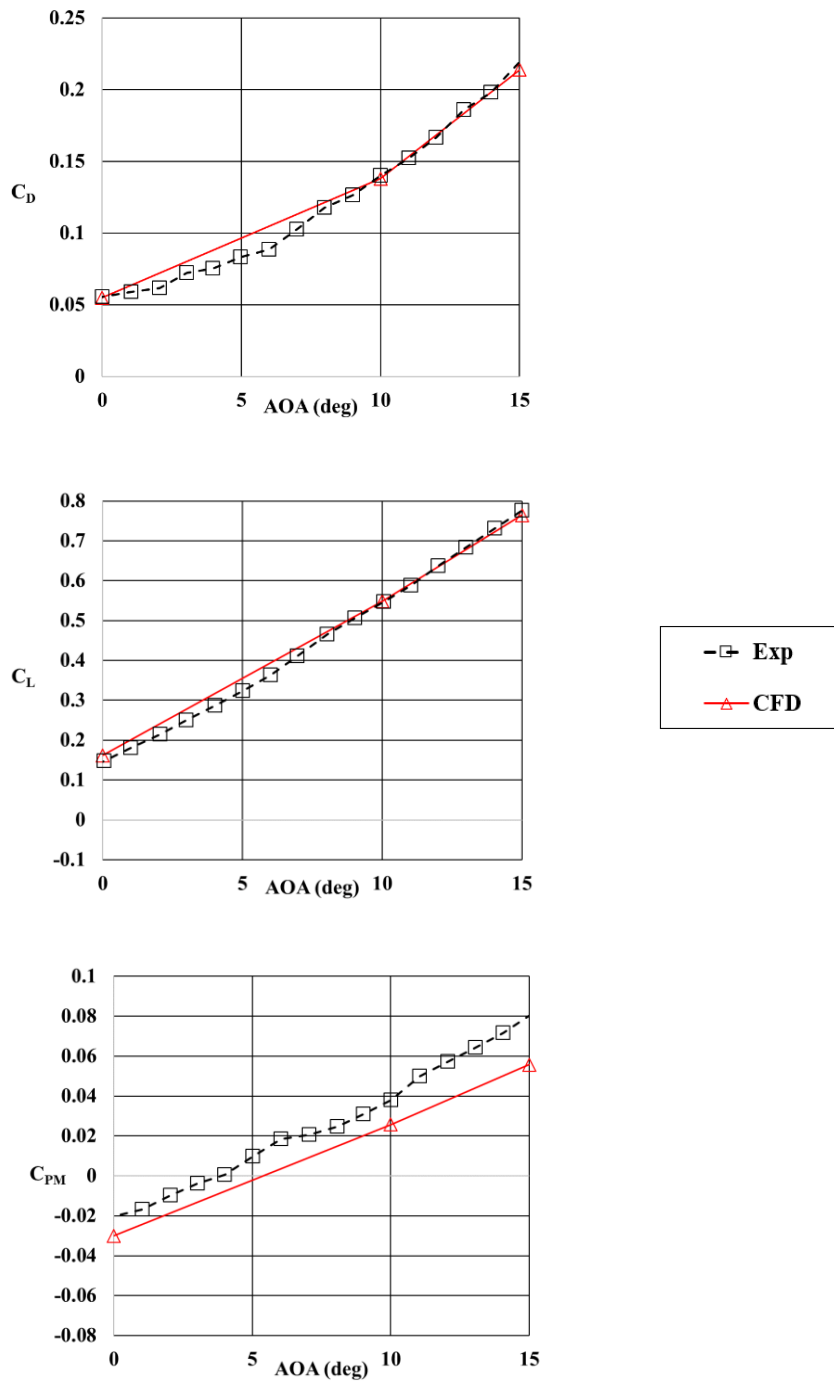


FIGURE 5.21. Aerodynamic force and moment coefficients for the Wraith golf disc, Lag EB k - ϵ tuned turbulence model and experiment [12]. C_D top, C_L center and C_{PM} bottom

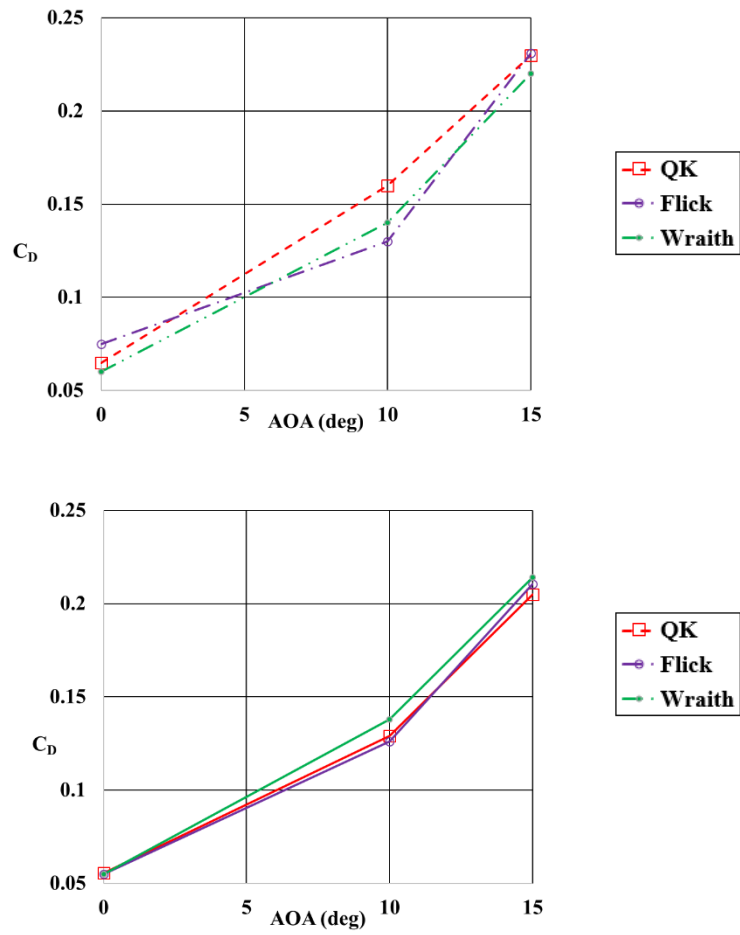


FIGURE 5.22. C_D v. AoA for all existing discs: experiment top [12], CFD bottom

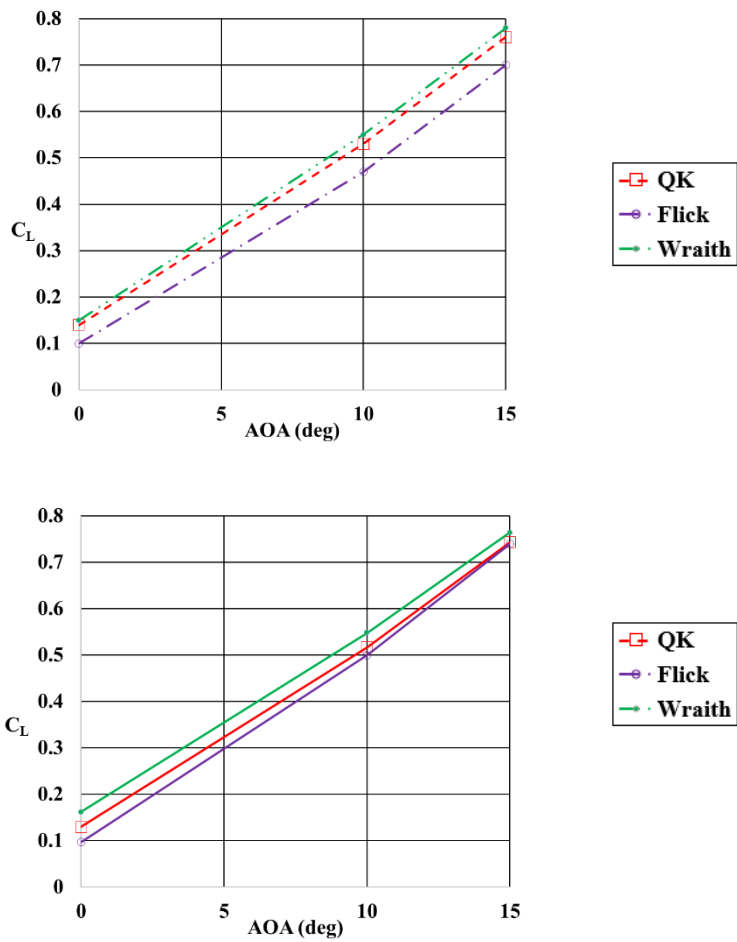


FIGURE 5.23. C_L v. AoA for all existing discs: experiment top [12], CFD bottom

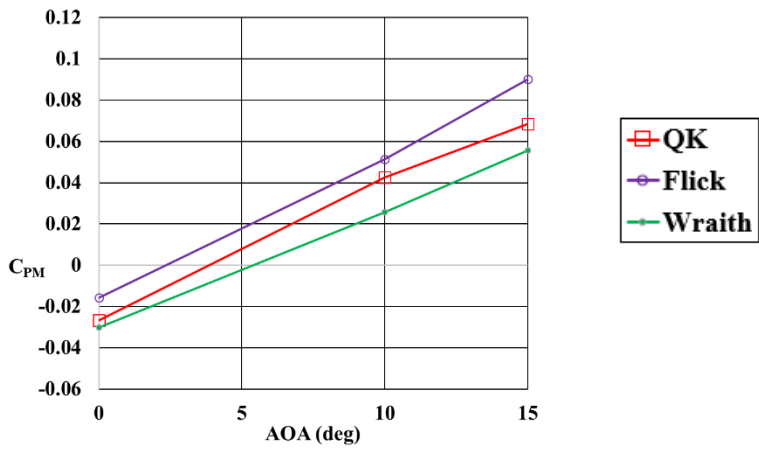
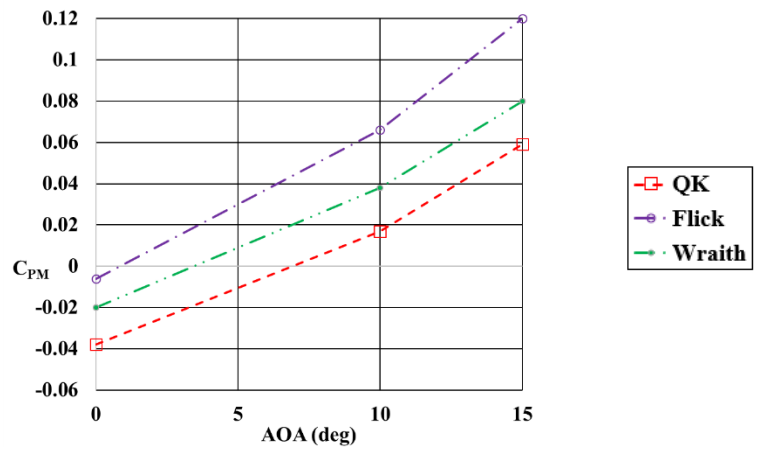


FIGURE 5.24. C_{PM} v. AoA for all existing discs: experiment top [12], CFD bottom

5.4 New disc designs

FIGURE 5.25 presents the aerodynamic force and moment coefficient results for all the new disc designs along with the Wraith disc. Although quantitative data is produced from the CFD, only cursory qualitative comments about the flight behavior can be made without further analysis. A flight simulation algorithm that takes the aerodynamic and non-aerodynamic forces into account, very importantly the gyroscopic effects, must be performed to predict the flight path.

The Wraith disc and Disc 1 curves approximately coincide for most data points as the circular protrusion had a minimal affect. The hypotheses put forth to support the design changes for Disc 2 compared to the Wraith seem to have been valid. More lift was created at 0 degrees angle of attack but this came at a cost as the drag increased. Surprisingly, the pitch moment decreased at 0 degrees angle of attack. FIGURE 5.26 is a plot of velocity magnitude at centerline for an angle of attack of 10 degrees with the Wraith disc on the top and Disc 2 on the bottom. More high energy flow is directed downwards thereby creating more lift for Disc 2. Also, notice the increased velocity on the center top surface of Disc 2 due to the circular protrusion originally added to Disc 1 and retained for Disc 2. This feature could possibly be accentuated in a future design resulting in more lift. Disc 3, with the outer lip that resembles the Aerobie has much more drag than the other disc designs. Again, flow visualization needs to be conducted to advance this and all designs. At first look, the concepts from Disc 2 show some promise but Disc 1 and Disc 3 need some major study and redesign which is outside of the scope of this thesis and could be the topic of future research.

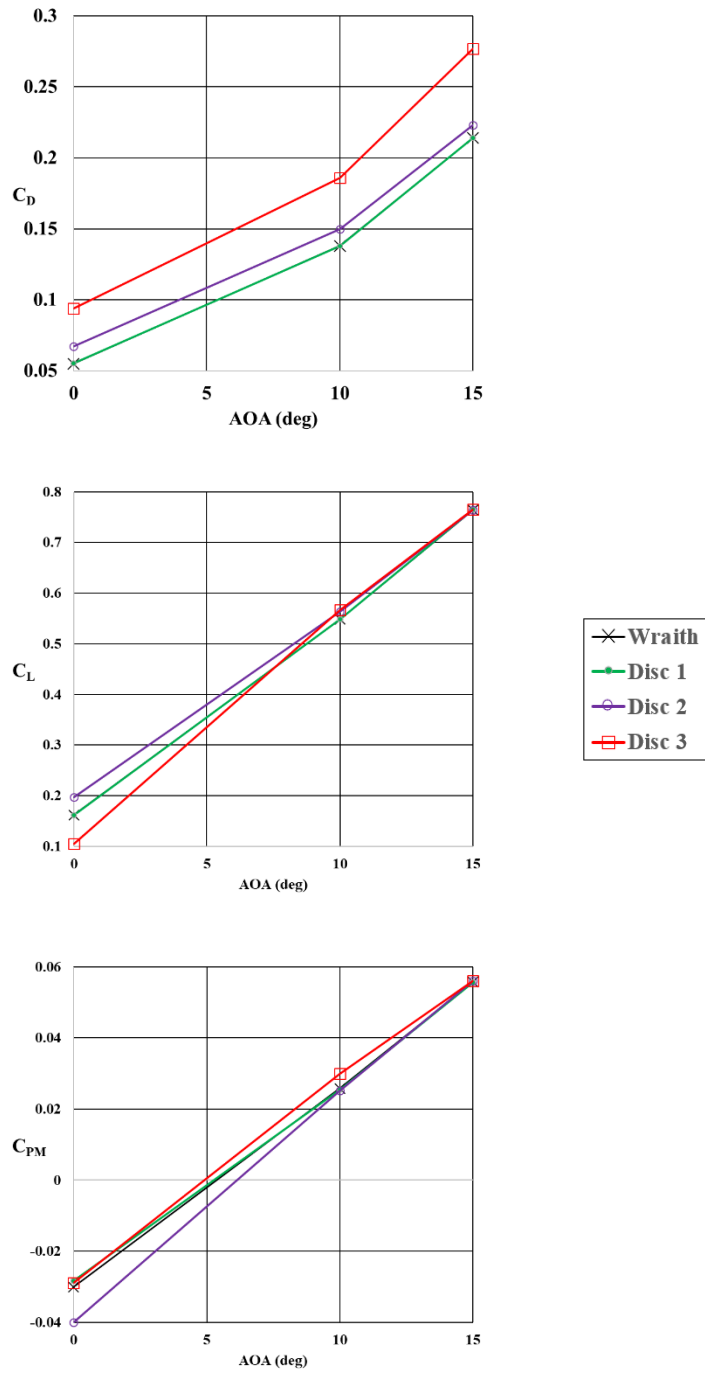


FIGURE 5.25. Aerodynamic force and moment coefficients (CFD) for three new disc designs and the Wraith disc

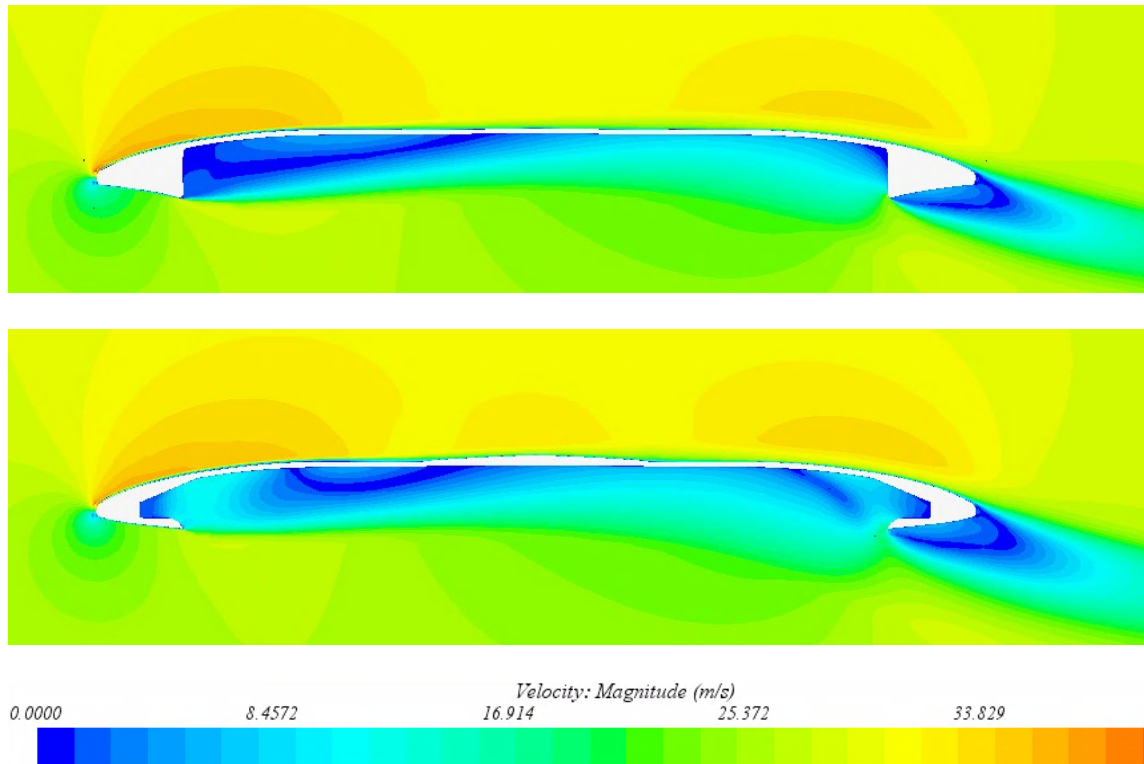


FIGURE 5.26. Velocity magnitude. Wraith top, Disc 2 bottom. $AoA=10^\circ$.

5.5 Additional angles of attack runs

The force and moment coefficient results are included in FIGURE 5.27 for the additional angles of attack runs suggested by one of the reviewers of this paper. The Lag EB $k-\epsilon$ tuned turbulence model was used in RANS mode for the Floater calibration disc and the three commercial golf discs. For the Floater calibration disc, the angles of -10, -5, and 5 degrees were added. For the commercial golf discs, -5 and 5 degrees were added. For the Floater calibration disc, -5 and 5 degree angle data align very well with the existing CFD trend. The offset from the experimental data for these two new points is very similar to offset for the other CFD data for the Floater calibration disc. The -10 degree angle data diverges more than expected for C_D and C_L , but the shape of the CPM plot is consistent

with the shape of the experimental curve. The data for the 5 degree angle added for all commercial golf discs matches the trend of the existing data as compared to the experimental data very well. The -5 degree matches the trend of the previous CFD data well for lift and pitch moment, but the drag deviates more for all discs than was expected, especially since the drag at -5 degrees for the blunt shaped Floater calibration disc matched so well. In summary, the additional points matched reasonably well for positive angles of attack, but not as well for negative angles. Since the turbulence model was primarily calibrated for positive angles of attack this is not surprising.

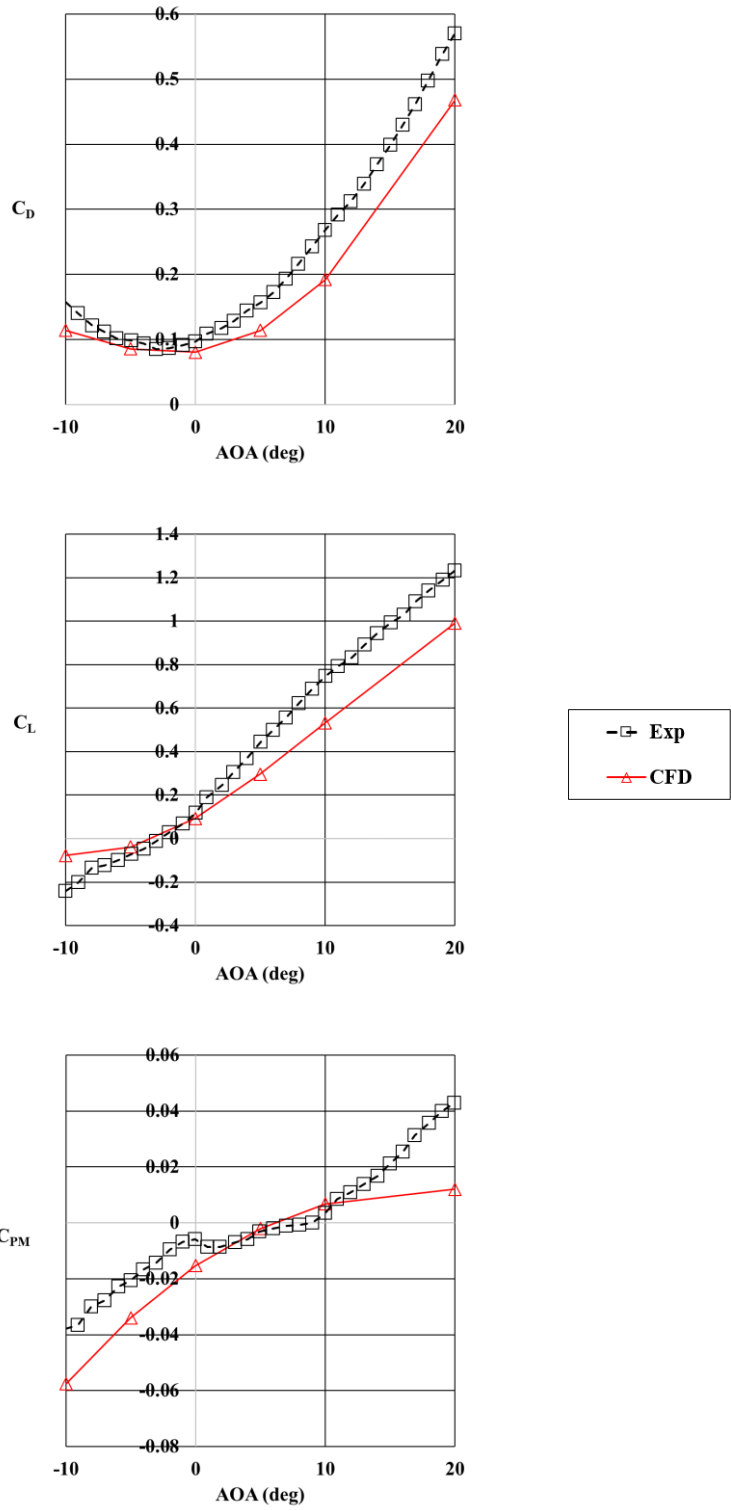


FIGURE 5.27. Aerodynamic force and moment coefficient results with additional angles of attack for Floater calibration disc

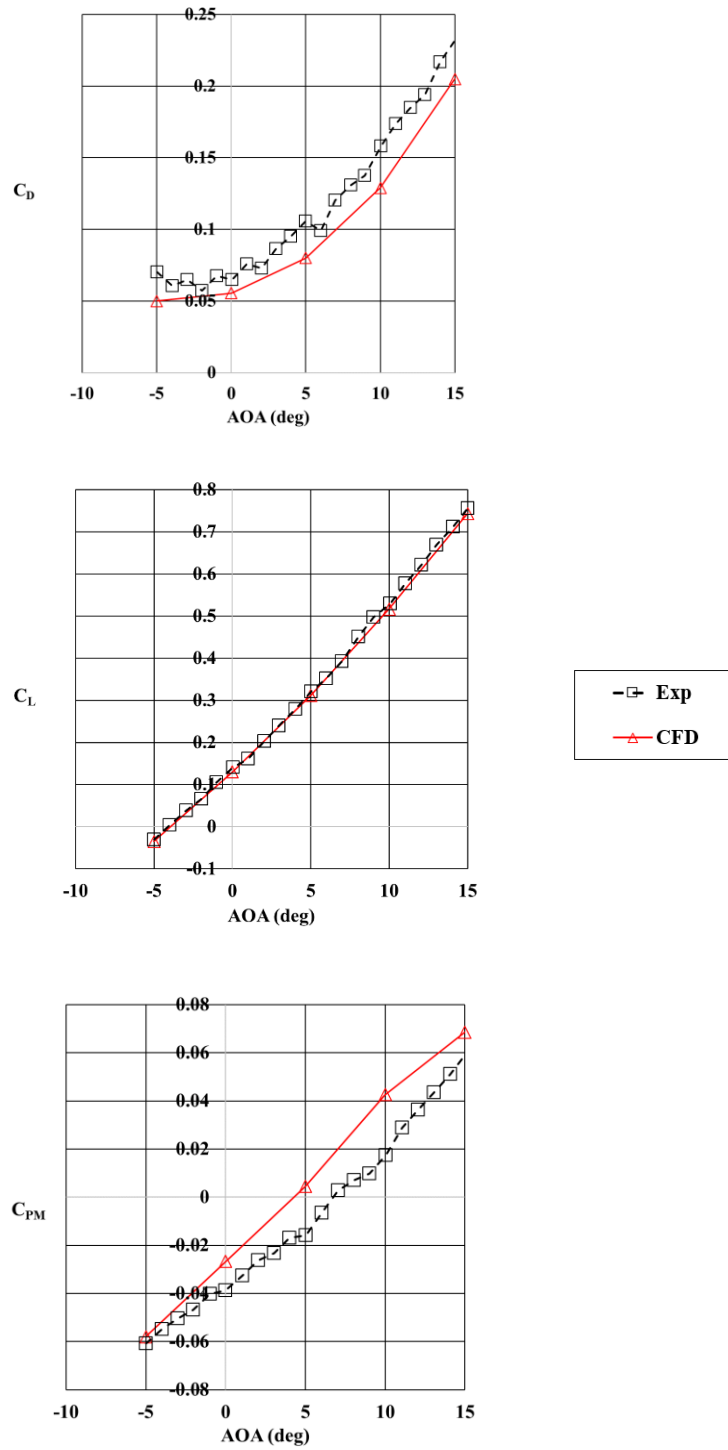


FIGURE 5.28. Aerodynamic force and moment coefficient results with additional angles of attack for Quarter K disc

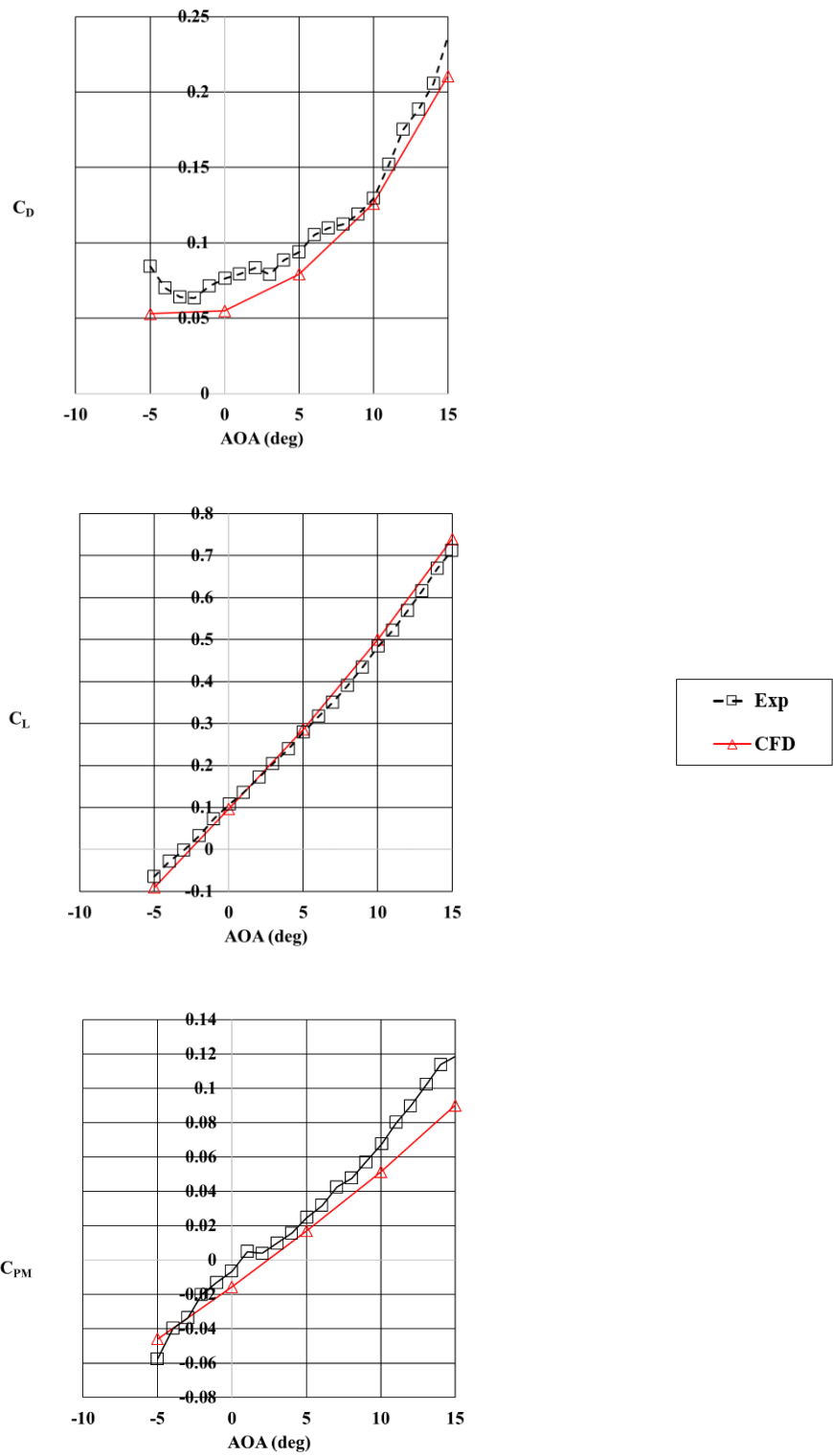


FIGURE 5.29. Aerodynamic force and moment coefficient results with additional angles of attack for Flick disc

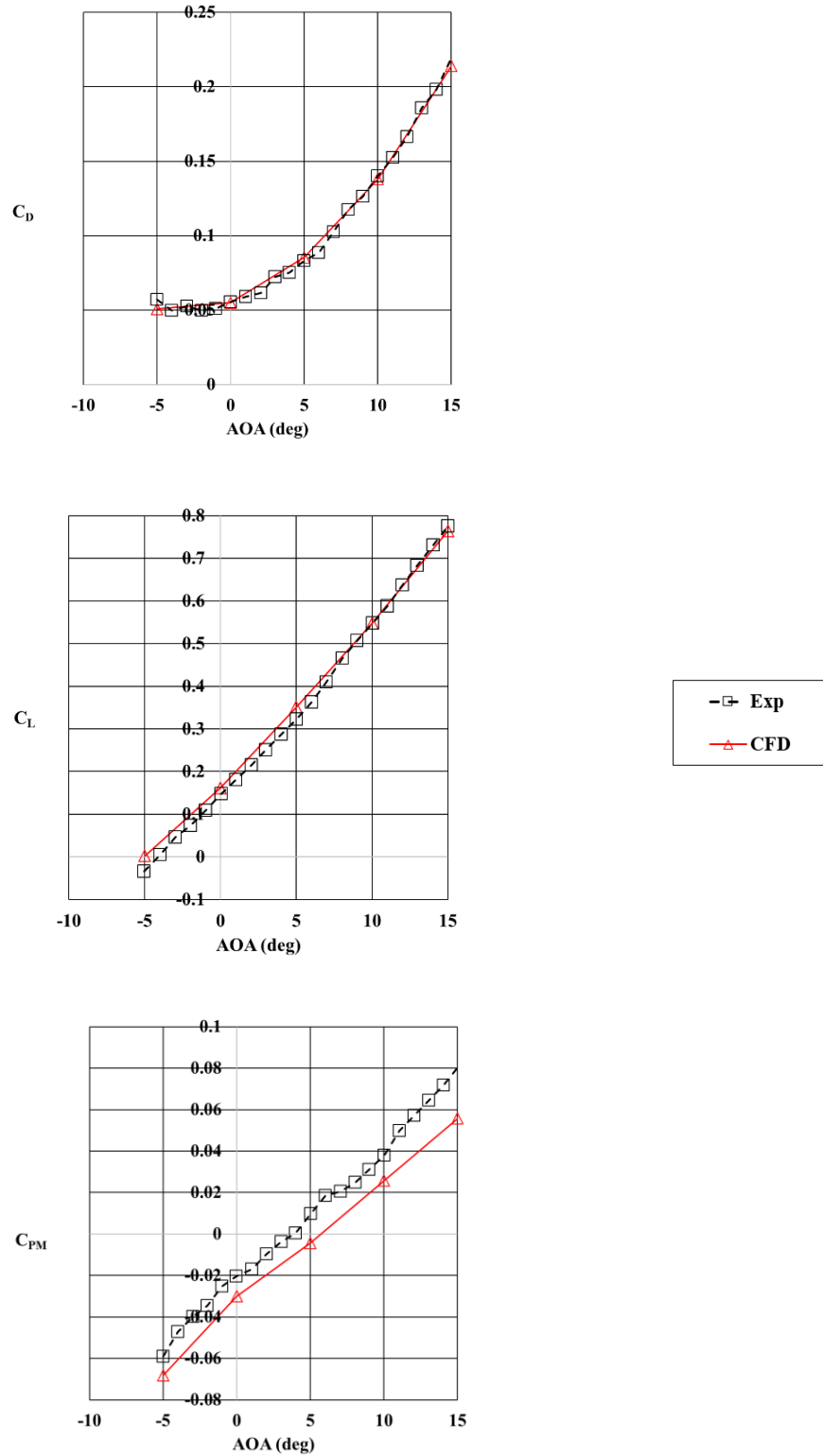


FIGURE 5.30. Aerodynamic force and moment coefficient results with additional angles of attack for Wraith disc

5.6 Note on preliminary simulations

Well over 100 preliminary RANS simulations were completed on discs by the author prior to beginning the bulk of the work included in this thesis. To maintain a practical length report, only the most significant runs have been detailed. Several additional turbulence models and closure coefficients were trialed. Many different meshes were also tested. Additionally, some simpler shaped discs were experimented with. Disc spin which showed a negligible effect was also investigated in early CFD runs.

CHAPTER 6. DES RESULTS

Detached eddy simulations were also performed as part of this study to assess if shortcoming in the RANS modeling could be remedied with DES. The DES study began with a mesh refinement study. Next a time step convergence study was commenced. Finally, some challenging aspects of the disc flow identified in the comparisons of RANS to CFD data are analyzed in the DES results. The DES study started with large eddy turnover times (LETOTs) of 197; LETOTs were later reduced to 79 to conserve resources.

6.1 Mesh refinement study

TABLE 6.1 presents the results of the mesh refinement study for DES runs at 10 degrees angle of attack. The time-step was held constant at 0.079 flow through times (FTTs). Flow through times were based on disc length and the free stream velocity of 21.6 m/sec. Only cases with like LETOT data averages (last column) should be compared to one another. From case 1 to case 2 (coarse to medium mesh) convergence was not reached. From case 3 to case 4 (medium to medium targeted) there was very little change in C_D and C_L , so convergence was deemed sufficient to proceed using the medium mesh. Most researchers focus only on C_D and C_L for convergence determination using force and moment coefficients. C_{PM} is typically not published. It could be argued that convergence was not reached between the medium and medium targeted mesh due to the 14% change in C_{PM} from case 3 to case 4 but due to limited resources and anticipated long runs times, the medium mesh was used. Note, cases 3 and 4 data could have been presented as averages over the same LETOTs as cases 1 and 2 but it was deemed instructive to show the difference in data caused by averaging over different LETOTs. FIGURE 6.1 and

FIGURE 6.2 present residual data and force and moment coefficients verses iterations respectively for the M27 medium mesh for the LETOTs=197 run.

TABLE 6.1. Aerodynamic force and moment coefficients from DES mesh refinement study for constant time step of $\text{FTT}=0.079$, $\text{AoA}=10^\circ$

Case	Mesh name	Mesh no.	C_D	C_L	C_{PM}	Run time (LETOTs)	Data average time (LETOTs)
1	coarse	M29	0.180	0.465	0.026	79	39
2	medium	M27	0.165	0.457	0.026	79	39
3	medium	M27	0.139	0.432	0.036	197	79
4	medium targeted	M31	0.142	0.435	0.031	197	79
RANS Lag EB $k-\epsilon$ tuned	medium	M27	0.192	0.532	0.007	NA	NA

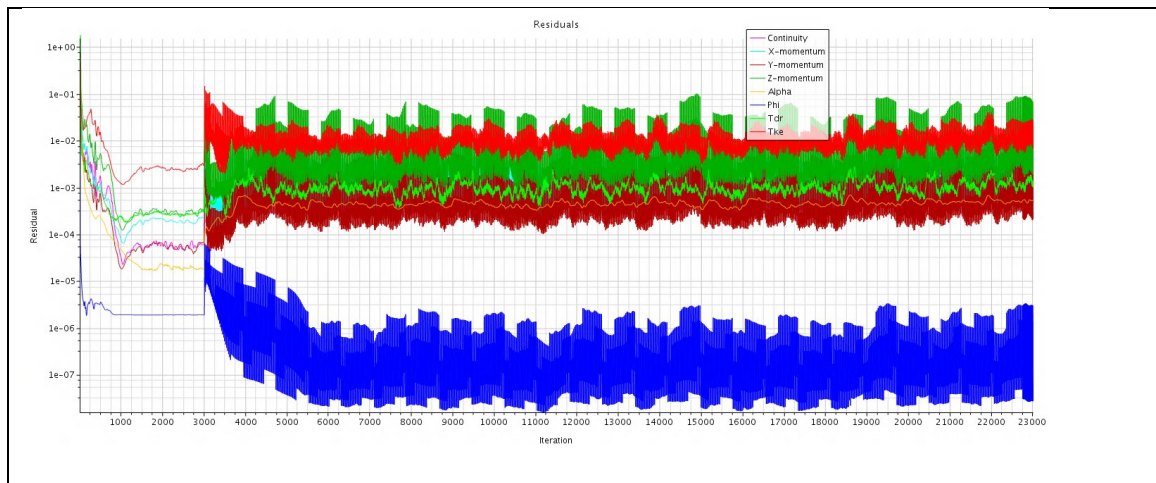


FIGURE 6.1. Residuals for M27, LETOTS=197, $\text{FTT}=0.079$

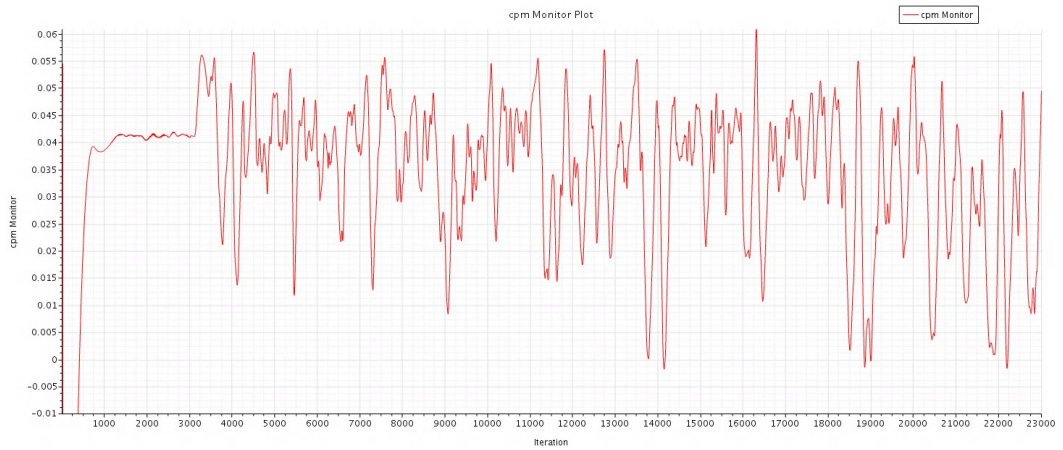
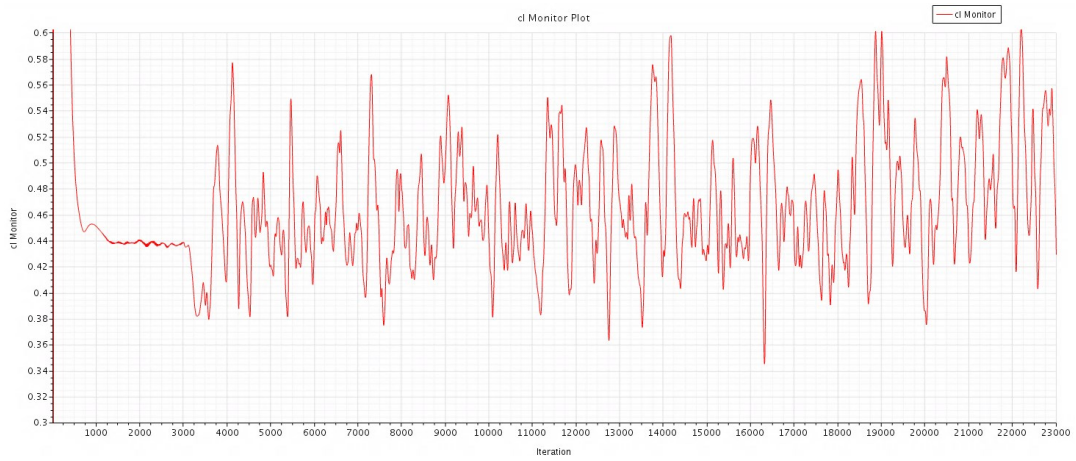


FIGURE 6.2. C_D (top), C_L (center) and C_{PM} (bottom) for M27, LETOTs=197, FTT=0.079

6.2 Time step convergence study

Using the medium mesh, which was deemed converged, a DES time step convergence study was conducted. This study commenced at 10 degrees angle of attack. Runs were for 79 LETOTs and averaged for 39 LETOTs. TABLE 6.2 presents the aerodynamic force and moment coefficient results of this study for FTTs of 0.079, 0.039, and 0.008. The oscillation of the force and moment coefficients across the FTTs was not expected. Again, proportionally to their total values, C_D and C_L moved within a much tighter band than C_{PM} . Since one of the main reasons for running DES was determine if DES could provide accurate predictions in areas where RANS may have fallen short, it was decided to move on from the 10 degree angle of attack case to one of the more challenging cases for RANS even though time step convergence had not been reached for the 10 degree case. One such challenging case for RANS was predicting the pressure profile for the top leading edge of the Floater disc at 20 degree angle of attack. It is obvious from FIGURE 5.12 that all RANS turbulence models did not predict this experimental behavior correctly. As evidenced by the upper pressure profile, flow separates gradually aft of the leading edge and then reattaches gradually. All turbulence models predicted a more abrupt separation and an almost immediate reattachment as evidenced by the leading edge double hump. For convenience, the bottom image from FIGURE 5.12 is included below as FIGURE 6.3 with the double hump circled for the experimental curve. To determine if the prediction of this behavior could be improved through time steps convergence, FTTs of 0.008, 0.004, 0.002, and 0.001 were run for the 20 degree case. FIGURE 6.3 through FIGURE 6.7 show the centerline pressure profiles for these cases. All DES cases predict the leading edge separation correctly and match the experiment well – separation and gradual attachment

with a reduced peak suction on the upper leading edge surface. As seen in the pressure profile plots, when the time step was reduced, the upper pressure profiles more closely matched the experimental curve until FFT=0.001. This phenomenon needs further investigation. It was expected that for each successively smaller time step, the CFD curve would more closely match the experimental curve. This held true until the FFT=0.001 case. TABLE 6.3 presents the force and moment coefficient results for the DES time-step convergence study along with the RANS Lag EB $k-\epsilon$ tuned model results. The decrease in pitch moment for the DES cases compared to RANS was expected since front suction was decreased. The force and moment coefficients as well as the pressure profile plots demonstrate that time-step convergence was not achieved.

TABLE 6.2. DES time step convergence, M27 medium mesh. AoA=10 °

time step (FFT)	time-step (msec)	C_D	C_L	C_{PM}
0.079	1	0.165	0.457	0.026
0.039	0.5	0.179	0.443	0.031
0.008	0.1	0.173	0.464	0.022

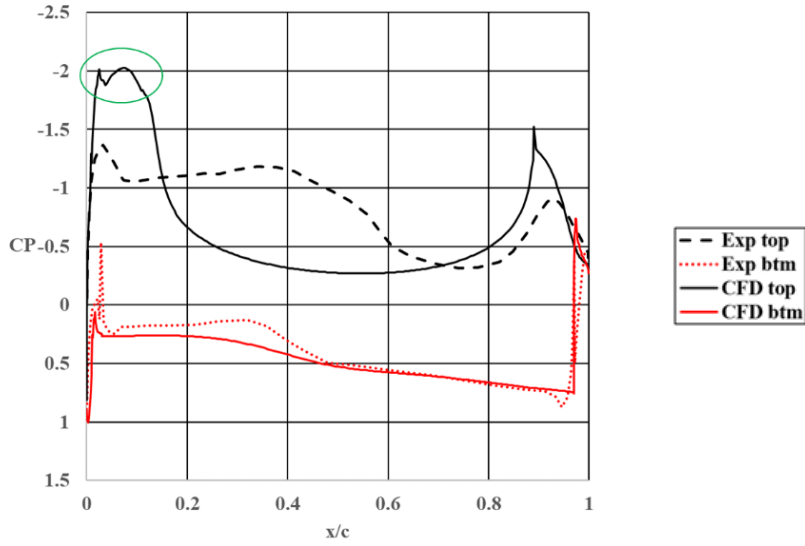


FIGURE 6.3. Centerline span pressure profiles for the Floater (calibration) disc. Experiment [2] and CFD Lag EB $k-\epsilon$ tuned (RANS) model, $AoA=20^\circ$

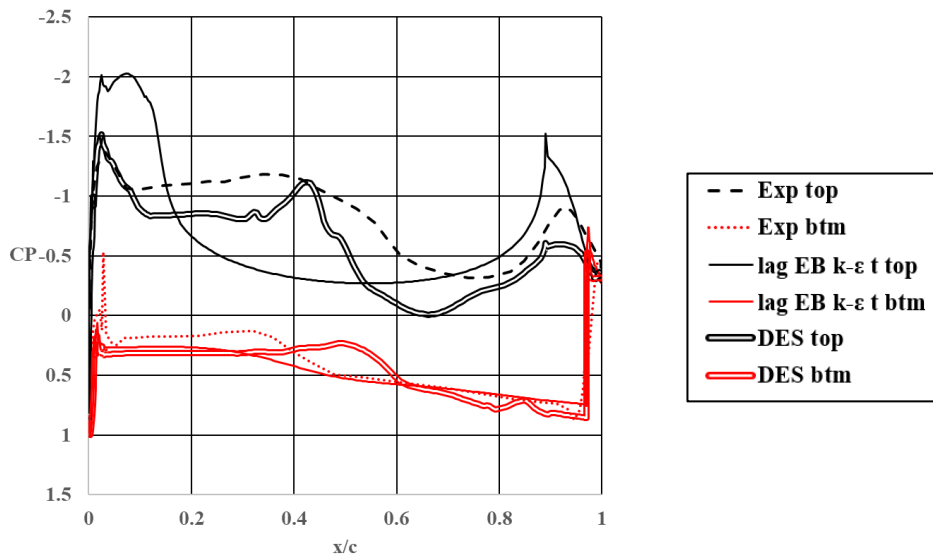


FIGURE 6.4. Centerline span pressure profiles for the Floater (calibration) disc. Experiment [2], Lag EB $k-\epsilon$ tuned model, and DES, $AoA=20^\circ$, DES FFT=0.008

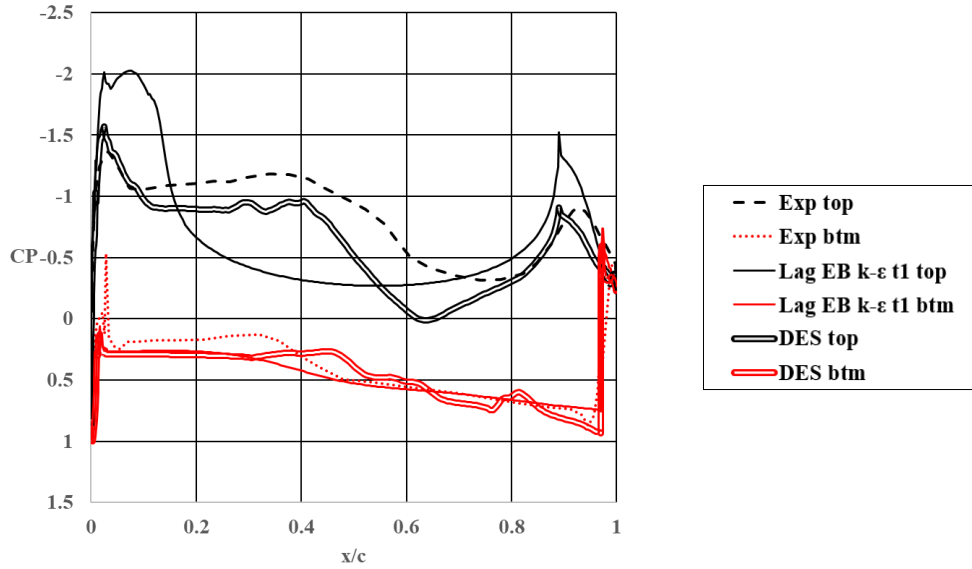


FIGURE 6.5. Centerline span pressure profiles for the Floater (calibration) disc. Experiment [2], Lag EB $k-\epsilon$ tuned model, and DES, $AoA=20^\circ$, DES FFT=0.004

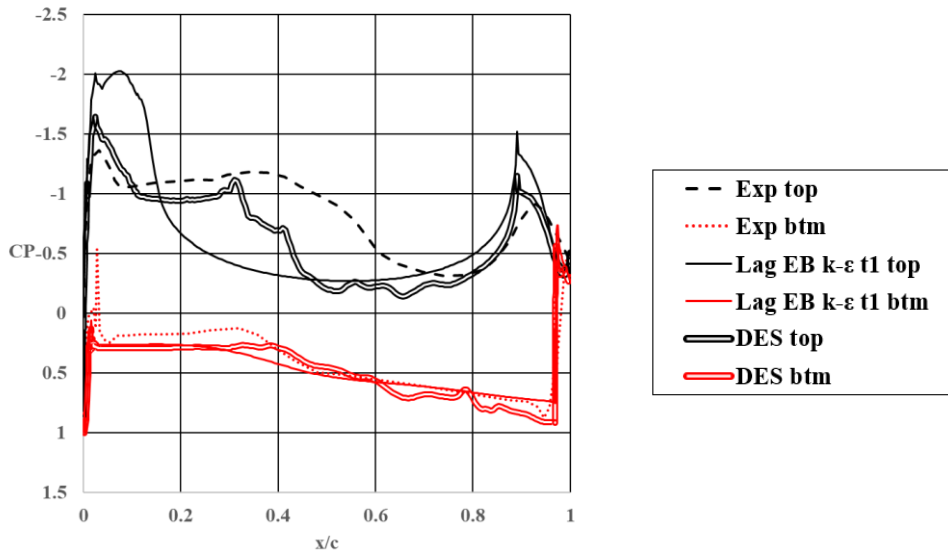


FIGURE 6.6. Centerline span pressure profiles for the Floater (calibration) disc. Experiment [2], Lag EB $k-\epsilon$ tuned model, and DES, $AoA=20^\circ$, DES FFT=0.002

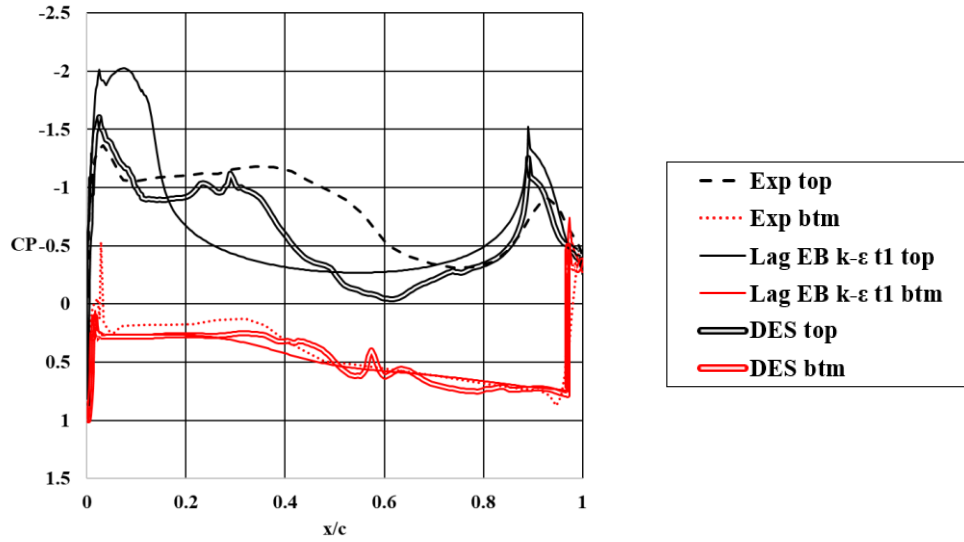


FIGURE 6.7. Centerline span pressure profiles for the Floater (calibration) disc. Experiment [2], Lag EB $k-\epsilon$ tuned model, and DES, $AoA=20^\circ$, DES FFT=0.001

TABLE 6.3. DES time step convergence, M27 medium mesh. $AoA=20^\circ$

Method	time step (FTT)	time step (msec)	C_D	C_L	C_{PM}
DES	0.008	0.1	0.501	0.986	-0.004
DES	0.004	0.05	0.484	0.944	0.004
DES	0.002	0.02	0.515	0.998	-0.004
DES	0.001	0.01	0.494	0.978	0.005
RANS, Lag EB $k-\epsilon$ tuned	NA	NA	0.468	0.991	0.012
Exp	NA	NA	0.56	1.2	0.049

CHAPTER 7. CONCLUSIONS

Golf disc manufacturers have a large amount of design freedom, but relatively few aerodynamic studies have been conducted on golf discs. This work has shown that RANS CFD is a viable tool for evaluating golf disc designs. Although high quality wind tunnel testing such as that reported in several references including [2] and [11] would be ideal, the lack of funding will likely preclude widespread testing in the near term. As the sport of disc golf grows, more funding will become available for wind tunnel testing. In the meantime, though as computing power increases and RANS models continue to be improved and tuned, additional widespread wind tunnel testing may not be needed. CFD could completely fill this role. The Lag EB k - ϵ tuned turbulence model matched the force and moment experimental data for the commercial golf discs reasonably well for a large portion of their probable operational range. C_D and C_L are likely within repeatability of the reverse engineering and experimental methods used. C_{PM} shows the most deviation from experiment but this is to be expected since small force changes at the extents of the disc can swing the pitch moment by large amounts. One must also consider that even when physical tests of identical models are performed at different wind tunnels, the results can vary by large amounts due to differences in the wind tunnels. Nevertheless, the CFD models still require improvements as is evidenced by the pressure coefficient data plots. Error created by scanning the pressure profile curves from an image file and disc geometric differences likely account for some of the deviation from CFD to experiment, but there are some obvious shortcomings in the CFD such as the large deviation in magnitude and shape for the top leading edge pressure profile on the Floater calibration disc at 20 degrees angle of attack. This is likely due to deficiencies in the turbulence modeling.

Additional conclusions from the current work are listed below:

1. The RANS Lag EB k - ε and Lag EB k - ε tuned turbulence models predicted the aerodynamic force and moment coefficients for the Floater calibration disc more accurately than the k - ω SST turbulence model compared to experimental data.
2. The k - ω SST turbulence model predicted a larger wake than the Lag EB k - ε turbulence model which is likely due to underprediction of turbulent kinetic energy in the shear layers by the k - ω SST model.
3. Changing the baseline Lag EB k - ε turbulence model closure coefficients as suggested by reference [32] for the standard k - ε model for wakes to $C_{\varepsilon 1}=1.2$ and $\sigma_{\varepsilon}/\sigma_k=1.8$ further reduced the size of the wake and increased the turbulent kinetic energy in areas of separation.
4. Even though time-step convergence was not reached, the accuracy advantage of DES for one of the more challenging cases became evident.

Future work could include the following:

1. Investigating individual parameter changes for streamlined golf discs using RANS models to determine if the predictive capability of RANS is more suited to certain parametric changes. Experimental data for these changes would be required.
2. Further tuning of the Lag EB k - ε turbulence model closure coefficients using the Floater calibration disc.
3. Additional DES runs with the Floater calibration disc further reducing the time-step.

4. Additional DES runs with the Floater calibration disc further increasing the mesh density since pitch moment had not converged.

REFERENCES

- [1] Professional Disc Golf Association , "PDGA Approved Disc Golf Discs," IDGC, 11 April 2020. [Online]. Available: <https://www.pdga.com/technical-standards/equipment-certification/discs?page=30>. [Accessed 11 April 2020].
- [2] J. R. Potts, "Disc-wing Aerodynamics," The University of Manchester, 2005.
- [3] E. Spanberg, "This family business was born from a hobby and an innovative idea," *Charlotte Business Journal* , 19 April 2019. [Online]. Available: [https://www-bizjournals-com.librarylink.uncc.edu/charlotte/news/2019/04/19/this-family-business-was-born-from-a-hobby-and-an.html](https://www.bizjournals-com.librarylink.uncc.edu/charlotte/news/2019/04/19/this-family-business-was-born-from-a-hobby-and-an.html). [Accessed 15 April 2020].
- [4] Wikipedia, "Disc Golf," Wikipedia, 18 April 2020. [Online]. Available: https://en.m.wikipedia.org/wiki/Disc_golf. [Accessed 22 April 2020].
- [5] S. A. Trendafilova and S. N. Waller , "Assessing the Ecological Impact Due to Disc Golf," *International Journal of Sport Management Recreation & Tourism*, vol. 8, pp. 35-64, 2011.
- [6] J. Senter, "Shawnee Mission Post," 21 June 2013. [Online]. Available: <https://shawneemissionpost.com/2013/06/21/local-disc-golfers-welcome-news-of-proposed-new-course-at-santa-fe-trail-park-19278>. [Accessed 14 February 2020].
- [7] Charlotte Disc Golf Club, "Charlotte Disc Golf Club," 12 April 2020. [Online]. Available: [http://charlottedgc.com/bradford-park/#iLightbox\[image_carousel_1\]/3](http://charlottedgc.com/bradford-park/#iLightbox[image_carousel_1]/3). [Accessed 12 April 2020].
- [8] H. Higuchi, G. Yuichiro, R. Hiramoto and I. Meisel, "Rotating flying disks and formation of trailing vortices," in *18th Applied Aerodynamics Conference*, Denver, CO, 2000.
- [9] P. Lissaman and M. Hubbard, "Maximum range of flying discs," in *8th Conference of the International Sports Engineering Association (ISEA)* , Vienna, Austria, 2010.
- [10] R. A. Lukes, J. H. Hart, J. Potts and S. J. Haake, "A CFD Analysis of Flow Around a Disc," *Procedia Engineering*, vol. 72, pp. 685-690, 2014.
- [11] N. Kamaruddin, J. Potts and W. Crowther, "Aerodynamic performance of flying discs," *Aircraft Engineering and Aerospace Technology*, pp. 390-397, 5 March 2018.
- [12] N. M. Kamaruddin, "Doctor of Philosophy Thesis "Dynamics and Performance of Flying Discs"," University of Manchester, 2011.

- [13] J. R. Potts and D. Masters, "Validation of the Aerodynamic Loading on Basic Flying Disc Geometries derived from CFD Simulations," *Procedia Engineering*, vol. 112, pp. 400-405, 2015.
- [14] P. Cosyn and J. Vierendeels, "Numerical Investigation of Low-Aspect-Ratio Wings at Low Reynolds Numbers," *Journal of Aircraft*, vol. 43, no. 3, pp. 713-722, 2006.
- [15] K. Hanjalić, *Turbulence and transport phenomena: Modelling and Simulation*, 2006.
- [16] H. Schlichting and K. Gersten, *Boundary Layer Theory*, Springer, 2001.
- [17] S. Pope, *Turbulent Flows*, New York: Cambridge University Press, 2000.
- [18] P. Davidson, *Turbulence: an introduction for scientists and engineers*, Oxford: Oxford University Press, 2015.
- [19] H. Tennekes and J. Lumley, *A First Course in Turbulence*, Cambridge MA: MIT Press, 1972.
- [20] W. Rodi, "Turbulence modeling and simulation in hydraulics: a historical review," *J. Hydraul. Eng.*, vol. 143, no. 5, pp. 1-20, 2019.
- [21] C. Argyropoulos and N. Markatos, "Recent advances on the numerical modelling," *Applied Mathematical Modelling*, vol. 39, no. 2, pp. 693-732, 2015.
- [22] J. Fröhlich, C. Mellen, W. Rodi, L. Temmerman and M. Leschziner, "Highly resolved large-eddy simulation of separated flow in a channel with streamwise periodic constrictions," *J. Fluid Mech.*, vol. 526, pp. 19-66, 2005.
- [23] D. Bepalko, A. Pollard and M. Uddin, "Direct Numerical Simulation of Fully-Developed Turbulent Channel Flow Using the Lattice Boltzmann Method and Analysis of OpenMP Scalability," in *High Performance Computing Systems and Applications*, Kingston, ON, Canada , Springer , 2009, pp. 13-30.
- [24] STAR-CCM+, "Reynolds Stress Transport (RST) Turbulence," in *STAR-CCM+ Documentation*, STAR-CCM+, 2020.
- [25] F. Menter, "Two-equation eddy-viscosity turbulence modeling for engineering applications," *AIAA*, vol. 32, pp. 1598-1605, 1994.
- [26] D. Wilcox, *Turbulence Modeling for CFD*, DCW Industries, Inc. , 1998.

- [27] S. Lardeau and F. Billard, "Development of an elliptic-blending lag model for industrial applications," in *54th AIAA Aerospace Sciences Meeting*, San Diego, CA, 2016.
- [28] W. Jones and B. Launder, "The prediction of laminarization with a two-equation model of turbulence," *Int. J. Heat Mass Transfer*, vol. 15, pp. 301-314, 1972.
- [29] C. Fu, M. Uddin, C. Robinson, A. Guzman and D. Bailey, "Turbulence Models and Model Closure Coefficients Sensitivity of," *SAE Int. J. Passeng. Cars - Mech. Syst.*, 2017.
- [30] C. Zhang, M. Uddin and C. Selent, "On Fine Tuning the k-w Turbulence Model Closure Coefficients for Improved Prediction of Automotive External Flows," in *Proceedings of the ASME 2018*, Pittsburgh, PA, USA, 2018.
- [31] N. Ashton, A. West, S. Lardeau and A. Revell, "Assessment of RANS and DES methods for realistic automotive models," *Computers and Fluids*, pp. 1-15, 22 January 2016.
- [32] S. Poroseva and H. Beazard, "On ability of standard k- ϵ model to simulate," *CFD Journal*, vol. 9, pp. 464-470, 2001.
- [33] STAR-CCM+, "Detached Eddy Simulation (DES)," in *STAR-CCM+ Product Documentation*, 2020.
- [34] University Research Computing, "UNCC Research Clusters," UNCC, 25 April 2020. [Online]. Available: <https://urc.uncc.edu/research-clusters>. [Accessed 25 April 2020].
- [35] Wikipedia, "Aerobie," Wikipedia, 29 January 2020. [Online]. Available: https://en.wikipedia.org/wiki/Aerobie#World_records. [Accessed 24 April 2020].
- [36] STARCCM+, "Prism Layer Meshing," in *STAR-CCM+ Documentation*, StarCCM+, 2020.
- [37] H. Schlichting, *Boundary Layer Theory*, New York: McGraw-Hill, 1955.
- [38] M. L. Henry, "Insight Derived from High Order Structured Finite Difference CFD Simulations of Flow Past Generic Simplified Car Models," University of North Carolina at Charlotte thesis, Charlotte, 2016.
- [39] N. Ashton and A. Revell, "Key factors in the use of DDES for the flow around a simplified car," *International Journal of Heat and Fluid Flow*, vol. 54, pp. 236-249, 2015.

